

CRACK GROWTH, SINGULARITIES AND
WAVE PROPAGATION IN AUXETIC
COMPOSITE MATERIALS

by

Mohammed Mustafa Adam

© Copyright by Mohammed Mustafa Adam, 2014

All Rights Reserved

A thesis submitted to the Faculty and the Board of Trustees of the Colorado School of Mines in partial fulfillment of the requirements for the degree of Doctor of Philosophy (Mechanical Engineering).

Golden, Colorado

Date _____

Signed: _____
Mohammed Mustafa Adam

Signed: _____
Dr. John R. Berger
Thesis Advisor

Golden, Colorado

Date _____

Signed: _____
Dr. Greg Jackson
Professor and Head
Department of Mechanical Engineering

ABSTRACT

An auxetic material is a material which has a negative Poisson's ratio, so it exhibit lateral expansion upon longitudinal tensile loading, or undergo lateral contraction under longitudinal compression. Such materials can exist in cellular form, or along specific axes in certain crystals.

The singularity order in a half plane consisting of two quarter dissimilar materials and the singularity at the tip of interfacial crack have been studied where the bi-material contains an auxetic material. The main goal was to investigate the effects of the auxetic behavior on the singularities. We have determined that the auxetic material has a significant effect on the singularity order. For example, the free-edge singularity can be removed for certain combinations of elastic moduli and auxetic Poisson's ratios. In general, the effects of the mismatch of elastic constants between the two materials on the singularity have been investigated and all these results will be shown in this dissertation.

The effect of a single particle or inclusion on crack propagation has been studied effectively using symmetric Galerkin boundary elements and a modified quarter-point crack tip element. Typical results show that an inclusion can decrease the crack-tip stress intensity as the crack approaches an inclusion, followed by deflection of the crack. Interestingly, as the crack extends beyond the inclusion there can also be an amplification of stress intensity. These previous results have shown the great influence the presence of an inclusion may have on a crack extension behavior. Here, we examine the influence of an auxetic particle on crack growth behavior. The objective of the present study is to understand the crack extension behavior and predict the crack growth direction in materials reinforced with auxetic particles. We will show the dramatic difference in crack path as compared to particles with positive Poisson's ratio.

The effects of a negative Poisson's ratio on wave propagation in elastic media are investigated numerically. Different types of elastic wave problems are taken into account. These problems are the reflection and transmission of SH-waves, and P-waves in two half-spaces and the SH-wave propagation in layered half-space. We focused on the elastic wave amplitude as a function in Poisson's ratio of this study. The results indicate a significant effect of auxetic material on wave amplitude. For example, the negative Poisson's ratio suppresses reflection and the incident wave totally transmits through the interface. Also, it reduces the value of the transmitted wave amplitude nearly to one half with compared to the incident wave amplitude. In another example, the auxetic material converts the value of amplitude from complex to real.

TABLE OF CONTENTS

| | |
|---|------|
| ABSTRACT | iii |
| LIST OF FIGURES | viii |
| LIST OF TABLES | xi |
| LIST OF SYMBOLS | xii |
| LIST OF ABBREVIATIONS | xv |
| ACKNOWLEDGMENTS | xvi |
| DEDICATION | xvii |
| CHAPTER 1 INTRODUCTION | 1 |
| 1.1 Review of Poisson's ratio | 1 |
| 1.2 Auxetic Materials | 3 |
| 1.3 Literature Review | 6 |
| 1.3.1 Singularities in bimetals | 7 |
| 1.3.2 Crack propagation | 7 |
| 1.3.3 Wave propagation | 10 |
| 1.4 BEM/ SGBEM and Green's Function | 13 |
| 1.4.1 Green's Function for Potential problems | 14 |
| 1.4.2 Green's Function for Elasticity problems | 18 |
| 1.4.3 Approximations and solution | 21 |
| 1.4.3.1 Collocation and Galerkin | 22 |
| 1.4.4 Singular and Hypersingular Integrals in BIE's | 27 |

| | |
|--|----|
| CHAPTER 2 SINGULARITIES IN AUXETIC BI-MATERIALS | 31 |
| 2.1 Singularities in bimetals | 31 |
| 2.2 Formulation | 31 |
| 2.3 The Free-Edge Problem | 33 |
| 2.4 The Interface Crack Problem | 35 |
| 2.5 Summary | 36 |
| CHAPTER 3 INFLUENCE OF AUXETIC PARTICLES ON CRACK PATHS | 38 |
| 3.1 Crack Extension Near a Particle | 38 |
| 3.2 Fracture Analysis by the SGBEM | 40 |
| 3.3 Effect of a Single Auxetic Particle on the Crack Path | 46 |
| 3.4 Effect of Double Auxetic Particles on the Crack Path | 52 |
| 3.5 Summary | 53 |
| CHAPTER 4 WAVE PROPAGATION IN AUXETIC COMPOSITE MATERIAL | 54 |
| 4.1 Reflection and transmission of SH waves in two half spaces | 54 |
| 4.1.1 Mathematical formulation | 54 |
| 4.1.2 Results and Discussion | 59 |
| 4.2 Reflection and transmission of P-waves in two half-spaces | 63 |
| 4.2.1 Mathematical formulation | 63 |
| 4.2.2 Results and discussion | 68 |
| 4.3 Wave propagation in layered half-space | 71 |
| 4.3.1 Mathematical formulation | 71 |
| 4.3.2 Results and Discussion | 77 |
| 4.4 Summary | 84 |

| | |
|---|----|
| CHAPTER 5 CONCLUSIONS AND SUGGESTIONS FOR FUTURE WORK | 85 |
| 5.1 Conclusions | 85 |
| 5.1.1 Stress singularity | 85 |
| 5.1.2 Crack propagation | 86 |
| 5.1.3 Wave propagation | 87 |
| 5.2 Suggestions for Future Work | 88 |
| REFERENCES CITED | 90 |
| APPENDIX - PROGRAMS, CODES USED AND METHODS | 98 |
| A.1 MATLAB program | 98 |

LIST OF FIGURES

| | | |
|------------|--|----|
| Figure 1.1 | A domain Ω with boundary Γ the source point P and field point Q | 15 |
| Figure 1.2 | The un-normalized tangent vector between the field and source points ($ R = Q - P $). | 16 |
| Figure 1.3 | The quadratic continuous element with three nodes. | 25 |
| Figure 1.4 | The cases of Galerkin integrations | 28 |
| Figure 1.5 | Coincident case and deforming the contour | 29 |
| Figure 2.1 | General elastic bimaterial problem. | 32 |
| Figure 2.2 | Singularity order δ for the free-edge problem as a function of ν_1 (with $\nu_2 = 0.30$) for $2 \leq \varepsilon = E_1/E_2 \leq 1000$ | 36 |
| Figure 2.3 | Singularity order δ for the free-edge problem as a function of ν_1 (with $\nu_2 = 0.30$) for $1.5 \leq \varepsilon \leq 4.5$ | 37 |
| Figure 2.4 | Imaginary part of the singularity order δ for the interface crack problem as a function of ν_1 (with $\nu_2 = 0.30$) for $1.5 \leq E_1/E_2 \leq 1000$ | 37 |
| Figure 3.1 | Crack approaching a particle. | 39 |
| Figure 3.2 | A domain containing a crack. | 42 |
| Figure 3.3 | Standard ($Q2, Q3$) and modified ($M2, M3$) quarter-point shape functions. | 44 |
| Figure 3.4 | Crack tip element. | 45 |
| Figure 3.5 | Three-point bend specimen. | 46 |
| Figure 3.6 | Comparison of results with Williams, et al. (2007) for non-auxetic particle-crack interaction, $\nu_p/\nu_m = 1$. Note that the horizontal scale is expanded to emphasize the crack path. | 47 |
| Figure 3.7 | Crack extension near an auxetic particle, $\nu_p/\nu_m = -1$. Note that the horizontal scale is expanded to emphasize the crack path. | 48 |

| | | |
|-------------|---|----|
| Figure 3.8 | Normalized mode-I stress intensity factor versus crack-tip position for $E_p/E_m = 2, \nu_p/\nu_m = \pm 1$ | 49 |
| Figure 3.9 | Normalized mode-II stress intensity factor versus crack-tip position for $E_p/E_m = 2, \nu_p/\nu_m = \pm 1$ | 50 |
| Figure 3.10 | Normalized mode-I stress intensity factor versus crack-tip position for $E_p/E_m = 8, \nu_p/\nu_m = \pm 1$ | 51 |
| Figure 3.11 | Crack extension near a particle, $\nu_p/\nu_m = \pm 1$, for $E_p/E_m = 0.5$ and $E_p/E_m = 2$ | 51 |
| Figure 3.12 | Effect of E_P/E_m on crack deflection in existence of two particles. | 52 |
| Figure 4.1 | Propagation of plane waves in two half-spaces | 55 |
| Figure 4.2 | Propagation of SH-waves in two half-spaces | 57 |
| Figure 4.3 | Transmitted SH-wave in two half-spaces (T_S/I_{SH}), amplitude ratios vs. Poisson's ratio. | 60 |
| Figure 4.4 | Reflected SH-wave in two half-spaces (R_S/I_{SH}), amplitude ratio vs. Poisson's ratio. | 61 |
| Figure 4.5 | The transmitted and reflected SH-waves in one plot compared to each other. | 61 |
| Figure 4.6 | Transmitted SH-wave, the amplitude ratio as a function in the incident angle for various values of Poisson's ratio. | 62 |
| Figure 4.7 | Reflected SH-wave, the amplitude ratio as a function in the incident angle for various values of Poisson's ratio. | 62 |
| Figure 4.8 | The transmitted and reflected waves as a function in the incident angle in one plot compared to each other. | 63 |
| Figure 4.9 | Propagation of P-waves in two half-spaces. | 64 |
| Figure 4.10 | The amplitude ratio of reflected longitudinal P-wave, R_P/I_P vs. incident angle, ϕ_I in two half-spaces. | 69 |
| Figure 4.11 | The amplitude ratio of reflected transverse P-wave, R_S/I_P vs. incident angle, ϕ_I in two half-spaces. | 69 |

| | | |
|-------------|---|----|
| Figure 4.12 | The amplitude ratio of transmitted longitudinal P-wave, T_P/I_P vs. incident angle, ϕ_I in two half-spaces. | 70 |
| Figure 4.13 | The amplitude ratio of transmitted transverse P-wave, T_S/I_P vs. incident angle, ϕ_I in two half-spaces. | 70 |
| Figure 4.14 | Propagation of SH-wave in layered half-spaces | 73 |
| Figure 4.15 | The amplitude ratio vs. Poisson's ratio of the layer real (Re) and imaginary (Im) part, $E_1/E_2 = 1$ | 78 |
| Figure 4.16 | The real part of amplitude ratio vs. Poisson's ratio of the layer for various values of E_1/E_2 | 79 |
| Figure 4.17 | The imaginary part of amplitude ratio vs. Poisson's ratio of the layer for various values of E_1/E_2 | 80 |
| Figure 4.18 | The real part of amplitude ratio vs. Poisson's ratio of the layer for various values of layer thickness (H). | 81 |
| Figure 4.19 | The imaginary part of amplitude ratio vs. Poisson's ratio of the layer for various values of layer thickness (H). | 81 |
| Figure 4.20 | The real and imaginary part of amplitude ratio vs. Poisson's ratio for incident angle $\phi_I = 89\pi/180$ (grazing angle). | 82 |
| Figure 4.21 | The amplitude ratio vs. the incident angle (ϕ_I) for two values of Poisson's ratio ($\nu_1 = -1$ and -0.8). | 82 |
| Figure 4.22 | The real part of amplitude ratio as a function in Poisson's ratio for various values of incident angle (ϕ_I). | 83 |
| Figure 4.23 | The imaginary part of the amplitude ratio as a function in Poisson's ratio for various values of incident angle (ϕ_I). | 83 |
| Figure A.1 | Code Package For Crack Growth Direction calculations | 98 |

LIST OF TABLES

| | | |
|-----------|---|----|
| Table 2.1 | Values of ν_1 where $\text{Im}(\delta)=0$ ($\nu_2 = 0.3$). | 35 |
| Table 3.1 | The behavior of crack path in presence of soft or hard particle. | 52 |
| Table 4.1 | Case when the amplitude ratio is equal to 1 for $\phi = \pi/3$ and $E_1/E_2 < 2$ | 78 |

LIST OF SYMBOLS

| | |
|------------|--|
| ν | Poisson's Ratio |
| λ | Lamé's first parameter |
| κ | Isothermal compressibility |
| μ | Shear modulus |
| σ | Stress |
| δ | Singularity order |
| δ | Dirac delta |
| Γ | Boundary |
| Ω | Domain |
| χ | Characteristic Function of Open Domain |
| ρ | Density |
| ξ | Local Coordinate |
| ϕ | Notch-face Angle |
| α | Velocity of Longitudinal Wave |
| β | Velocity of Transverse Wave |
| $\phi(P)$ | Potential Function |
| ∇^2 | The Laplacian |
| $2D$ | Two Dimensions |
| $3D$ | Three Dimensions |
| C_{ijkl} | Stiffness Tensor |

| | | |
|--------------------|-------|--|
| Σ_{ij}^E | | The External Stress Kernel |
| F_i | | Force |
| G | | Green's Function |
| H | | Hardness |
| Σ_{ij}^I | | The internal Stress Kernel |
| J | | The Jacobian Of Transformation |
| $N(P)$ | | Unit Outward Normal at P |
| P | | Source Point |
| P_k | | Selected Boundary Points |
| Q | | Field Point |
| R | | Un-normalized tangent vector |
| S_{ijkl} | | Compliance Tensor |
| e_i | | Unit Vector |
| g_i | | Galerkin Vector |
| δ_{ij} | | Kronecker Delta. |
| σ_{ij} | | Stress Tensor |
| ε_{ij} | | Strain Tensor |
| $\psi_k(P)$ | | Weight Function |
| $n(Q)$ | | Unit Outward Normal at Q |
| r | | Distance from the crack tip to a point |
| r | | Distance between two points, P and Q |
| t | | Parameter Space |
| t_i | | Traction Vector |

| | |
|--------------------|---|
| u_i | Displacement Vector |
| w_i | Displacement Kernel |
| ε_{xx} | Normal Strain in x -direction |
| ε_{yy} | Normal Strain in y -direction |
| B | Bulk Modulus |
| C | Elastic Stiffness Constant |
| D_{ijk} | Integral Singular Kernel of the Stress BIE |
| E | Young's Modulus |
| $F(P)$ | Flux |
| K_I | Stress Intensity Factor Mode-I |
| K_{II} | Stress Intensity Factor Mode-II |
| S | Elastic Compliance Constant |
| S_{ijk} | Integral Hypersingular Kernel of the Stress BIE |
| T_{ij} | Kelvin Kernel of Traction |
| $U(P)$ | Potential |
| U_{ij} | Kelvin Kernel of Displacement |
| V | Volume |
| e | Strain |

LIST OF ABBREVIATIONS

| | |
|------------------|--|
| BEM | Boundary Element Method |
| BIE | Boundary Integral Equation |
| COD | Crack Opening Displacement |
| DBEM | Dual Boundary Element Method |
| DCT | Displacement Correlation Technique |
| DE | Differential Equation |
| FEM | Finite Element Method |
| HBIE | Hypersingular Boundary Integral Equation |
| IE | Integral Equation |
| MQP | Modified Quarter Point crack tip element |
| PDE | Partial Differential Equation |
| SGBEM | Symmetric Galerkin Boundary Element Method |
| SIF | Stress Intensity Factor |
| UHMWPE | Ultra High Molecular Weight Polyethylene |

ACKNOWLEDGMENTS

First of all, I would like to express my sincere gratitude, deepest appreciation and respect to Dr. John Berger, my thesis advisor, for his guidance and support during the several years that I spent with him. He has been an advisor, teacher and friend. I have benefited from his experience and knowledge. I would like to thank him for his patience with me. He has spared no effort in helping me to overcome the difficulties faced by during my studies and research with him. He has been all the time encouraging and pushing me to the success.

Also, I would like to thank all my committee members, Dr. Graham Mustoe, Dr. Vaughan Griffiths, Dr. Paul Martin and Dr. Ivar Reimanis, for their valuable help and comments. I appreciate that they are taking time to read and revise my dissertation. I especially would like to thank Dr. Paul Martin and Dr. Ivar Reimanis for their precious time and useful discussions, that was great help for me. In addition, I would like to express my truthful thanks to Dr. Leonard J. Gray from Oak Ridge National Laboratory and Dr. Anh-Vu Phan from University of Southern Alabama for their worthy help and support by providing me SGBEM code.

However, I cannot express enough thanks to my parents for their unlimited support, encouragement and love. May Allah have mercy upon them. Finally, to my caring, loving, and supportive wife, Saaida: my honest gratitude. Your encouragement when the times got rough are much appreciated and duly noted. It was a great comfort and relief to know that you were willing to provide management of our household activities while I completed my work. I also thank my children. To Alrayan, Abdelaziz, Fatima and Jumana thank you for allowing me time away from you to research and write. My heartfelt thanks. For all these people, I say, without your support and encouragement this work would have never accomplished. Thank you all.

To my Parents, Mustafa Yadem Alnegrat and Fatima Sliman Ejnan.

CHAPTER 1

INTRODUCTION

This study presents research on the effects of Poisson's ratio for three elastic problems. They are the stress singularity in a bimaterial, crack path direction near inclusions, and elastic wave propagation. In this chapter we will review the main relevant topics and review some previous works that have relevance to the problems studied here. We will review the following subjects. The first is Poisson's ratio, the second is auxetic materials, and in the third section we will present brief and general background about stress singularities in a bimaterial, crack propagation near inclusions, and elastic wave propagation. The last section will also contain a review of the boundary element method (BEM) and symmetric Galerkin boundary element method (SGBEM).

1.1 Review of Poisson's ratio

Poisson's ratio (ν), as Poisson himself defined it, is the ratio between the transverse deformation and the longitudinal deformation when mechanical force is applied on material specimen in one dimension. Poisson observed that a material stretched under axial tensile forces not only elongates longitudinally, but it also contracts laterally. The property that characterizes this behavior is Poisson's ratio (ν) which is defined also as the negative lateral strain a stretched or compressed body divided by its longitudinal strain [1], so it is a dimensionless value. All common materials undergo laterally a transverse contraction when stretched in one direction and transverse expansion when compressed. The Poisson's ratio has two theoretical limits in an isotropic material: it is greater than -1 and equal to or less than 0.5, $-1 < \nu \leq 0.5$, and that is proved by elasticity theory. For anisotropic materials, Poisson's ratio can be defined by the elastic compliance constants as $\nu_{ij} = -S_{ij}/S_{ii}$ ($i, j = 1, 2, 3$), where S_{ij} is the elastic compliance constants, the inverse of elastic stiffness, C_{ij} [2]. The

bounds of Poisson's ratio in the anisotropic materials are wider ($-\infty < \nu < \infty$) than in the isotropic case [3].

Most common materials have a Poisson's ratio close to 1/3; however, rubbery materials have values approaching 1/2 [3]. Materials with a negative Poisson's ratio will contract (expand) in the transverse direction when compressed (stretched) [4]. For most well-known solids such as metals, polymers and ceramics, $0.25 < \nu < 0.35$. Glasses and minerals are more compressible, and for these $\nu \rightarrow 0$. For gases, $\nu = 0$, and network structures can exhibit $\nu < 0$. Materials with negative Poisson's ratio are called *auxetic* [5].

Poisson's ratio can be considered one of the two independent elastic moduli, for homogeneous linear isotropic material. Other common elastic constants such as Lamé's first parameter (λ), and bulk modulus (K), are commonly used for the second independent elastic constant. For example Lamé's first parameter (λ) can be expressed as

$$\lambda = \frac{E\nu}{(1 + \nu)(1 - 2\nu)} \quad (1.1)$$

where E is Young's modulus. In this relationship λ has real defined positive value, only if ν is in the valid range $-1 < \nu < 0.5$. Also, the bulk modulus, K , which governs volumetric expansion can be calculated as

$$K = \frac{E}{3(1 - 2\nu)} \quad (1.2)$$

Finally, the shear modulus, μ , can be calculated as

$$\mu = \frac{E}{2(1 + \nu)} \quad (1.3)$$

Rubbery materials undergo shear deformation but resist volumetric deformation, so $\mu \ll K$.

Solids with Poisson's ratio near to -1 would be the opposite of rubbery materials, they resist shear deformation and undergo volumetric deformation, where $\mu \gg K$ [3]. Isotropic elastic material can exhibit roughly four types of extreme behavior according to its elastic properties: rigid materials have high bulk and high shear moduli, spongy materials have low bulk and low shear moduli, rubbery materials have high bulk and low shear moduli

and dilational materials have low bulk and high shear moduli. The dilational materials fall outside realm of ordinary experience, and their existence within the frame work of continuum elasticity has been a subject of debate [6]. Poissons ratio can also be calculated as

$$\nu = \frac{3K - 2\mu}{2(3K + \mu)} \quad (1.4)$$

in terms of bulk modulus, K , and the shear modulus, μ , where the bulk and the shear moduli have positive values. Poisson's ratio (ν) is negative when $\mu < \frac{3}{2}K$, and it approaches -1 when $\mu \gg K$.

1.2 Auxetic Materials

In 1987 Lakes [7] presented a new foam structure which exhibited a negative Poisson's ratio. This was achieved by converting a conventional foam using heating and compression techniques to create a reentrant structure [7]. This type of material is called an auxetic material. An auxetic material expands laterally upon longitudinal tensile loading and contracts laterally under longitudinal compression. Some examples include pyrite ($\nu=-0.14$), transformed polymer foams ($\nu=-0.7$) [7], and silicon dioxide in its form α -cristobalite ($\nu=-0.5$ to -0.16) [8]. Auxetic materials are very rare in nature [9]. Man-made and natural auxetic materials and structures exist from the molecular to the micro and macroscopic levels [10]. Most of auxetics are fabricated or modified from conventional materials by using different techniques. Most studies either discovery of natural auxetic materials or design of auxetic materials are concerned with new materials exhibiting a negative Poisson's ratio.

In order to explain the auxetic behavior of materials with negative Poisson's ratio, some have investigated this behavior in terms of their geometry [11–15]. They presented a mechanism that achieves a negative Poisson's ratio based on an arrangement involving rigid triangles or squares or parallelograms connected together at their vertices by hinges. The auxetic behavior in these materials can be explained in terms of their geometry and deformation mechanism [11]. Molecular level auxetics have also been discovered, proposed, or

synthesized including nanostructure polymers, metals, silicates and zeolites. These indicate that the negative Poisson's ratio results from a very particular nano or microstructure in the material and the way this deforms when subjected to loads [15]. An explanation is proposed for experimental observed auxetic behavior in α -cristobalite where the auxetic behavior was identified and described by perfectly rigid rotating rectangles connected together. This system exhibits Poisson's ratio of -1 and this has been proved mathematically [16]. In real α -cristobalite materials, the assumption that the rectangles are perfectly rigid is not realistic and it is expected that Poisson's ratio would be less negative [16]. Typical models for auxetic behavior rely on completely regular microstructures to simplify the modeling and to produce transparent and beneficial results such as the granular model of Bathurst and Rothenburg, the broken rib model of Smith et al., and the two dimensional honeycomb model of Masters and Evans [17]. Manufactured auxetic materials have clearly disordered microstructures [17]. Simple analytical models have been developed and applied to both silica and germania in which the deformation of the α -quartz and α -cristobalite structures happens by rotation of the tetrahedra, dilation of the tetrahedra and concurrent rotation and dilation of the terrahera [10]. Several mechanisms causing auxetic behavior in materials have been found such as certain molecular networks, networks of dilating elastic elements, expanding chiral honeycomb lattices, and rotating rigid units [18].

Particular processing steps are required for producing polymeric materials with auxetic behavior such as foams, microporous films and fibers, and macroscopically perforated sheets [18]. There are several techniques to convert conventional material to auxetic one such as a compression and heating technique [7] which results in broken cell ribs in foams, permanent volumetric compression technique [19] and the powder metallurgy techniques of compaction, sintering and extrusion [20].

Auxetic materials have been studied theoretically, numerically and experimentally in order to investigate the effects of auxetic behavior on the material properties, and to know how to profit from these effects to enhance properties such as the hardness, toughness,

indentation resistance, acoustic response and others. Due to their unusual behavior and their properties, auxetic materials are interesting and there are many studies about these materials to investigate their effects on these materials properties. Some studies [19, 21–23] have provided an increased understanding of the effects of negative Poisson’s ratio on these material properties. For example, the shear modulus (μ) is predicted to increase [7, 8, 11, 19] as the Poisson’s ratio approaches the lower theoretical limit ($\nu=-1.0$) considering Young’s modulus (E) as constant where $\mu = E/2(1 + \nu)$.

Indentation resistance has been investigated on several fabricated auxetic materials. Enhancements in hardness (H) have been found where $H \propto (1 - \nu^2)^{(-2/3)}$ [7]. Auxetic materials have been found to be up to three times more difficult to indent than conventionally processed polymers [20]. A material with a negative Poisson’s ratio approaching the thermodynamic limit ($\nu = -1.0$) will be difficult to indent [7, 8]. The indentation resistance of auxetic microporous ultra high molecular weight polyethylene (UHMWPE) is a strain dependent property, and the hardness was improved by up to 2 and 3 over conventional UHMWPE in the presence of auxeticity [20, 23]. Foams with negative Poisson’s ratios were also found to have higher resilience than conventional foams [7].

Auxetic materials are predicted to become very tough according to classical elasticity theory when the Poisson’s ratio approaches the lower limit of -1.0. For example the fracture toughness of negative Poisson’s ratio open cell copper foams are enhanced by 80 percent, 130 percent and 160 percent for permanent volumetric compression ratio values of 2.0, 2.5 and 3.0, respectively, compared to the value of conventional foam with a positive Poisson ratio [19]. Currently, there is an interest in the development of many negative materials with counter-intuitive properties such as negative thermal expansion, negative permeability, permittivity, negative refractive index and negative Poisson’s ratios [10]. In general all these properties are related to the structural geometry of the materials, so there is a need for understanding the mechanisms acting within the material nano, micro or macro-structures [10].

A lot of experimental work has been done to either fabricate new auxetics or measure their properties. For example, samples of auxetic foams were produced from conventional ones through a simple compression/heating process [7]. In the study of Choi and Lakes [19], values of fracture toughness of auxetic foams have been determined experimentally using J_{ic} tests for different permanent volumetric compression ratio values. The single crystal elastic stiffness constants of α cristobalite have been measured under ambient conditions using laser Brillouin spectroscopy [8]. Also, the Poisson's ratio has been found to vary extensively with temperature over the $\alpha - \beta$ transition of cristobalite, SiO_2 , and takes a minimum value at around the transition point [24]. Furthermore, it has been found that Poisson's ratio is never positive over the entire temperature range of 300-1800 K [24].

Many papers in this field propose potential application for materials with auxetic behavior. In a recent paper, Stavroulakis (2005) [9] mentioned several potential applications for auxetic materials such as design of sealing for pipelines and machine components, and optimal noise and vibration absorbing behavior in concrete. Also, auxetic materials with enhanced hardness have certain advantages for the construction of wear-resistant machine components, the design of efficient piezoelectric sensors with applications in hydrophones and ultrasonic devices, and application in gaskets, which could seal better upon compression loading. The development of auxetic nanomaterials is expected to lead to high modulus auxetic materials, with potential applications in sensors, and molecular sieve and separation technologies [10, 25]. Other proposed applications such as expanding blast-proof curtains made from auxetic fibres protect people in an explosion by capturing debris from smashed glass, smart medical dressings that release medication in protection to the extent of swelling and several components of aircraft, naval vessels and automobiles [26].

1.3 Literature Review

There are many industrially relevant elastic problems related to material reliability such as cracks, stress singularities, and body waves. In recent studies, it is thought that auxetic materials could play positive role. There are many studies which investigate the effects of

auxetic behavior on several elastic parameters. In this section, a literature review of these problems is made to give a brief background about them.

1.3.1 Singularities in bimetals

The singularity order, δ , has been studied extensively in isotropic bimetals. For interface cracks, solutions of the type $\sigma \sim r^\delta$ have been obtained where δ is complex valued and r is the distance from crack tip. The free-edge problem has also been extensively studied [27, 28], as well as others, and the stress field solution was of the type r^δ where δ was real-valued depending on the elastic properties of the two materials. The parameters that the stress field depends on was reduced from three to two in [29] and these parameters were used to express the solution in a more compact way.

The plane problem of bonded dissimilar wedges of arbitrary angle and subjected to general forms of loading was studied in [30]. The solution was obtained by solving two simpler problems where the solution is given by the sum of solutions of the two separated problems. The dependence of singularity order in the stress field on the wedge angles and the elastic constants of the materials was also investigated in [30]. Numerical results of several angle geometries for all relevant material constants combinations were produced. Finally, we note that Green's function methods have also been used successfully on the free-edge problem. The anisotropic problem was considered in [31], where the Green's function was represented by an exact integral. Both the displacement and the stress Green's function were obtained. A Green's function method was also employed in [32] where a reduced equation for calculating the singularity order was found. An anisotropic bimaterial problem was also considered in [33] where it was noted that the free edge singularity vanishes for certain free-surface angles and elastic constants combinations.

1.3.2 Crack propagation

In the first half of the 20th century, fracture mechanics appeared as a separated discipline, and pioneers such as Bertram Hopkinson, Charles E. Inglis, Alan Griffith, Harold Wester-

gaard, George Irwin, Max Williams, Paul Paris and James R. Rice, and others put the main concepts and the essential basic theories for this branch of science. Hopkinson [34] made some general observations concerning the stresses around a crack in his paper published in The Sheffield Society of Engineers and metallurgists in January 1910. Inglis [35] calculated the intensities of the stress around an elliptic hole in a plate subjected to a tensile stress. Griffith [36] stated that fracture occurs when the tensile stress at a crack tip exceeds the theoretical cohesive strength of material. On the other hand, when there are no cracks at all, fracture strength would be equal to the theoretical cohesive strength. Westergaard [37] presented the stress field associated with cracks by solving plane stress or plane strain problems using an Airy stress function approach. Williams and Irwin, in two different papers, [38, 39] focused on investigating the factors influencing the growth of initial crack and established the stress-intensity factor. In comparative analytical and experimental study, Erdogan and Sih [40] investigated the crack extension direction in a two-dimensional plate made of brittle material, the hypothesis that the crack grows in the direction perpendicular to the largest tension at the crack tip was verified. The direction of crack growth in mixed mode stress field was investigated by Sih [41].

A crack will naturally propagate in a straight path perpendicular to the maximum stress unless it confronts an obstacle or inclusion. But when the crack grows in a non-uniform stress field, the path of the fracture is generally curved as Cotterell and Rice [42] stated. In their work, they presented a solution for the stress intensity factors at the tip of a slightly curved or kinked crack.

Hwu and Ting [43] studied the two-dimensional elliptic inclusion embedded in an anisotropic elastic material problem which was subjected to a uniform stress at infinity using the Stroh formalism [44]. Their solution included both extreme cases of the elliptic hole and rigid inclusion. Hwu and Yen [45] also obtained an analytical solution for anisotropic elliptical inclusions in a finite anisotropic matrix using the Stroh formalism combined with the method of analytical continuation. Later Yen et al. [46] obtained the analytical solution for a dislo-

cation located inside, outside or on the interface of an anisotropic elliptic inclusion. Hwu et al. [47] extended these analyses to problems of interactions between inclusions and different types of cracks such as a crack located inside or outside the inclusion, a crack penetrating the inclusion, and a curvilinear crack lying along the interface of the inclusion with the matrix. These problems were solved by representing the cracks as a distribution of dislocations where established analytical solutions for a dislocation located inside, outside or on the interface of an anisotropic elliptic inclusion were used [46]. Chen [48] considered a two dimensional solution for a crack outside an elliptical inclusion where he analyzed the interaction between the inclusion and the crack by the body force method. The effect of inclusion geometry on the stress intensity factors of small cracks was found to depend on the location of the crack.

For predicting the crack path direction, Bush [49] used the energy release rate technique and the boundary element method to study the interaction of a crack with a particle cluster. It was found that the energy release rate is affected by the presence of the particle and the crack deflected away. Kitey and others [50] also studied the interaction between a crack and particle cluster in a brittle material. They used numerical simulations based on symmetric Galerkin boundary element method (SGBEM) combined with quasi-static crack growth prediction tools, and used the modified quarter point (MQP) crack tip element of Gray [51]. The displacement correlation technique (DCT) was used to evaluate the stress intensity factors (SIFs). They investigated several parameters, energy release rate, crack growth direction, crack tip shielding and amplification, stress intensity factors and toughening of the material. Finally, the crack-particle interaction due to elastic constants mismatch was investigated by Williams et al. [52] using the symmetric Galerkin boundary element method (SGBEM). The modified quarter-point (MQP) crack tip element and the displacement correlation technique (DCT) were used to calculate the stress intensity factors (SIFs). The maximum principal stress criterion was employed to predict the crack growth direction. The authors demonstrated that the numerical results for the SIFs were very accurate and showed good agreement with known analytical solutions. The elastic constants were showed

to have a significant effect on the crack path direction and crack tip shielding. Stress intensity amplification behaviors as the crack propagated past the inclusion were clearly observed.

1.3.3 Wave propagation

Physically, waves are classified into two types. The first are the progressive waves, which move away from wave sources, the second are standing waves, which oscillate and cause vibration of the medium particles. According to the energy concentration, progressive elastic waves are divided into two types as well: body waves, which propagate inside a medium, and surface waves, which propagate on the surface of a medium. Moreover, both of these kinds of waves are divided again; the body waves are longitudinal waves and transverse waves while the surface waves are divided into two principal waves: Love waves and Rayleigh waves.

In this study, we will only deal with elastic body waves. Body waves consist of two principal waves: longitudinal waves, which appear first and are therefore called primary waves (P-waves) where all the particles of the medium move in the direction in which the wave is travelling, and transverse waves which are also called secondary waves (S-waves) where the particles move in perpendicular direction from the wave movement direction.

The presence of a discontinuity in material properties generally produces a significant influence on a system of waves propagating through the medium [53]. When elastic waves impinge on the interface of two different media, reflected and refracted waves appear with different angles made with the interface line. Any incident wave at the interface of two elastic solid bodies will introduce compressional (longitudinal) and distortional (transverse) waves in both media [54]. In 1898 Bromwich [55] found solutions for four elastic problems. He investigated the effect of gravity on Rayleigh waves in three problems by applying the equations derived by Love [56] for an incompressible material while in the fourth problem he studied the layered half-space considering a very thin layer of compressible material.

Biot [57] investigated the effects of initial stress on the propagation of Rayleigh waves in an elastic medium. He considered several cases of initial stress. The influence of initial stress only appears in the elastic coefficients of material for the case of the uniform hydrostatic

pressure. With a uniform pressure gradient, initial stress causes coupling between longitudinal and transverse waves. Also, the amplitude of the wave decreases exponentially with depth because of the gravity, and this effect increases with the wavelength. Finally, when the medium is under initial vertical compression, only the rotational waves are affected, and the velocity in the horizontal direction is higher than in the vertical.

In a theoretical study, the transmission of a plane elastic waves in layered media was investigated by Thomson [58] using the matrix method. He considered different materials for the layers with different thicknesses values. Philippacoulos [59] considered Rayleigh waves in a partially saturated layered half-space. He investigated this problem under plane strain conditions. Muskat and Meres [60] studied plane waves in an elastic media problem. They created systematic tables for the reflection and transmission coefficients as functions in incident angles for various types of interfaces. Wang et al. [61], also solved the propagation of SH-waves in a layered half-space problem in the presence of friction at the contact interface. The effects of various parameters such as shearing traction are discussed in light of their numerical results. Recently, Liu et al. [62] studied the propagation of SH surface waves in a layered piezoelectric half-space. They investigated the effect of the interfacial imperfection on the propagation velocity and the effect of a piezoelectric layer on the dispersive behavior. Destrade and Saccomandi [63], also studied the propagation of finite amplitude waves in elastic compressible materials. They derived solutions for the corresponding general equations of motion. Their results agreed with the well-known results of Carroll [64].

The research reported here investigates the effect of a negative Poisson's ratio on the amplitude of propagating elastic waves. Lipsett and Beltzer [65] are among the few people who have studied the effect of an auxetic material on wave propagation. They reconsidered several elastic wave problems for a material with a negative Poisson's ratio. They showed in their numerical results that the negative Poisson's ratio gives different results than that of the positive one in some cases. For the problem of longitudinal wave impinging on a free surface, they reported that the reflected amplitude ratio is equal -1 at zero incident angle.

Also, the reflected amplitude is equal to zero for two nonzero incident angles if Poissons ratio (ν) is less than 0.26, where it is totally reflected as a transverse wave. This case is known as total mode conversion. For positive Poissons ratio there is always just one reflected transverse wave except at the extreme angles corresponding to normal and grazing incidence angles (angles 0° and 90°). For Rayleigh waves, they obtained interesting results. They showed the relationship between the wave speed ratios (the ratio between Rayleigh wave speed (c_R) and the transverse (c_T) and longitudinal (c_L) wave speeds) and Poissons ratio for the range $-1 < \nu < 0.5$. They found that the maximum in c_R/c_T is near $\nu = -0.25$ and the longitudinal speed wave increases as the auxeticity of material increase. Also, they concluded that the maximum vertical displacement for an auxetic material occurs at the surface, while for typical material it occurs inside the material. However, the magnitude of horizontal surface displacement becomes nearly equal to that of the vertical displacement and both decay more rapidly as Poisson's ratio tends to -1.

Recently, Lim et al. [66] investigated the effect of the change in Poisson's ratio from positive (typical material) to negative (auxetic material) on the velocity of wave propagation in four different types of elastic waves. The results were interesting where the auxetic material has a different effect on each type of waves. They investigated the effect of negative Poisson's ratio on the velocity of elastic wave in isotropic material for four types of elastic waves, longitudinal waves in prismatic bars, plane waves of dilatation, plane waves of distortion and surface waves. The velocity of longitudinal waves in prismatic bars was found to be higher than that of the plane waves of distortion for a typical material, but the difference decrease in this case for auxetic material in the range $-0.5 < \nu < 0$. Also, the velocity of the longitudinal waves in prismatic bars is lower than that of the plane waves of distortion for auxetic material in the intermediate range $-0.733 < \nu < -0.5$, and lower than that of the surface waves for auxetic material in the high range $-1 < \nu < -0.733$. Furthermore, the velocity of the surface waves is slightly lower than that of the plane waves of distortion for a typical material, but the difference becomes larger when auxetic material is considered.

Goldstein et al. [67] compared the behavior of Rayleigh and Love surface waves in both auxetic and non-auxetic materials. It was found that the behavior of the Rayleigh and Love waves strongly depends on Poisson's ratio of the half-space in the Rayleigh case and on the two Poisson's ratios for the covering layer and the lower half-space in the Love case. They showed in their results that the Rayleigh wave velocity increases with decreasing Poisson's ratio, and it increases especially rapidly for negative Poisson's ratios less than -0.75 . Also, it is shown that, in the case of an incompressible thin covering layer, the velocity of the first mode of the Love waves strongly increases for negative Poisson's ratios of the half-space material. For negative Poisson's ratios, the Love wave in a layer and a half-space is mainly localized in the covering layer for any values of its thickness and weakly penetrates into the half-space.

Very recently, Lim [68] studied the effect of negative Poisson's ratio on vibration of thick plates. He considered the natural frequency of a Mindlin plate related to that of a Kirchhoff plate upon comparing the shear deformation in four cases, with and without rotary inertia, and the use of constant and variable shear correction factors. The results obtained recommend that the use of Mindlin plate theory with constant shear correction factor and no rotary inertia is sufficient to approximate the case of Mindlin plates of variable shear correction factor with rotary inertia when the plate's Poisson's ratio is positive. When the plate is auxetic, the natural frequency for the Mindlin plate is overestimated when at least one of the simplifying assumptions is used and the overestimation is especially large when both assumptions are used. As such, both the variable shear correction factor and rotary inertia must be taken into account when calculating the natural frequency of thick auxetic plates. The results also show that as the Poisson's ratio of the plate becomes more negative, the natural frequency of Mindlin-to-Kirchhoff plates increases.

1.4 BEM/ SGBEM and Green's Function

The boundary element method (BEM) is a numerical method used to solve complex problems which are difficult or impossible to solve analytically. More precisely, it is a numerical

computational method for solving linear partial differential equations which have been formulated as integral equations. In other words, it is a collection of numerical techniques for solving some basic partial differential equations (PDE). It is a powerful numerical technique for solving a wide variety of computational engineering and science problems, such as geo-mechanics, structural mechanics, electro-magnetics, acoustic, hydraulics, low Reynolds number hydrodynamics, biomechanics, off-shore structures and cathodic protection [69].

The mathematical foundations of the boundary element method include the theorems of Gauss, Green and Stokes which reduce the volume differential equation to a boundary integral equation [70], [71]. A distinguishing feature of this approach, as opposed to commonly employed "volume methods" such as finite element or finite differences, is that only the boundary of the domain is discretized, thereby reducing the dimension of problem by one. Also there are more advantages for using BEM such as the high accuracy for the stresses and displacements results, using less number of nodes and elements which means less computational time, and there is less data which reduces the computational effort and time.

The BEM is based upon transforming the differential equation (DE) into an integral equation (IE), this integral equation is valid everywhere inside the domain, on the boundary, and even the exterior to the domain, but it is usually the on-boundary form that is of interest. Many algorithms have been employed to approximate the solution of the boundary integral equation (BIE) numerically. The Symmetric Galerkin Boundary Element Method (SGBEM) is used in this dissertation. Also, we will consider and review the formulation of the SGBEM for the elasticity problems.

1.4.1 Green's Function for Potential problems

The transformation from differential to integral equation is made possible by employing Green's function (G). In the boundary element analysis, The Green's function is considered to be the fundamental solution to the governing differential equation. in both potential and

elasticity problems, the main ideas needed for BEM analysis are similar to each other.

We review the BEM for Laplace's equation. For two dimension (2D), the fundamental solution of Laplace equation is Green's function $G(P, Q)$ given as

$$G(P, Q) = \frac{1}{2\pi} \log \left(\frac{1}{r} \right) \quad (1.5)$$

where

$$\nabla^2 G(P, Q) = -\delta(P, Q) \quad (1.6)$$

P and Q are called the source and the field points, respectively, δ is the Dirac delta function, and r is the absolute distance between points Q and P (see Figure 1.1),

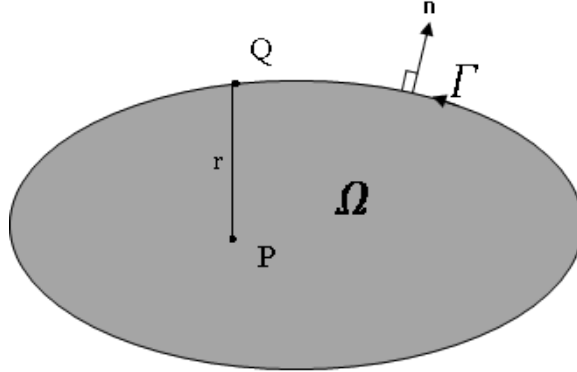


Figure 1.1: A domain Ω with boundary Γ the source point P and field point Q .

where

$$r = |R| = |Q - P| = \sqrt{(x_Q - x_P)^2 + (y_Q - y_P)^2 + (z_Q - z_P)^2} \quad (1.7)$$

R is the unnormalized tangent vector, which is illustrated in Figure 1.2.

The corresponding normal derivative with respect to n is

$$\frac{\partial}{\partial n} G(P, Q) = -\frac{1}{2\pi} \frac{\mathbf{n} \cdot \mathbf{R}}{r^2} \quad (1.8)$$

and the second corresponding normal derivative with respect to N is

$$\frac{\partial^2}{\partial N \partial n} G(P, Q) = -\frac{1}{2\pi} \left[-\frac{\mathbf{N} \cdot \mathbf{n}}{r^2} + 2 \frac{(\mathbf{n} \cdot \mathbf{R})(\mathbf{N} \cdot \mathbf{R})}{r^4} \right] \quad (1.9)$$

where $\mathbf{n} = \mathbf{n}(\mathbf{Q})$ is the unit normal to the boundary at point Q , $\mathbf{N} = \mathbf{N}(\mathbf{P})$ is the unit normal to the boundary at point P . So, ∂n indicates a derivative with respect to the coordinates of Q , and ∂N indicates a derivative with respect to coordinates of P . For fixed P , $G(P, Q)$ satisfies the Laplace equation everywhere except at $Q = P$. G is symmetric in its two arguments, $G(P, Q) = G(Q, P)$, so the roles of P and Q can be reversed.

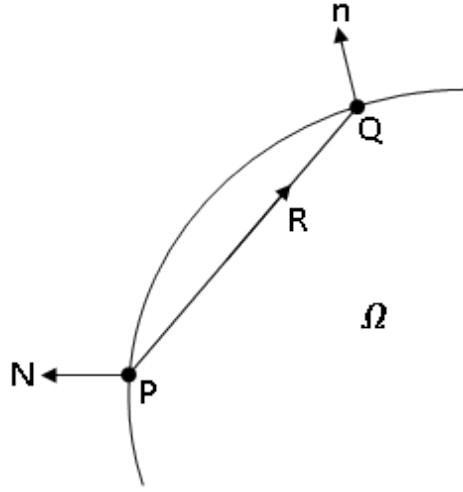


Figure 1.2: The un-normalized tangent vector between the field and source points ($|\mathbf{R}| = |Q - P|$).

For the Laplace equation in three dimensions (3D), the free space Green's function is

$$G(P, Q) = \frac{1}{4\pi r} \quad (1.10)$$

and its normal derivatives are

$$\frac{\partial}{\partial n} G(P, Q) = -\frac{1}{4\pi} \frac{\mathbf{n} \cdot \mathbf{R}}{r^3} \quad (1.11)$$

$$\frac{\partial^2}{\partial N \partial n} G(P, Q) = -\frac{1}{4\pi} \left[-\frac{\mathbf{N} \cdot \mathbf{n}}{r^3} + 2 \frac{(\mathbf{n} \cdot \mathbf{R})(\mathbf{N} \cdot \mathbf{R})}{r^5} \right] \quad (1.12)$$

The divergence of Green's function and its normal derivatives at $Q = P$ means that the numerical implementation of BEM for $P \in \Gamma$ must include the evaluation of singular integrals. When $r \rightarrow 0$ or $P = Q$, there is singularity in Green's function. The singularity in 3D case behaves as $\frac{1}{r}$, which is worse than the $\log(\frac{1}{r})$ for 2D case. Note that the singularity in normal derivative is worse than for G as is clear in the previous equations, Eqs.(1.5, 1.8, 1.9, 1.10, 1.11 and 1.12).

Green's second identity is used to transform Laplace equation, $\nabla^2 \phi = 0$, in the domain $\Omega \in \mathbf{R}^3$ with boundary Γ , from partial differential equation (PDE) of potential function $\phi(x, y, z)$ to a boundary integral equation (BIE) as

$$U(P) = \chi(P)\phi(P) + \int_{\Gamma} \left(\frac{\partial G}{\partial n}(P, Q)\phi(Q) - G(P, Q)\frac{\partial \phi}{\partial n}(Q) \right) dQ = 0 \quad (1.13)$$

Here, $\phi(Q)$ is in fact an exact solution of the Laplace equation, $G(P, Q)$ is a known function (Green's function), and $\chi(P)$ is the characteristic function of the open domain,

$$\chi(P) = \begin{cases} 1 & P \in \Omega \\ 1/2 & P \in \Gamma, \quad \Gamma \text{ is smooth} \\ (1 - \frac{\alpha}{2\pi}) & P \in \Gamma, \quad \Gamma \text{ is not smooth} \\ 0 & P \notin \Omega \cap \Gamma. \end{cases} \quad (1.14)$$

where α is the interior angle of the corner at P . $P \in \Gamma$ is a more delicate issue, due to the important fact that $G(P, Q)$ is singular when $P = Q$. The corresponding equation for the normal derivative of ϕ is

$$F(P) = \chi(P)\frac{\partial \phi}{\partial N}(P) + \int_{\Gamma} \left(\frac{\partial^2 G}{\partial N \partial n}(P, Q)\phi(Q) - \frac{\partial G}{\partial N}(P, Q)\frac{\partial \phi}{\partial n}(Q) \right) dQ = 0 \quad (1.15)$$

After discretizing the boundary integral equation (BIE), eq. (1.13) and introducing approximations for ϕ and $\frac{\partial\phi}{\partial n}$, the following boundary element method (BEM) matrix equation is obtained

$$[H]\{\phi\} = [G]\left\{\frac{\partial\phi}{\partial n}\right\}, \quad (1.16)$$

where $H = \frac{\partial}{\partial n}G(P, Q)$, and in block matrix form these equations are

$$\begin{bmatrix} H_{11} & H_{12} \\ H_{21} & H_{22} \end{bmatrix} \begin{Bmatrix} \phi_{bv} \\ \phi_u \end{Bmatrix} = \begin{bmatrix} G_{11} & G_{12} \\ G_{21} & G_{22} \end{bmatrix} \begin{Bmatrix} \left(\frac{\partial\phi}{\partial n}\right)_u \\ \left(\frac{\partial\phi}{\partial n}\right)_{bv} \end{Bmatrix} \quad (1.17)$$

where the subscript u indicates an unknown boundary value and a subscript bv indicates a known boundary value.

1.4.2 Green's Function for Elasticity problems

In order to understand and review the BEM analysis for fracture, first of all we should review the Green's function for elastic problem. Newton's second law expresses the motion of a linear isotropic material in equilibrium by the equations

$$\sigma_{ji,j} + F_i = \rho \frac{\partial^2 u_i}{\partial t^2}, \quad (i, j = 1, 2, 3) \quad (1.18)$$

where $\sigma_{ji} = \sigma_{ij}$ is the stress tensor, $\sigma_{ji,j} = \frac{\partial\sigma_{ji}}{\partial x_j}$, F_i are the body forces, ρ is the mass density and u_i are the displacements. The equilibrium equations, in the absence of the body forces and when the displacements are not function in time, become

$$\sigma_{ji,j} = 0 \quad (1.19)$$

For isotropic homogeneous solid Hooke's Law written as

$$\sigma_{ij} = \lambda\delta_{ij}\varepsilon_{kk} + 2\mu\varepsilon_{ij}, \quad (k = 1, 2, 3) \quad (1.20)$$

and the strain-displacement tensor

$$\varepsilon_{ij} = \frac{1}{2}(u_{i,j} + u_{j,i}) \quad (1.21)$$

where λ and μ are the first and second Lamé parameters, and δ_{ij} is the Kronecker delta. By substituting the strain-displacement equations in the stress equations, then substituting in the equilibrium equations, the following equation is obtained:

$$\mu u_{i,jj} + (\lambda + \mu)u_{j,ij} = 0 \quad \text{or} \quad \frac{u_{j,ij}}{(1 - 2\nu)} + \nabla^2 u_i = 0 \quad (1.22)$$

The governing equations obtained in two last forms, Eq. (1.22) are called Navier-Cauchy equations.

To solve the Navier-Cauchy equations, we use a function of the displacements, such as the Galerkin vector, to make the governing equation more ready for analytical solution [72]. The displacements are given in terms of derivatives of g_i [72] as

$$u_i = \nabla^2 g_i - \frac{1}{2(1 - \nu)} g_{j,ij} \quad (1.23)$$

substituting into the Navier-Cauchy equations yields

$$\nabla^2 g_i (\nabla^2 g_i) = 0 \quad (1.24)$$

The solution of previous equation (1.24) is the fundamental solution for the isotropic elastic problem. The fundamental solution (fundamental Galerkin vector) for three dimensions [73] is

$$g_i = \frac{1}{8\pi\mu} r e_i \quad (1.25)$$

For two dimensions, the fundamental solution is given by

$$g_i = \frac{1}{8\pi\mu} r^2 \log(r) e_i \quad (1.26)$$

where e_i indicates unit vectors and $i = 1, 2, 3$.

The reciprocal work theorem forms the basis of the BIE formulation [72]. For elastic problems, the reciprocal theorem is used to obtain the Somigiana first identity for displacements which is singular boundary integral equation (BIE). This mathematical process starts with the following identity

$$\int_V \sigma_{ij}^1 \varepsilon_{ij}^2 dV = \int_V \sigma_{ij}^2 \varepsilon_{ij}^1 dV \quad (1.27)$$

where the superscripts, 1 and 2, indicates two different solution states and V is the domain volume. By using Hooke's law ($\sigma_{ij} = C_{ijkl}\varepsilon_{kl}$), the symmetry of stiffness ($C_{ijkl} = C_{klij}$), substituting the displacement into the strains and using the fundamental solutions, (see for more details [72]), we get the displacement BIE (Somigiana first identity) as

$$u_i(P) = \int_{\Gamma} U_{ij}(P, Q) t_j(Q) dQ - \int_{\Gamma} T_{ij}(P, Q) u_j(Q) dQ \quad (1.28)$$

where t_j and u_j are the traction and displacement vectors, respectively, Γ is the domain boundary, U_{ij} and T_{ij} are the Kelvin kernel tensors. For plane strain problem the Kelvin kernels are given as [70, 74]

$$U_{ij}(P, Q) = \frac{1}{8\pi\mu(1-\nu)} [r_{,i} r_{,j} - (3-4\nu)\delta_{ij}\ln(r)], \quad (1.29)$$

$$T_{ij}(P, Q) = \frac{1}{4\pi(1-\nu)r} \left[\frac{\partial r}{\partial n} \{ (1-2\nu)\delta_{ij} + 2r_{,i} r_{,j} \} - (1-2\nu)(n_j r_{,i} - n_i r_{,j}) \right] \quad (1.30)$$

where $r_{,i} = \partial r / \partial x_i$, $r_i = x_i(Q) - x_i(P)$ and $\partial r / \partial n = r_{,i} n_i$.

For a point (P) interior to the domain the stress can be obtained by differentiating the previous BIE for displacement Eq. (1.28). Using that equation another time (Somigiana first identity of displacement) and substituting the displacement into Hooke's law we get the Somigiana second identity for the stresses which is the hypersingular BIE (HBIE) for the boundary stresses,

$$\sigma_{ik}(P) = \int_{\Gamma} D_{ijk}(P, Q) t_j(Q) dQ - \int_{\Gamma} S_{ijk}(P, Q) u_j(Q) dQ \quad (1.31)$$

where the kernels D_{ijk} and S_{ijk} are given by [70] as

$$D_{ijk} = \frac{1}{4\pi(1-\nu)r} [(1-2\nu)(\delta_{ij} r_{,k} + \delta_{jk} r_{,i} - \delta_{ki} r_{,j}) + 2r_{,i} r_{,j} r_{,k}] \quad (1.32)$$

$$S_{ijk} = \frac{\mu}{2\pi(1-\nu)r^2} \left[2 \frac{\partial r}{\partial n} \{ (1-2\nu)\delta_{ki} r_{,j} + \nu(\delta_{ij} r_{,k} + \delta_{jk} r_{,i}) - 4r_{,i} r_{,j} r_{,k} \} \right. \\ \left. + 2\nu(n_i r_{,j} r_{,k} + n_k r_{,i} r_{,j}) + (1-2\nu)(2n_j r_{,k} r_{,i} + \delta_{ij} n_k + \delta_{jk} n_i) \right. \\ \left. - (1-4\nu)\delta_{ki} n_j \right] \quad (1.33)$$

where $r^2 = r_i r_i$, μ is shear modulus, ν is Poisson's ratio and δ_{ij} is Kronecker delta.

1.4.3 Approximations and solution

As with all partial differential equations, it is required to give some additional information in order to obtain a solution. Here, this supplemental information is the boundary conditions which are usually given for every boundary point Q . For Laplace problem, the boundary condition is given as either the value $\phi(Q)$, or its normal derivative,

$$\frac{\partial \phi}{\partial n}(Q) = \nabla \phi \cdot \mathbf{n} = \left(\frac{\partial \phi}{\partial \mathbf{x}}, \frac{\partial \phi}{\partial \mathbf{y}}, \frac{\partial \phi}{\partial \mathbf{z}} \right) \cdot \mathbf{n} \quad (1.34)$$

In elasticity problems, either the displacement or traction is specified at each boundary point. The goal of a boundary element solution is to complete the knowledge of the boundary information, (potential and flux in potential problems, or in the case of elasticity, displacement and traction). BEM is most suitable for applications that only need a boundary solution. Interior values can be computed from Eq.(1.13). Eq.(1.13) provides an infinite number of equations, to balance the infinite number of unknown boundary values. Numerical approxi-

mations are used to reduce this to finite system of equations that can be solved. The main point of the transfer from volume methods to the boundary method is that the numerical approximations in BEM are limited to the boundary. The approximations are the interpolation of Γ and the boundary values but only the boundary has to be discretized. This provides significant benefits. In BEM, we treat the boundary potential and its normal derivative on equal footing. Thus, unknown values of the derivative are solved for directly, on the other hand the standard finite element method obtains an approximate potential everywhere in the domain and then must differentiate this approximation to get any required derivatives which incurs a loss of accuracy.

1.4.3.1 Collocation and Galerkin

For obtaining a numerical solution, there are two fundamental procedures that are generally applied to reduce the continuous integral equations, Eqs.(1.13) and (1.15) in potential problem and Eqs.(1.28) and (1.31) in elastic problem, to a finite system. The simpler procedure is the collocation approach wherein the boundary integral equations are explicitly enforced at a finite set of points. In its simplest form, these collocation points are selected to be the nodes used to discretize the boundary.

A collocation approximation of Eq.(1.13), in potential problems can be simply written as: $U(P_k) = 0$, where P_k , $1 \leq K \leq M$ are the selected boundary points. This gives the M equations required to solve for unknown values. Collocation necessarily leads to non-symmetric matrices. On the other hand, the Galerkin approach does not require that the integral equations satisfied at any point. Instead the equations are enforced in a weighted average sense,

$$\int_{\Gamma} \psi_k(P)U(P)dP = 0 \tag{1.35}$$

$$\int_{\Gamma} \psi_k(P)F(P)dP = 0 \tag{1.36}$$

Where $\psi_k(P)$ are the chosen weight functions. The required M equations can be generated by a suitable selection of M weights. Here we define the weight function $\psi_k(P)$ as the shape functions that are non-zero at the node P_k .

Mathematically, collocation is a strong solution, the equations are satisfied at the selected points, whereas Galerkin is a weak solution [70]. The Galerkin solution is the linear combination that is the closest to exact solution. In general, Galerkin is more accurate than collocation, and also provides a more accurate solution at the boundary corners. In addition, the primary advantage of Galerkin is that the treatment of hypersingular integrals is in fact much easier than with collocation.

For the elasticity problem, an equation similar to Eq. (1.13) can be written as

$$\chi(P)u_i(P) + \int_{\Gamma} T_{ij}(P, Q) u_j(Q) dQ - \int_{\Gamma} U_{ij}(P, Q) t_j(Q) dQ \quad (1.37)$$

This is the displacement BIE. The stress BIE is also needed for the symmetric Galerkin boundary element method (SGBEM) where the interior and exterior stress equations are obtained by differentiating the displacement Eq. (1.28) with respect to point P . The displacement and stress equations, Eqs. (1.28) and (1.31), for shortcut and simplicity can be rewritten as

$$w_i(P) = u_i(P) + \int_{\Gamma} T_{ij}(P, Q) u_j(Q) dQ - \int_{\Gamma} U_{ij}(P, Q) t_j(Q) dQ \quad (1.38)$$

and

$$\Sigma_{ij}^I = \sigma_{ik}(P) + \int_{\Gamma} S_{ijk}(P, Q) u_j(Q) dQ - \int_{\Gamma} D_{ijk}(P, Q) t_j(Q) dQ \quad (1.39)$$

$$\Sigma_{ij}^E = \sigma_{ik}(P) + \int_{\Gamma} S_{ijk}(P, Q) u_j(Q) dQ - \int_{\Gamma} D_{ijk}(P, Q) t_j(Q) dQ \quad (1.40)$$

where $w_i(P)$ is the displacement equation, Σ_{ij}^I and Σ_{ij}^E are the interior and exterior stress equations, respectively. In Galerkin approach, as it's discussed previously in this section,

the BIE's are enforced in a weighted average sense

$$\int_{\Gamma} \psi_k(P) w_i(P) = 0 \quad (1.41)$$

$$\int_{\Gamma} \psi_k(P) \Sigma(P) = 0 \quad (1.42)$$

Where $\psi_k(P)$ are the chosen weight functions as mentioned previously. Interchanging the derivative with integral is allowed if P is off the boundary due to the symmetry properties of Green's function, thus interior and exterior equations are mathematically appropriate. However, treating the singularity in Eq. (1.38) is necessary to achieve symmetric matrices in the SGBEM.

After discretizing the boundary integral equation, Eq.(1.37) we got the following form

$$\chi(P) u_i(P) = \sum_{n_k=1}^N \int_{\Gamma} U_{ij}(P, Q) t_j(Q) d\Gamma_n - \sum_{n_k=1}^N \int_{\Gamma} T_{ij}(P, Q) u_j(Q) d\Gamma_n \quad (1.43)$$

Numerical integration such as Simpson's rules, trapezoidal and Gauss-Legendre quadrature is frequently used. In most boundary element method programs, Gauss-Legendre quadrature is typically used for integrations when P and Q are not on the same element. Kelvin kernels, U_{ij} and T_{ij} are easy to be calculated for any pair of points, but it is not trivial to integrate these functions over the boundary element Γ_n , analytically.

For approximating the values of displacement (u_j) and traction (t_j), we consider the discrete points as nodes for the boundary elements. At these nodes, the values of displacement and traction will be interpolated. Also, at any other point on the element, the displacement and traction can be found by interpolating from the nodes which made possible through using the shape functions. The quadratic continuous element has a set of shape functions, in the local coordinate (ξ) as shown in Figure 1.3, $-1 \leq \xi \leq 1$,

$$\begin{aligned}
\psi_1(\xi) &= \frac{1}{2}\xi(\xi - 1) \\
\psi_2(\xi) &= (\xi - 1)(\xi + 1) \\
\psi_3(\xi) &= \frac{1}{2}\xi(\xi + 1)
\end{aligned} \tag{1.44}$$

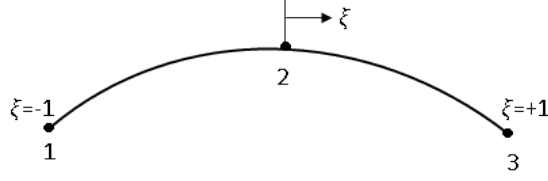


Figure 1.3: The quadratic continuous element with three nodes.

The displacement and the traction (u_j and t_j) at any point on the element can then be obtained by interpolation as

$$u_j(\xi_k) = \sum_{k=1}^3 \psi_k u_j(\xi_k), \tag{1.45}$$

and

$$t_j(\xi_k) = \sum_{k=1}^3 \psi_k t_j(\xi_k) \tag{1.46}$$

where $u_i(\xi_k)$ and $t_i(\xi_k)$ are the nodal displacement u_i and traction t_i , respectively at node ξ_k . By substituting the equations of displacement (Eq. 1.45) and traction (Eq. 1.46) in Eq. (1.43) in interpolated forms we obtain

$$\chi_{ij}(P)u_j(P) + \sum_{n=1}^N \int_{-1}^1 T_{ij} \sum_{k=1}^3 \psi_k u_j(\xi_k) J d\xi = \sum_{n=1}^N \int_{-1}^1 U_{ij} \sum_{k=1}^3 \psi_k t_j(\xi_k) J d\xi \tag{1.47}$$

where J is the Jacobian of the transformation from cartesian coordinate (x_k) to local coordinate (ξ_k). Also, we can write the previous equation, Eq. (1.47) as

$$\chi_{ij}(P)u_j(P) + \sum_{n=1}^N \left\{ \sum_{k=1}^3 u_j^n(\xi_k) \int_{-1}^1 T_{ij} \psi_k J d\xi \right\} = \sum_{n=1}^N \left\{ \sum_{k=1}^3 t_j^n(\xi_k) \int_{-1}^1 U_{ij} \psi_k J d\xi \right\} \quad (1.48)$$

which could be reduced to matrix term after integrating to become [69]

$$\chi_{ij}u_j + \sum_{n=1}^N \mathbf{H}_j^n u_j^n = \sum_{n=1}^N \mathbf{G}_j^n t_j^n \quad (1.49)$$

where N is the number of nodes, u_j^n and t_j^n are the displacements and tractions at node “ n ” and the matrices \mathbf{H} and \mathbf{G} are

$$\mathbf{H}_j^n = \sum_{k=1}^3 \int_{-1}^1 T_{ij} \psi_k J d\xi \quad (1.50)$$

$$\mathbf{G}_j^n = \sum_{k=1}^3 \int_{-1}^1 U_{ij} \psi_k J d\xi \quad (1.51)$$

\mathbf{H} and \mathbf{G} are 2×2 matrices in two dimensions and 3×3 in three dimensions case.

In Galerkin approach, the field and source points P and Q are treated equally, and thus it is possible to produce a symmetric coefficient matrix, the symmetric Galerkin boundary element method (SGBEM) [70]. Also, the integral kernels are symmetric. Thus if the displacement is known everywhere on the boundary, the BIE of displacement leads to a symmetric system of equations for the unknown tractions. Also, if the traction is known on the entire boundary, the BIE of traction yields symmetric system of equation for the unknown displacement. However, the displacement equation is employed on the part of the boundary where displacement is known, while the traction equation is employed on the part of the boundary where traction is specified to produce symmetric linear equations. In the end of Galerkin formulation, and after evaluating the kernel tensors U_{ij} , T_{ij} , D_{ijk} and S_{ijk} , from equation (1.49) we obtain system can be written in block matrix form

$$\begin{bmatrix} H_{11} & H_{12} \\ H_{21} & H_{22} \end{bmatrix} \begin{Bmatrix} u_{bv} \\ u_* \end{Bmatrix} = \begin{bmatrix} G_{11} & G_{12} \\ G_{21} & G_{22} \end{bmatrix} \begin{Bmatrix} t_* \\ t_{bv} \end{Bmatrix} \quad (1.52)$$

where u_* and t_* are unknown displacement and traction values, respectively and u_{bv} and t_{bv} are the known displacement and traction values on the boundary. Equation (1.52) can be rewritten in brief form as

$$\mathbf{H} \mathbf{u} = \mathbf{G} \mathbf{t}, \quad (1.53)$$

where \mathbf{u} and \mathbf{t} are vectors of displacement and traction nodal values, respectively. They contain either known or unknown value. \mathbf{H} and \mathbf{G} are $3N \times 3N$ square matrices. By rearranging the previous Eq. (1.53) to bring the unknown values to the left hand side and taking the known values to the right hand side we obtain the linear system in the form

$$\mathbf{A} \mathbf{x} = \mathbf{b}, \quad (1.54)$$

The vector \mathbf{x} contains all the unknown nodal values of displacement and traction on the boundary, which is easy to solve by using any numerical method such as Gauss elimination. After finding the unknown boundary values of displacement and traction, the displacement and stress at any internal point can be computed directly from the discretized Eqs. (1.28) and (1.31), respectively.

1.4.4 Singular and Hypersingular Integrals in BIE's

The singularities of the fundamental solutions requires more analysis when the source point P located on the boundary, or when P and Q are located on the same element. The boundary integral equations for the potential and elasticity problems involve the Greens function $G(P,Q)$ (fundamental solution) and its first and second derivatives. These functions are divergent when $P = Q$, the singularity becoming progressively worse with higher derivatives [70]. The integral of Green's function is indicated as "*singular*" integral and its second derivative is termed "*hypersingular*".

Roughly, there are three types of singularities in boundary integral equations, coincident

case, edge adjacent case and vertex adjacent case as illustrated in Figure 1.4. However, special quadrature necessary to handle singularities that occur when the source point of the integration is a member of the element being integrated must be considered for each of the three points defining a quadratic element [75]. The situation in three dimensions is naturally much more complicated, as singularities appear all along the edge shared by two elements [76]. Two types of singular integrals arise in a two dimensional calculation, coincident and adjacent where two elements are sharing a common node, and in three dimensions, there are two varieties of adjacent integration, adjacent elements may share a common edge or a common vertex [77].

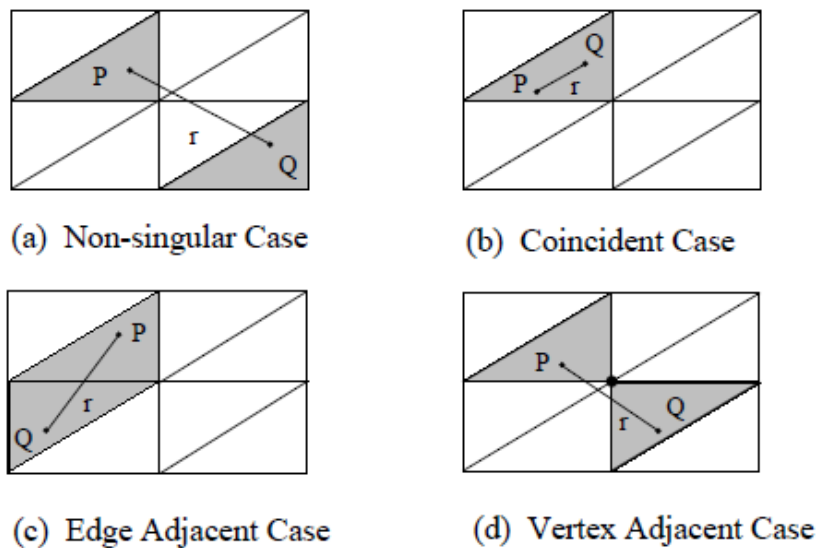


Figure 1.4: The cases of Galerkin integrations [78].

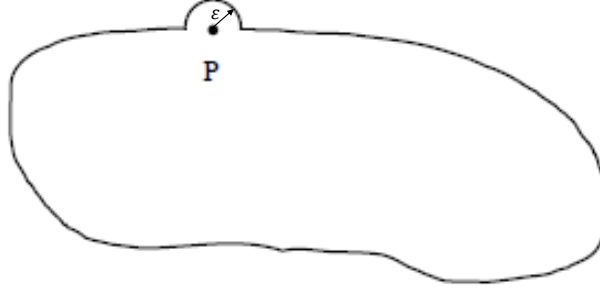


Figure 1.5: Coincident case and deforming the contour [78].

Many techniques are used for defining and computing the singular integrals [70]. One of these techniques is to define the boundary equation as a limit as P approaches the boundary, of either the interior or exterior equation. In the singularity case when the source point located on the boundary Γ , it's surrounded with a small circle of radius ε and the solution is examined when $\varepsilon \rightarrow 0$ which result new boundaries $\Gamma + \Gamma_\varepsilon$. We know that the BIE of displacement is

$$w_i(P) = u_i(P) + \int_{\Gamma} T_{ij}(P, Q) u_j(Q) dQ - \int_{\Gamma} U_{ij}(P, Q) t_j(Q) dQ \quad (1.55)$$

This equation provides solution for the displacement for all the locations of P either interior or exterior the domain or located on the boundary (Γ). The solution can not be trivial when $P \in \Gamma$. The integrals in the BIEs for both the potential and elasticity problems (Eqs. (1.13) and (1.38)) are singular. Therefore, they need more examination and treatment. For the singularity of integration, Sutradhar et al. [70] present an approach to solve these kind of integrals. This approach defines the boundary integral as a limit as the source point (P)

approaches the boundary from inside or outside the boundary. It's found that it's necessary to establish that these limits exist. Also, finding the boundary limit is essential to be able to handle the corresponding equation for its normal derivatives in equations (1.39) and (1.40).

The kernels U_{ij} and T_{ij} in Eq. (1.38) are singular at $Q = P$, they behave as $\log(r)$ and r^{-1} for two dimensions, respectively. when $r \rightarrow 0$. Also, in Eqs. (1.39) and (1.40), the kernels D_{ijk} and S_{ijk} have higher order singularities, behaving as r^{-1} and r^{-2} , respectively. Galerkin approach is used because it is very effective in dealing with the hypersingular kernels beside the fact that Galerkin has high accuracy, produces symmetry and deal easier with corner integration, whereas collocation fails to treat this type of singularity. The singular integration algorithm is based upon the fact that the displacement and stress equations, Eqs. (1.38) and (1.39) or (1.40) are defined only for P off the boundary, so the limit of singular integral evaluated as P approaches the boundary either from inside or outside the domain.

CHAPTER 2

SINGULARITIES IN AUXETIC BI-MATERIALS

The motivation for the present chapter is to investigate problems in elastic bimetals when one portion of the bimaterial is auxetic. Typical problems of this nature are the free-edge singularity (which can be useful in investigating delamination failures in bimetals) and the interface crack problem. To generalize the problem, we present results for both the free-edge and interface crack problems over the entire range of permissible Poisson ratios where the effect of a material becoming auxetic on the stress singularity order may be readily seen. It is important to refer that this chapter is based on a published paper [79]

2.1 Singularities in bimetals

We consider the general bimaterial problem shown in Figure 2.1. Both Material 1 and Material 2 are taken to be linear, elastic, isotropic, and homogeneous. Material 1 has Poisson's ratio ν_1 and shear modulus μ_1 , and Material 2 has ν_2 and μ_2 . We will assume the two materials are perfectly bonded at the planar interface so displacements and tractions are continuous across the interface. The local polar coordinate system r, θ is positioned at the root of the notch, and the notch-face angle ϕ is assumed to be symmetric with respect to the interface. There are, in general, four types of problems which are special cases of Figure 2.1 determined by the notch-face angle, ϕ . Here we will focus on two specific problems: the *free-edge problem* ($\phi = \pi/2$) and the *interface crack problem* ($\phi = \pi$). Of interest in all four of these problems is the nature of the increase in stress (if any) as $r \rightarrow 0$.

2.2 Formulation

In this section, we review the analytical solution for the bimaterial wedge as introduced in previous papers, see for example [27, 80]. Typical solutions use an Airy stress function in

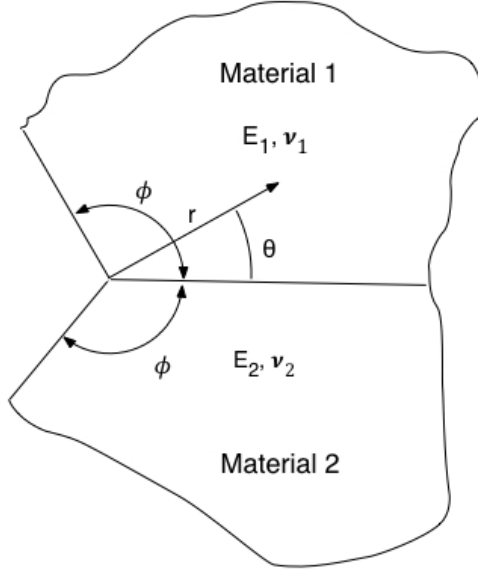


Figure 2.1: General elastic bimaterial problem.

polar coordinates, $\psi(r, \theta)$ [81], written in each portion of the bimaterial,

$$\psi_j(r, \theta) = r^\delta F_j(\theta), \quad j = 1, 2 \quad (2.1)$$

where $F_j(\theta)$ can be determined from the governing differential equation for ψ , $\nabla^4 \psi = 0$. The stress components in each portion of the bimaterial are then

$$\begin{aligned} \sigma_{rr}^{(j)} = & (\delta + 1) r^\delta \{ \delta [A_j \sin \delta \theta - B_j \cos \delta \theta] \\ & - (\delta + 2) [C_j \sin(\delta + 2)\theta + D_j \cos(\delta + 2)\theta] \} \end{aligned} \quad (2.2)$$

$$\begin{aligned} \sigma_{r\theta}^{(j)} = & (\delta + 1) r^\delta \{ \delta [A_j \cos \delta \theta + B_j \sin \delta \theta] \\ & + (\delta + 2) [C_j \cos(\delta + 2)\theta - D_j \sin(\delta + 2)\theta] \} \end{aligned} \quad (2.3)$$

$$\begin{aligned} \sigma_{\theta\theta}^{(j)} = & (\delta + 1)(\delta + 2) r^\delta \{ A_j \sin \delta \theta + B_j \cos \delta \theta \\ & + C_j \sin(\delta + 2)\theta + D_j \cos(\delta + 2)\theta \} \end{aligned} \quad (2.4)$$

where $j = 1, 2$ indicating if the stress component is in Material 1 or Material 2.

Using similar notation, the displacements in each portion of the bimaterial are

$$u_r^{(j)} = \frac{r^{\delta+1}}{E_j} \{(\delta + \nu_j(\delta + 2)) [A_j \sin \delta\theta - B_j \cos \delta\theta] - (\delta + 2)(1 + \nu_j)[C_j \sin(\delta + 2)\theta + D_j \cos(\delta + 2)\theta]\} \quad (2.5)$$

and

$$u_\theta^{(j)} = \frac{r^{\delta+1}}{E_j} \{-(\nu_j(\delta + 2) + (\delta + 6))[A_j \cos \delta\theta + B_j \sin \delta\theta] + (\delta + 2)(1 + \nu_j)[C_j \cos(\delta + 2)\theta + D_j \sin(\delta + 2)\theta]\} \quad (2.6)$$

For continuity of displacement and traction at the interface, $\theta = 0$,

$$u_r^{(1)}(r, 0) = u_r^{(2)}(r, 0), \quad u_\theta^{(1)}(r, 0) = u_\theta^{(2)}(r, 0) \quad (2.7)$$

$$\sigma_{\theta\theta}^{(1)}(r, 0) = \sigma_{\theta\theta}^{(2)}(r, 0), \quad \sigma_{r\theta}^{(1)}(r, 0) = \sigma_{r\theta}^{(2)}(r, 0) \quad (2.8)$$

Finally, the traction-free surface conditions are

$$\sigma_{\theta\theta}^{(1)}(r, \phi) = \sigma_{\theta\theta}^{(2)}(r, -\phi) = \sigma_{r\theta}^{(1)}(r, \phi) = \sigma_{r\theta}^{(2)}(r, -\phi) = 0 \quad (2.9)$$

Substituting the stress and displacement equations in the boundary and continuity conditions, we obtain eight linear equations in the eight unknown values of A_j , B_j , C_j , and D_j which can be written in matrix form as $\mathcal{A}x = 0$. For a non-trivial solution we then have $\det \mathcal{A} = 0$, which yields the singularity order δ .

2.3 The Free-Edge Problem

For this problem, we consider the effects of an auxetic material on the singularity at the intersection between an interface and the free surface of the bimaterial. Following [32], the singularity order for $\phi = \pi/2$ can be computed from

$$\det \mathcal{A} = -4^4(\delta + 1)^2 [(1 - \nu_1)\mu_2 + (1 - \nu_2)\mu_1]^2 \Delta(\delta) = 0 \quad (2.10)$$

where

$$\begin{aligned}\Delta(\delta) = & (\beta^2 - 1)S^4 + [1 + 2(\delta + 1)^2(\alpha - \beta)\beta] S^2 \\ & + (\delta + 1)^2 [(\delta + 1)^2(\alpha - \beta)^2 - \alpha^2],\end{aligned}\quad (2.11)$$

$S = -\sin\frac{1}{2}(\delta + 1)\pi$, and α, β are Dundurs constants [29],

$$\alpha = \frac{\varepsilon - 1}{\varepsilon + 1}, \quad \beta = \frac{(\kappa_2 - 1)\mu_1 - (\kappa_1 - 1)\mu_2}{(\kappa_2 + 1)\mu_1 + (\kappa_1 + 1)\mu_2}, \quad \varepsilon = \frac{E_1}{E_2}\quad (2.12)$$

where

$$\bar{E}_j = \begin{cases} E_j & \text{Plane Stress} \\ E_j/(1 - \nu_j^2) & \text{Plane Strain} \end{cases}$$

and

$$\kappa_j = \begin{cases} (3 - \nu_j)/(1 + \nu_j) & \text{Plane Stress} \\ 3 - 4\nu_j & \text{Plane Strain} \end{cases}$$

In the majority of the literature (see, for example, [82]), physically admissible values for the Dundurs constants are restricted to lie within the parallelogram enclosed by $\alpha = \pm 1$ and $\alpha - 4\beta = \pm 1$ in the (α, β) plane. However, this result assumes that Poisson's ratio is positive. If we consider auxetic materials, the bounds on α remain unchanged but the values of β are no longer bound to lie within the parallelogram given above.

To examine the influence of one portion of the bimaterial becoming auxetic, we calculate the singularity order, δ , from Eq.(2.11) as we vary ν_1 . For this calculation we leave $\nu_2 = 0.30$ and allow the elastic moduli ratio, $\frac{E_1}{E_2}$ to vary. The first set of results are shown in Figure 2.2, where we plot δ as a function of ν_1 . We take values of ν_1 across the entire range of permissible values of the Poisson ratio, $-1 \leq \nu_1 \leq 0.5$. Note in the figure that the singularity order, δ , becomes increasingly negative as $\frac{E_1}{E_2}$ is increased for fixed ν_1 . Also, once Material 1 becomes auxetic ($\nu_1 < 0$), the singularity order is significantly effected by the Poisson ratio. In certain cases the singularity order decreases over 18% due to Material 1 becoming auxetic. Finally, in Figure 2.2 we note that for $\frac{E_1}{E_2} = 2$, the singularity disappears when ν_1 decreases below -0.4. This is explored in more detail in Figure 2.3 for moduli ratios of $1.5 \leq \frac{E_1}{E_2} \leq 4.5$. In Figure 2.3, note that if $\frac{E_1}{E_2} \geq 3$, the singularity can not be eliminated.

2.4 The Interface Crack Problem

For this problem, we investigate the effect of an auxetic material on the singularity at the tip of an interface crack, that is, when $\phi = \pi$. The stress field near the tip of the crack varies as [83]

$$\sigma \sim r^{-1/2}[\cos \text{ or } \sin](\text{Im}(\delta) \log r)$$

where the second term arises from the imaginary part of the singularity order and is usually referred to in the literature as the oscillatory part of the singularity. This can be computed from [84] as

$$\text{Im}(\delta) = \frac{1}{2\pi} \log \left[\frac{\kappa_1/\mu_1 + 1/\mu_2}{\kappa_2/\mu_2 + 1/\mu_1} \right]$$

where the μ_j are the shear moduli.

When the two portions of the bimaterial are closely matched elastically, the imaginary part of the singularity order is very small as expected, vanishing if $\mu_1/\mu_2=1$. In Figure 2.4 we have plotted $\text{Im}(\delta)$ for a variety of μ_1/μ_2 ratios as a function of ν_1 . As with the free-edge problem, we have kept $\nu_2 = 0.30$ for these calculations. We note in the figure that, in general, a negative Poisson's ratio causes the oscillatory singularity to decrease when compared to cases where the Poisson's ratio is positive. Of particular interest are cases, such as $\mu_1/\mu_2 = 7.5$, where the decrease due to the ν_1 becoming negative can actually drive $\text{Im}(\delta)$ to zero. In Table 2.1 we present values for ν_1 where $\text{Im}(\delta)=0$ for various μ_1/μ_2 ratios. For example if $\mu_1/\mu_2 = 4.0$ and $\nu_1 = -0.3$, the crack-tip singularity will be purely real.

Table 2.1: Values of ν_1 where $\text{Im}(\delta)=0$ ($\nu_2 = 0.3$).

| | | | | | | | | | | | | | |
|---------------|-----|-----|-----|------|------|------|------|------|------|------|------|------|------|
| μ_1/μ_2 | 1.5 | 2.0 | 2.5 | 3.0 | 3.5 | 4.0 | 4.5 | 5.0 | 5.5 | 6.0 | 6.5 | 7.0 | 7.5 |
| ν_1 | 0.2 | 0.1 | 0.0 | -0.1 | -0.2 | -0.3 | -0.4 | -0.5 | -0.6 | -0.7 | -0.8 | -0.9 | -1.0 |

2.5 Summary

In this chapter, we have investigated stress singularities in elastic bimetals where we allow the Poisson's ratio of one portion of the bimaterial to vary completely over $-1 < \nu < 0.5$. Our motivation for this study comes from recent discoveries of auxetic materials, and how this might affect stress singularities in such problems. We found that when one portion of the bimaterial becomes auxetic, the effect on either the free-edge or interface crack singularity can be profound, even causing it to vanish given appropriate values of the remaining elastic constants. As more auxetic materials are developed, this fact could lead to strategies helping to suppress delamination or fracture failures in these bimetals.

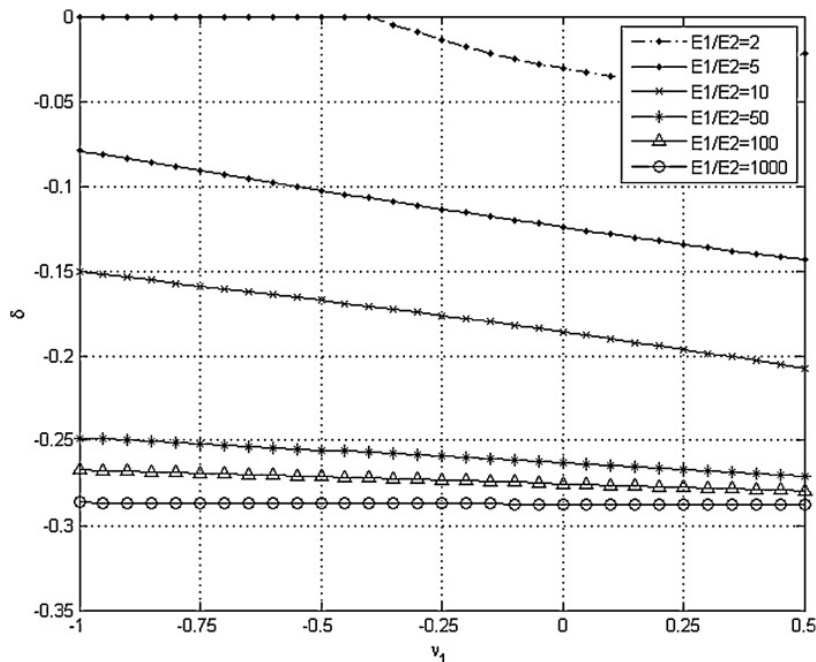


Figure 2.2: Singularity order δ for the free-edge problem as a function of ν_1 (with $\nu_2 = 0.30$) for $2 \leq \varepsilon = E_1/E_2 \leq 1000$.

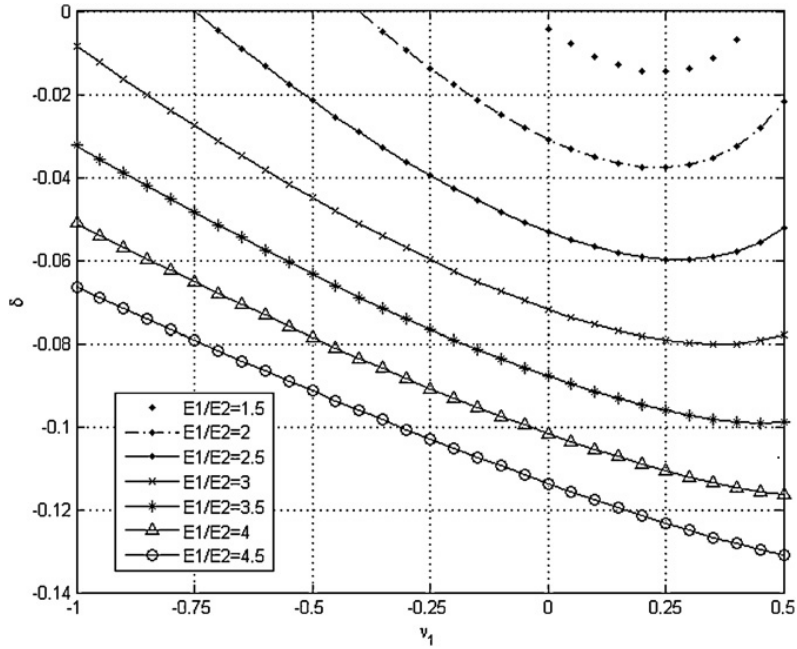


Figure 2.3: Singularity order δ for the free-edge problem as a function of ν_1 (with $\nu_2 = 0.30$) for $1.5 \leq \varepsilon \leq 4.5$.

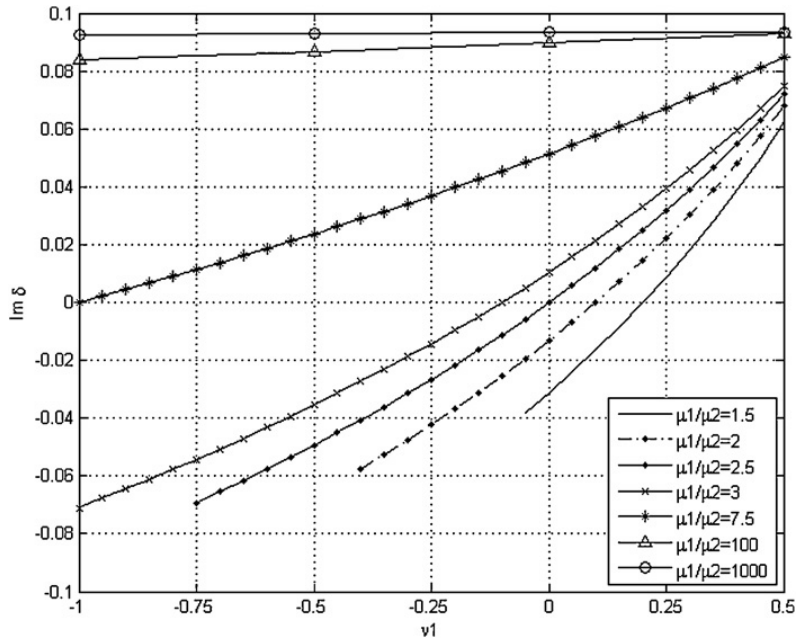


Figure 2.4: Imaginary part of the singularity order δ for the interface crack problem as a function of ν_1 (with $\nu_2 = 0.30$) for $1.5 \leq E1/E2 \leq 1000$.

CHAPTER 3

INFLUENCE OF AUXETIC PARTICLES ON CRACK PATHS

The motivation for the present chapter is to investigate problems involving crack extension near auxetic particles. Of particular interest are the conditions required, in terms of elastic constants, for a crack to either be deflected from or attracted to an auxetic particle. Knowledge of such conditions may suggest potential toughening strategies in brittle materials reinforced with auxetic particles. We will use a symmetric Galerkin boundary element method for our crack extension simulations. We first verify our simulations by performing crack extension studies near isotropic inclusions, and compare our results with results available in the literature for these problems (for example, in Bush [49], Williams, et al. [52]). We then investigate crack extension when the particle is auxetic, and present results in terms of elastic modulus mismatch for attracting or deflecting the crack from the particle. Finally, we investigate the behavior of the mode-I and mode-II stress intensity factors as the crack approaches the particle.

3.1 Crack Extension Near a Particle

The general problem of a crack approaching a particle (or inclusion) is shown in Figure 3.1. With reference to the figure, we will use E_p and ν_p for the Young's modulus and the Poisson's ratio for the particle, and E_m and ν_m for the Young's modulus and the Poisson's ratio for the matrix material. Both materials are considered isotropic, and we will be interested in the crack extension behavior for various ratios of the elastic moduli as ν_p becomes negative. We consider the particle to be perfectly bonded to the matrix material, so at the matrix-particle interface we have

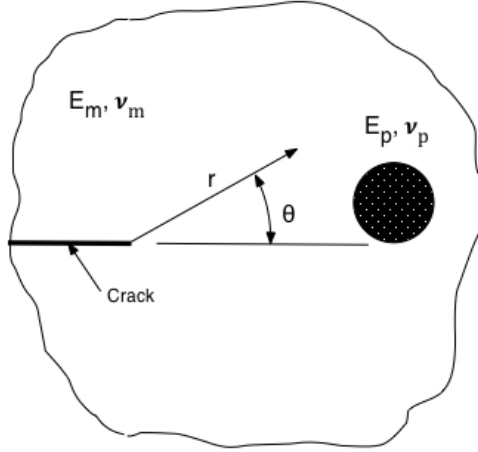


Figure 3.1: Crack approaching a particle.

$$u_r^p = u_r^m, \quad u_\theta^p = u_\theta^m$$

and

$$\sigma_{rr}^p = \sigma_{rr}^m, \quad \sigma_{r\theta}^p = \sigma_{r\theta}^m$$

where u_r , u_θ are displacement components and σ_{rr} , $\sigma_{r\theta}$ are stress components in polar coordinates, and the superscripts p and m indicate the particle and matrix, respectively.

The general problem of a crack interacting with a particle has been studied analytically both for isotropic materials (see, for example, Tamate [85], Atkinson [86], Erdogan et al. [87]) and for anisotropic problems (see, for example, Hwu et al. [88]). Bush [49] investigated the interaction between a crack and an inclusion in a discontinuously reinforced material by using a dual boundary element method (DBEM), combined with a maximum energy release rate criterion for crack extension. The effects of particle size and location on the crack path and on the energy release rate were studied. Simulations involving a single particle, two particles, and a group of ten particles were reported. The accuracy of the method was validated by analyzing a single-edge-notch fracture specimen and comparing the numerical results with exact solutions.

Williams, et al. [52] used a symmetric Galerkin boundary element method (SGBEM) to study numerically the effects of elastic constant mismatch on the crack path behavior in a reinforced brittle composite material in the presence of one or more inclusions. The simulation utilized a multi-zone SGBEM, and used a modified quarter-point crack tip element (Gray et al. [51]) for accurate crack-tip stress field modeling. Stress intensity factors were computed using a displacement correlation technique and the maximum principal stress criterion was used for predicting the crack propagation direction. Extensive validation studies were reported for the problem of a single particle in an infinite plate by comparing the numerical results with the results reported in Hwu et al. [88].

Perhaps most relevant to the study reported here is the paper by Knight et al. [89] where the problem of a crack approaching either a coated or uncoated inclusion was studied. The authors found that the Poisson's ratio of the different phases (matrix and inclusion) could have a *significant* effect on the crack trajectory. It was also shown that the energetics involved in the process of crack deflection were dramatically altered by the Poisson ratio mismatch. For a crack approaching an uncoated elastic inclusion, the authors concluded that by simply modifying the Poisson's ratio mismatch the rate at which the crack propagates, and the crack deflection/attraction mechanism can be controlled. We note that Knight et al. [89] only considered $0 < \nu < 0.5$; our work can be considered an extension of their analysis to cases where the inclusion becomes auxetic.

3.2 Fracture Analysis by the SGBEM

The symmetric Galerkin formulation for boundary integral equations in two-dimensional isotropic linear elastostatics has been extensively reported on in the literature and we will not review it here (see, for example, the book by Sutradhar et al. [70]). The SGBEM has several advantages for crack-extension problems (Williams, et al. [52]): the formulation yields a symmetric coefficient matrix; no subdomains are required to solve fracture problems; no smoothness requirements are needed on the displacements for evaluating the hypersingular integrals; and a smoother solution is obtained near geometric discontinuities.

We will use three-noded quadratic elements for the boundary element calculations reported here. We approximate both the boundary and the boundary functions using this particular interpolation. Employing the parameter space $t \in [0, 1]$, and defining $t_1 = 0$, $t_2 = 1/2$ and $t_3 = 1$, the shape functions are defined as

$$\begin{aligned}\psi_1(t) &= (1-t)(1-2t), \\ \psi_2(t) &= 4t(1-t), \\ \psi_3(t) &= t(2t-1),\end{aligned}\tag{3.1}$$

The approximate representations of the boundary and boundary functions are then given by

$$\alpha_i = \sum_{\ell=1}^3 \psi_\ell(t) \alpha_i^\ell\tag{3.2}$$

where α_i can be the boundary displacement u_i , the boundary traction t_i , or the boundary geometry x_i , or y_i . α_i^ℓ is the nodal value of α_i .

Let the elastostatic problem be posed in the domain Ω with outer boundary $\Gamma = \partial\Omega$. Further, let the portion of the outer boundary with displacement boundary conditions be Γ_u and the portion of the boundary with traction boundary conditions be Γ_t , so $\Gamma = \Gamma_u \cup \Gamma_t$. If a crack of boundary Γ_c is added to the domain, the new total boundary becomes $\Gamma^* = \Gamma \cup \Gamma_c$ (see Figure 3.2). The crack is composed of two symmetrically loaded surfaces Γ_c^+ and Γ_c^- which are initially coincident. Let $\Gamma_t^* = \Gamma_t + \Gamma_c^+$. In this case, the displacement and traction boundary integral equations (BIEs) are written as

$$u_k^*(P) = u_k(P) + \int_{\Gamma_c^+} T_{kj}(P, Q) \Delta u_j(Q) dQ = 0\tag{3.3}$$

$$T_k^*(P) = T_k(P) + n_\ell^+(P) \int_{\Gamma_c^+} S_{kj\ell}(P, Q) \Delta u_j(Q) dQ = 0\tag{3.4}$$

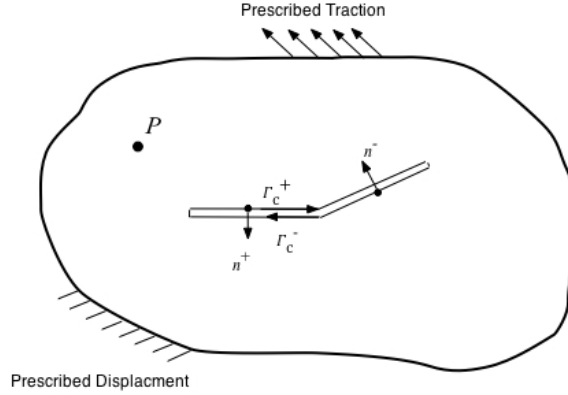


Figure 3.2: A domain containing a crack.

where T_{kj} and S_{kjl} are the usual Kelvin kernels used in boundary element analysis, P, Q are the source and field point locations, respectively, and n_ℓ^+ is the outward normal vector to Γ_c^+ . In these equations, the displacement jump vector Δu_j across the crack surfaces is used as the unknown on the crack. As a result, only one crack surface, e.g., Γ_c^+ , needs to be discretized. It is well known that the traction boundary integral equation, Eq. (3.4), is essential for treating crack geometries.

The use of Δu_j as the unknown on the crack as mentioned above is needed for obtaining a symmetric coefficient matrix. The symmetric-Galerkin formulation is given by

$$\int_{\Gamma_u} \psi_k(P) u_k^*(P) dP = 0 \quad (3.5)$$

$$\int_{\Gamma_t}^* T_k^*(P) dP = 0 \quad (3.6)$$

For standard fracture analysis problems, wherein the boundary condition on the crack is a specified traction, the symmetric-Galerkin procedure is remarkably simple: the above prescription (writing the traction equation on the crack surface) retains the symmetry, with the proviso that the unknowns on the fracture surface are now the jump in displacement, and the complementary variable is the sum of the known tractions. See for example, Sirtori et al. [90] and Bonnet et al. [74].

The important detail that requires discussion is the crack front treatment. As is well known, in linear elastic fracture mechanics the opening displacement at the crack front is non-analytic, behaving as $r^{1/2}$, where r is the distance to the tip. Obtaining accurate stress intensity factors therefore requires that this behavior is incorporated into the numerical model. Henshell and Shaw [91] and independently Barsoum [92], provided an easy way to do this: they showed that by moving the mid-node coordinates (x_2, y_2) three fourths of the way towards the tip, the parameter t becomes $\sqrt{r/L}$, with L the distance from (x_1, y_1) to (x_3, y_3) . As a consequence, the leading order term in Δu_k^j at $t = 0$, which is t , is the correct square root of distance. Note however, that the next term, which is t^2 , is r/L . Following Gray and Paulino [93] this term should vanish, and the modification presented below replaces this term with $(r/L)^{3/2}$.

For the new approximation, we keep the representation of $\Gamma(t)$ so that the property $t \approx \sqrt{r}$ remains, and the interpolation of the geometry remains quadratic. However for the crack opening displacement (COD, the difference in displacement on the two sides of the crack), we define new shape functions by adding a cubic term:

$$\begin{aligned}\psi_2(t) &= \frac{8}{3}(t^3 - t), \\ \psi_3(t) &= \frac{4}{3}(4t^3 - t).\end{aligned}\tag{3.7}$$

This additional contribution accomplishes the cancellation of the $t^2 \approx r$ term, without disturbing the interpolation, i.e., $\hat{\psi}_\ell(t_m) = \delta_{\ell m}$. As might be expected, this alteration does not radically alter the shape functions (see Figure 3.3) nor the eventual COD solution on the crack. However, there are significant changes to the formulas for the stress intensity factors, and this is reflected in much more accurate results for mixed mode problems, see Gray et al. [51].

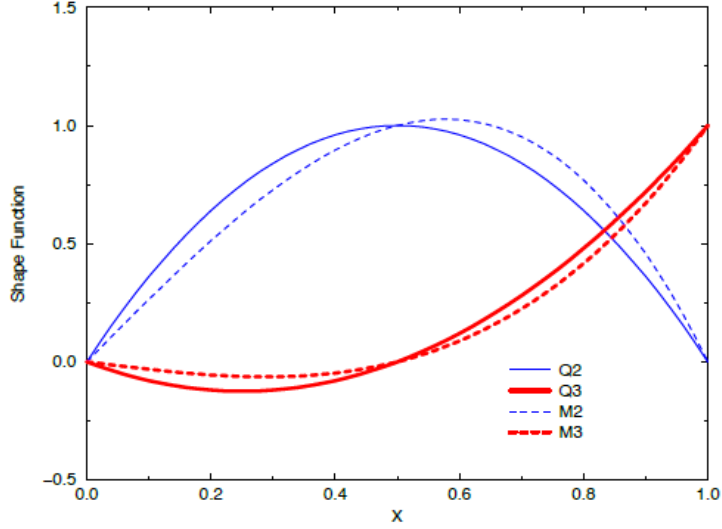


Figure 3.3: Standard ($Q2, Q3$) and modified ($M2, M3$) quarter-point shape functions.

The results reported in this paper employ the Displacement Correlation Technique (DCT) to compute the mode-I and mode-II stress intensity factors, K_I, K_{II} . With the modified quarter-point element, accurate results can be achieved, even with this very simple evaluation method. The general expression for the stress intensities by means of the DCT technique are

$$\begin{aligned}
 K_I &= \frac{\mu}{\kappa + 1} \lim_{r \rightarrow 0} \sqrt{\frac{2\pi}{r}} \Delta u_n \\
 K_{II} &= \frac{\mu}{\kappa + 1} \lim_{r \rightarrow 0} \sqrt{\frac{2\pi}{r}} \Delta u_t
 \end{aligned} \tag{3.8}$$

where Δu_n and Δu_t are the normal and tangential components of the displacement jump vector, respectively, $\kappa = 3 - 4\nu$ for plane strain and $\kappa = \frac{3-\nu}{1+\nu}$ for plane stress. As discussed in Gray et al. [51], with the modified quarter-point these become

$$\begin{aligned}
 K_I &= \frac{\mu}{3(\kappa + 1)} \sqrt{\frac{2\pi}{L}} (8\Delta u_n(B) - \Delta u_n(C)) \\
 K_{II} &= \frac{\mu}{3(\kappa + 1)} \sqrt{\frac{2\pi}{L}} (8\Delta u_t(B) - \Delta u_t(C))
 \end{aligned} \tag{3.9}$$

where the nodes $\{B, C\}$ are defined in Figure 3.4. Thus, K_I, K_{II} are given directly in terms of the nodal values of the crack opening displacement on the crack tip element.

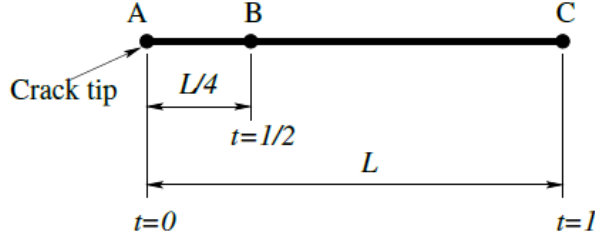


Figure 3.4: Crack tip element.

In order to extend the crack, a crack extension criterion must be selected. Here, we use the maximum principal stress criterion of Erdogan and Sih [94] where the crack grows in a direction perpendicular to the maximum principal stress. The crack extension angle, θ_c can be calculated from the condition $\sigma_{r\theta} = 0$ ahead of the crack as

$$K_I \sin \theta_c + K_{II}(3 \cos \theta_c - 1) = 0 \quad (3.10)$$

The crack extension simulation can proceed in a straightforward manner by performing the SGBEM analysis, computing K_I, K_{II} from Eq.(3.9), computing θ_c from Eq.(3.10), then extending the crack by a small amount Δa in the direction of the crack extension. The crack extension is accomplished by adding a new modified quarter point element to the tip of the crack, and reverting the previous crack-tip element to a standard element. For the simulations reported on here, crack extension will only occur in the matrix material, we terminate our calculations if the crack impinges on an interface due to the increased complexity of the crack-tip stress field. As noted in Williams, et al. [52], the SGBEM with modified quarter-point crack elements is capable of producing highly accurate results for both crack path and stress intensities, even when the crack tip is extremely close to interface boundaries.

3.3 Effect of a Single Auxetic Particle on the Crack Path

In order to validate our analysis, we will use a problem geometry identical to that used in Williams, et al. [52], see Figure 3.5, and benchmark our analysis against results for non-auxetic particles. With reference to the figure, we will use $L = 0.150$ m and $h = 0.04$ m in our calculations. The origin of coordinates is located at the crack tip, and the initial crack length is $h/4$. The changes in crack length in the x and y directions are normalized with respect to the half-length $L/2$ and the height of the beam, h , respectively. The particle radius is denoted by r which is selected to be very small ($r = 0.001$ m). The particle is centered vertically in the beam but offset from the crack path an amount $x = -r$ from the y -axis.

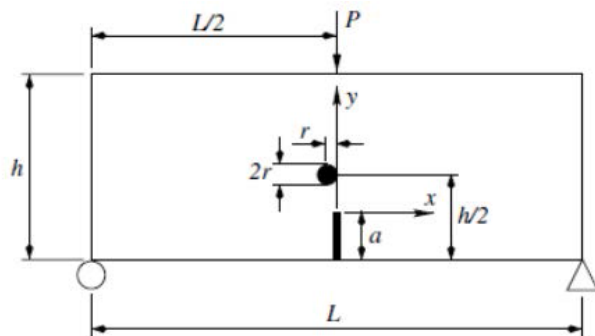


Figure 3.5: Three-point bend specimen.

We first consider non-auxetic particles, with $\nu_p/\nu_m = 1$, and compute the crack path when E_p/E_m varies from 2 to 16. We use 193 quadratic elements on the outer boundary for this problem, 64 quadratic elements for the particle, and initially 10 elements for the crack. We take crack extension increments of $\Delta a = 0.03$ mm. These values provided good agreement with published results. The results for the crack path are shown in Figure 3.6, where the results from Williams, et al. [52] are also plotted, but are directly on top of the results of our calculations. As such, we are confident in the accuracy of the results for the subsequent analyses reported here. Note in the figure that for $2 \leq E_p/E_m \leq 16$ the crack is always deflected away from the particle when $\nu_p/\nu_m = 1$ with the amount of deflection

increasing with E_p/E_m . It was also noted in Williams, et al. [52] that the ratio ν_p/ν_m only has a slight influence on crack deflection when E_p/E_m is large, but has a pronounced effect on the crack path at lower values of E_p/E_m . This is consistent with the results reported in Knight et al. [89].

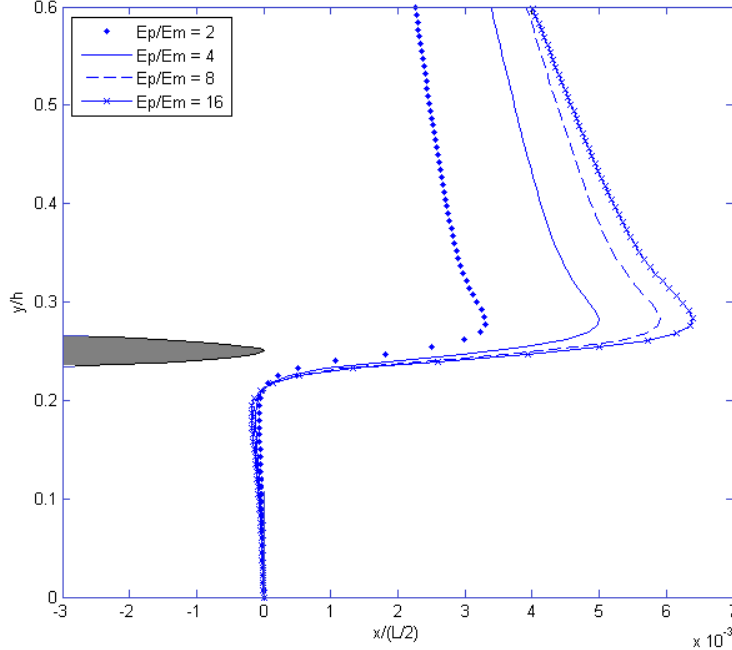


Figure 3.6: Comparison of results with Williams, et al. (2007) [52] for non-auxetic particle-crack interaction, $\nu_p/\nu_m = 1$. Note that the horizontal scale is expanded to emphasize the crack path.

We next perform an analysis similar to our benchmark analysis, but the particle is taken to be auxetic: $\nu_p/\nu_m = -1$. We investigate the effects of the mismatch in Young's modulus on crack extension by again varying E_p/E_m from 2 to 16. Our simulation results are shown in Figure 3.7. In contrast to the results shown in Figure 3.6 for the non-auxetic particle, we see that for lower values of E_p/E_m ($E_p/E_m = 2, 4$) the auxetic particle actually attracts the crack. When the particle is stiffer than the matrix material ($E_p/E_m = 8, 16$) the crack is deflected away from the particle as it is in the case of the non-auxetic particle.

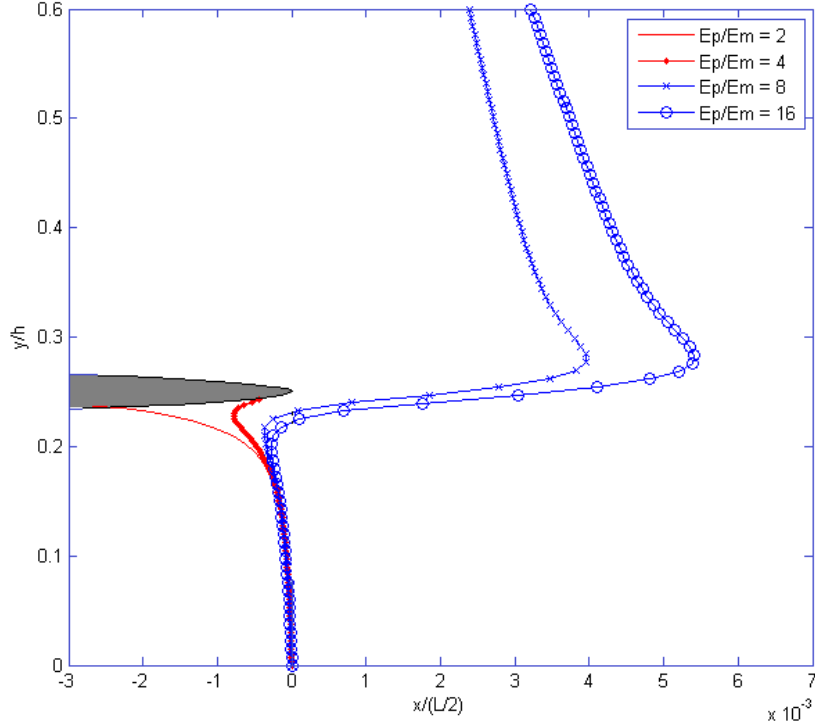


Figure 3.7: Crack extension near an auxetic particle, $\nu_p/\nu_m = -1$. Note that the horizontal scale is expanded to emphasize the crack path.

It is interesting to study the stress intensity factors as the crack approaches both a non-auxetic and an auxetic particle. First, consider the case $E_p/E_m = 2$ where the crack is deflected from the non-auxetic particle, and is attracted (and perhaps pinned) for the auxetic particle. In Figure 3.8 we plot the mode-I stress intensity factor, K_I , normalized by the mode-I stress intensity factor for the three-point bending specimen in the absence of a particle, K_{I0} , as given in Tada, et al. [95]. The figure shows the normalized stress intensity K_I/K_{I0} plotted versus the normalized vertical crack-tip position, y/h . The effect of the particle becoming auxetic is profound. As the crack approaches the particle, we see K_I/K_{I0} decrease for the case of the non-auxetic particle, and increase for the case of the auxetic particle.

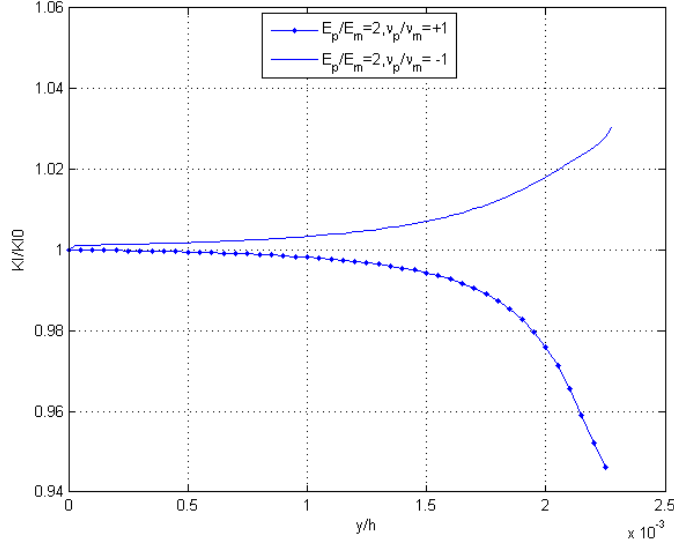


Figure 3.8: Normalized mode-I stress intensity factor versus crack-tip position for $E_p/E_m = 2$, $\nu_p/\nu_m = \pm 1$.

The mode-II stress intensity factors are also dramatically effected by the particle becoming auxetic. With reference to Figure 3.7 and Eq.(3.10), this must be true as the crack kinks in an opposite direction (toward the particle) when compared to the crack extension toward a non-auxetic particle. In Figure 3.9 we have plotted the normalized mode-II stress intensity factor, K_{II}/K_{II0} , again for $E_p/E_m = 2$ and $\nu_p/\nu_m = \pm 1$. In the case of the non-auxetic particle (where the crack is deflected), the mode-II stress intensity is increasingly positive as the crack approaches the particle, causing the crack to kink away from the particle and deflect. In the case of the auxetic particle, the mode-II stress intensity is negative, causing the crack to kink toward the particle.

We next consider the behavior of the stress intensity factors for a case where the crack is deflected away from the particle for both the auxetic and non-auxetic particle. We take $E_p/E_m = 8$, $\nu_p/\nu_m = \pm 1$, and plot K_I/K_{I0} versus y/h in Figure 3.10. For this moduli ratio we see the shielding of stress intensity commonly associated with a crack approaching a particle, and the amplification of the stress intensity as the crack passes the particle. The amount of shielding and amplification of the stress intensity is nearly identical for the auxetic

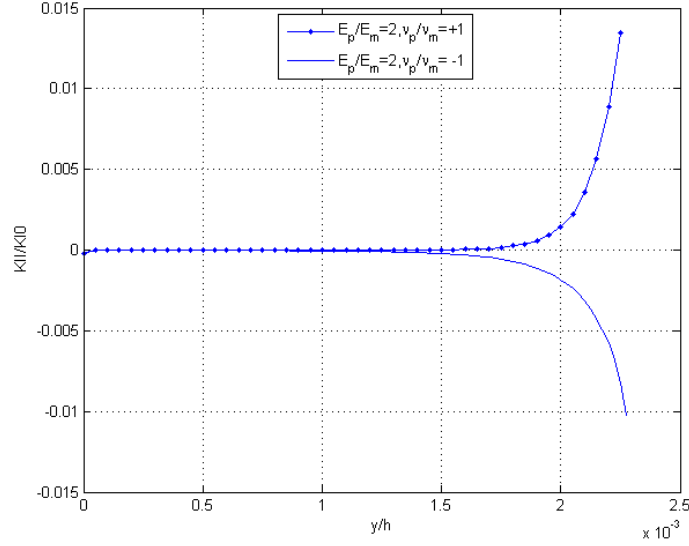


Figure 3.9: Normalized mode-II stress intensity factor versus crack-tip position for $E_p/E_m = 2$, $\nu_p/\nu_m = \pm 1$.

particle and the non-auxetic particle. It seems that once the crack is deflected away from the particle, the mode-I stress intensity is not effected significantly. However, the peak of the shielded stress intensity occurs slightly sooner for the non-auxetic particle than it does for the auxetic particle.

One natural question to ask concerns the crack extension behavior when the auxetic particle is soft in comparison to the matrix material ($E_p/E_m < 1$) versus when the particle is relatively hard ($E_p/E_m > 1$). Here we present results for soft and hard particles, comparing the extension behavior when $\nu_p/\nu_m = 1$ and when $\nu_p/\nu_m = -1$. We use $E_p/E_m = 0.5$ for the soft particle and $E_p/E_m = 2$ for hard particle. As can be seen in Figure 3.11, the crack is attracted to the auxetic inclusion, but this attraction varies slightly for the soft and hard particles. If the particle is non-auxetic, the crack is attracted only towards the soft inclusion, while defects away from the hard particle as shown in the figure. In summary, we note that the soft particle attracts the crack whether it is auxetic or not. However, a significant increase in the attraction can clearly be seen for the case of the auxetic particle.

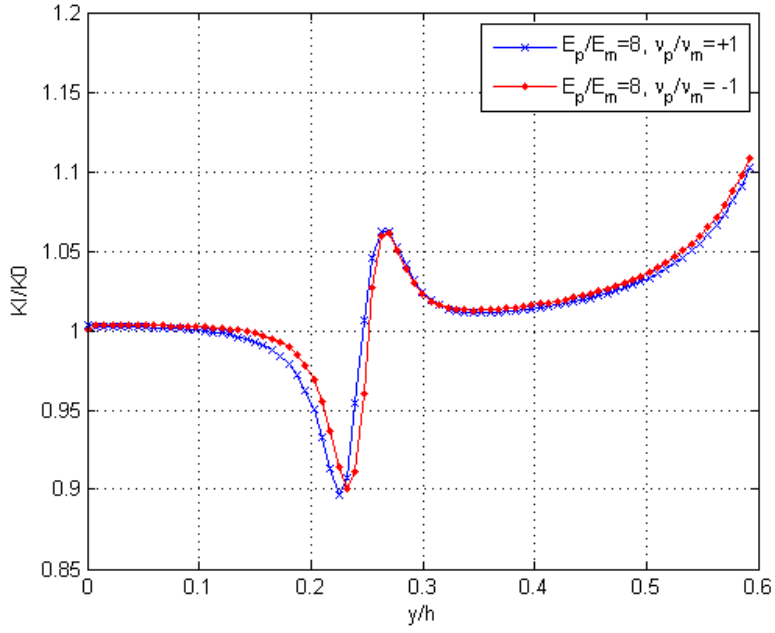


Figure 3.10: Normalized mode-I stress intensity factor versus crack-tip position for $E_p/E_m = 8$, $\nu_p/\nu_m = \pm 1$.

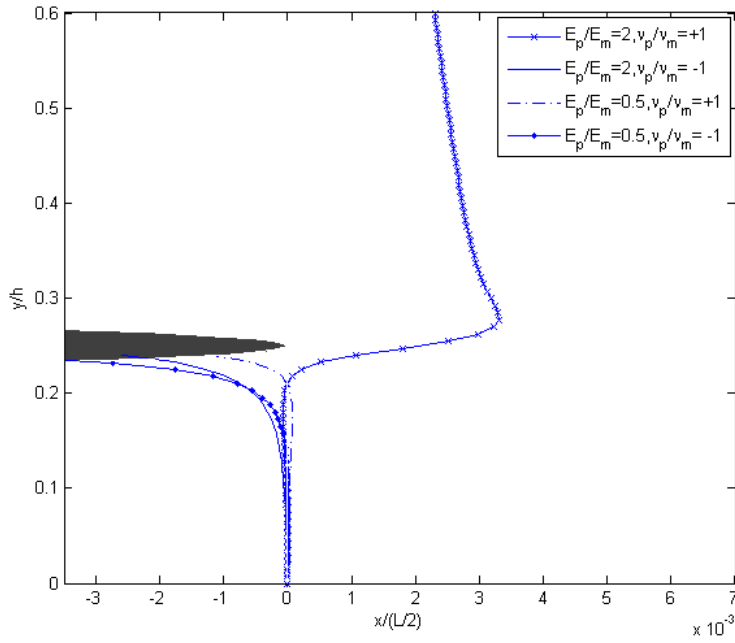


Figure 3.11: Crack extension near a particle, $\nu_p/\nu_m = \pm 1$, for $E_p/E_m = 0.5$ and $E_p/E_m = 2$.

Table 3.1: The behavior of crack path in presence of soft or hard particle.

| No. | Particle type | ν_p/ν_m | Crack behavior |
|-----|---------------|---------------|----------------|
| 1 | soft | 1 | attracted |
| 2 | soft | -1 | attracted |
| 3 | hard | 1 | deflected |
| 4 | hard | -1 | attracted |

3.4 Effect of Double Auxetic Particles on the Crack Path

Also, we have investigated the effect of two auxetic particles on the crack path direction. The geometry of this problem is already described in the previous section and illustrated in Figure 3.5, except that now an auxetic particle is added, which has the same elastic constants, selected to be placed above the first particle and offset in the positive direction of x , an amount r from the y -axis, where the two particles have the same horizontal tangential line.

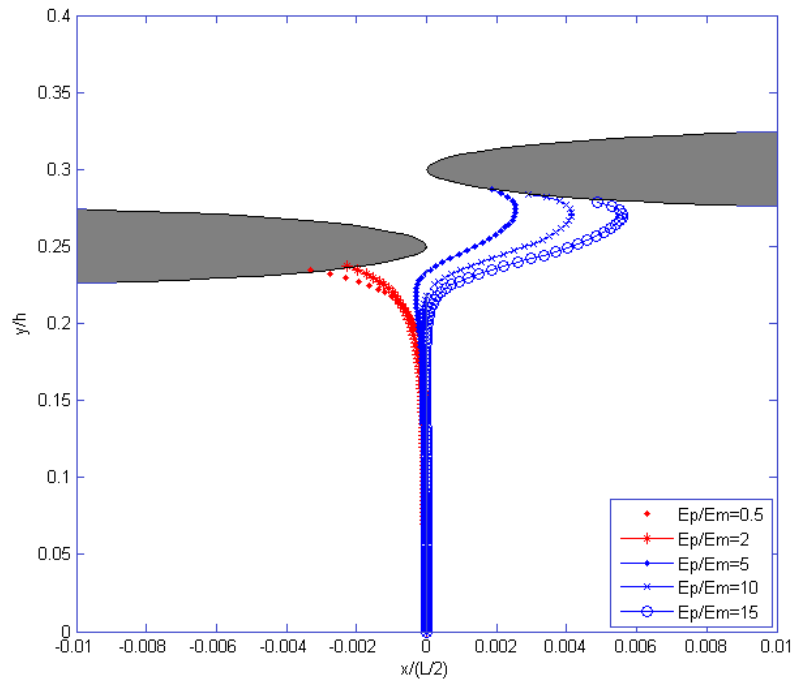


Figure 3.12: Effect of E_P/E_m on crack deflection in existence of two particles.

As mentioned in the previous examples, in single particle case, the crack is attracted to the first inclusion, as the Young's modulus ratio (E_p/E_m) is less than 5. For large Young's modulus ratio, the crack deflects away from the first inclusion to collide with the second inclusion as it passes through the small distance between the two inclusions as shown in Figure 3.12.

3.5 Summary

We employed a symmetric Galerkin based boundary element method to analyze crack extension near an auxetic particle. We found that the crack extension behavior can be dramatically different near an auxetic particle when compared to extension behavior near a non-auxetic particle. For values of $E_p/E_m = 2, 4$ we found that the crack was attracted to the particle when $\nu_p/\nu_m = -1$, yet when $\nu_p/\nu_m = 1$ the crack is deflected away from the particle. We also found that when $E_p/E_m = 8, 16$ the crack was deflected away from the particle when $\nu_p/\nu_m = \pm 1$. This suggests strategies for pinning extending matrix cracks by employing auxetic particles that tend to attract the crack. Indeed, we found that a soft particle ($E_p/E_m = 0.5$) will attract the crack when $\nu_p/\nu_m = \pm 1$, but if the particle was hard ($E_p/E_m = 0.5$) the crack was only attracted when $\nu_p/\nu_m = -1$.

CHAPTER 4
WAVE PROPAGATION IN AUXETIC COMPOSITE MATERIAL

In this chapter, we investigate the effects of auxetic material on the wave propagation through its amplitude ratio. Three different wave types are selected, SH-waves, and P-waves in two half-spaces and the SH-wave propagation in layered half-space. Each problem will be reviewed and studied in a separate section and we will show the results in each section and a summary will be given at the end of the chapter.

4.1 Reflection and transmission of SH waves in two half spaces

This section contains the analysis of the first problem, propagation of SH-wave in two half-spaces. The material of the upper half is an auxetic material.

4.1.1 Mathematical formulation

This section reviews the plane harmonic waves, SH-wave type, following Achenbach [53]. The displacement of a plane harmonic wave in one dimension is

$$\mathbf{u} = A \mathbf{d} \exp[ik(\mathbf{x} \cdot \mathbf{p} - ct)] \quad (4.1)$$

where A is the amplitude of the wave, \mathbf{d} is the unit vector for the direction of wave motion, \mathbf{p} is the unit vector for the direction of wave propagation, \mathbf{d} and \mathbf{p} have the same direction in the case of the longitudinal wave (the harmonic motion in the direction of the wave propagation) and they are perpendicular to each other in the case of the transverse wave (the harmonic motion normal to the direction of propagation). Also, \mathbf{x} is the Cartesian position and t denotes the time, k is the wave number where $k = \frac{\omega}{c}$ and c is velocity of propagation.

If the wave is longitudinal, then the velocity $c = \alpha$ and

$$c = \alpha = \left(\frac{\lambda + 2\mu}{\rho} \right)^{\frac{1}{2}}. \quad (4.2)$$

If the wave is transverse, then the velocity $c = \beta$ and

$$c = \beta = \left(\frac{\mu}{\rho} \right)^{\frac{1}{2}} \quad (4.3)$$

where λ and μ are Lamé's elastic constants, and ρ is the mass density. Also, the relationship between the longitudinal and transverse speed is expressed as follows

$$\kappa = \frac{\alpha}{\beta} = \left(\frac{\lambda + 2\mu}{\mu} \right)^{\frac{1}{2}} = \left[\frac{2(1 - \nu)}{1 - 2\nu} \right]^{\frac{1}{2}} \quad (4.4)$$

and

$$\frac{\beta_1}{\beta_2} = \sqrt{\left(\frac{1 - \nu_2}{1 - \nu_1} \right) \left(\frac{1 - 2\nu_1}{1 - 2\nu_2} \right)} \quad (4.5)$$

In general, the problem of wave propagation in two half-spaces, as shown in Figure 4.1,

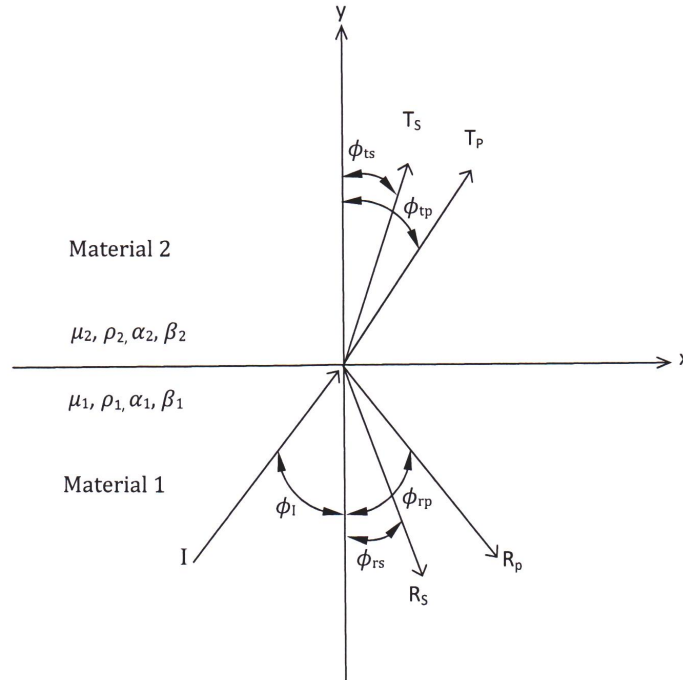


Figure 4.1: Propagation of plane waves in two half-spaces

consists of two half-spaces with different elastic properties (μ , ρ and λ), bonded together at the interface ($y = 0$). The incident wave is represented by the letter I . R and T stand for reflected and transmitted waves, respectively. The subscripts s and p denote the S-

and P-waves, and the subscripts 1 and 2 indicate the different materials. We consider the displacement and stress to be continuous at the interface. In two dimensions, we rewrite the displacement equation as

$$\mathbf{u} = A \mathbf{d} \exp[ik(\mathbf{x} \cdot \mathbf{p}_x + \mathbf{y} \cdot \mathbf{p}_y - ct)]. \quad (4.6)$$

Achenbach [53] defined and summarized the vectors \mathbf{p}_x and \mathbf{p}_y for reflected and transmitted waves for both the longitudinal and transverse waves as follows,

Reflected longitudinal wave:

$$\mathbf{p}_x = \sin \phi_{rp}, \quad \mathbf{p}_y = -\cos \phi_{rp}, \quad c = \alpha_1. \quad (4.7)$$

Reflected transverse wave:

$$\mathbf{p}_x = \sin \phi_{rs}, \quad \mathbf{p}_y = -\cos \phi_{rs}, \quad c = \beta_1. \quad (4.8)$$

Transmitted longitudinal wave:

$$\mathbf{p}_x = \sin \phi_{tp}, \quad \mathbf{p}_y = \cos \phi_{tp}, \quad c = \alpha_2. \quad (4.9)$$

Transmitted transverse wave:

$$\mathbf{p}_x = \sin \phi_{ts}, \quad \mathbf{p}_y = \cos \phi_{ts}, \quad c = \beta_2. \quad (4.10)$$

Figure 4.2 illustrates SH-wave propagation in two half-spaces, they are made from two isotropic, homogenous materials; material 1 in the lower half plane ($y < 0$), and material 2 in the upper half plane ($y > 0$). The incident SH-wave, I_{SH} , produces two SH-waves when it impinges at the interface $y = 0$, R_s and T_s , which are the reflected and transmitted SH-waves.

The incident SH-wave, I_{SH} , causes a displacement in the z -direction, which is represented by the equation

$$(u_z)_I = I_{SH} \exp[ik_I(x \sin \phi_I + y \cos \phi_I - \beta_1 t)]. \quad (4.11)$$

The shear stress is obtained from

$$\tau_{yz} = \mu u_{z,y} = \mu \frac{\partial u_z}{\partial y} \quad (4.12)$$

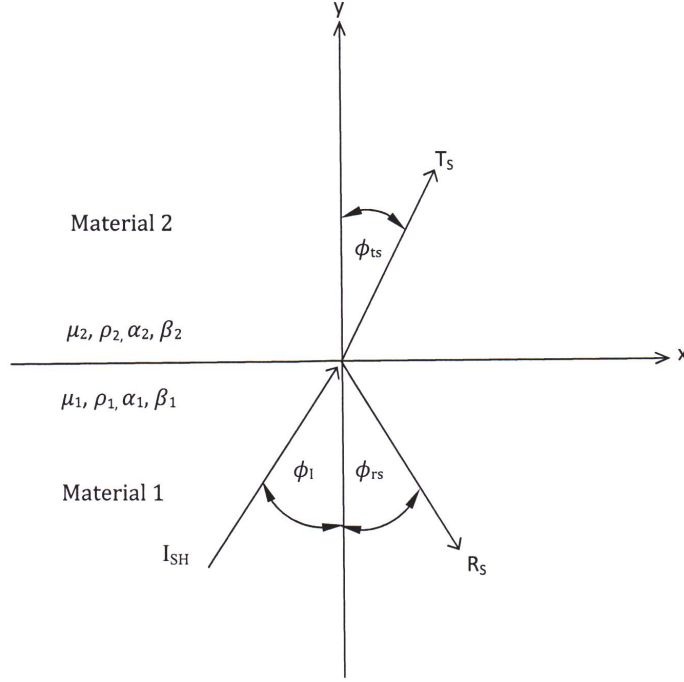


Figure 4.2: Propagation of SH-waves in two half-spaces

where

$$(\tau_{yz})_I = ik_I \mu_1 I_{SH} \cos \phi_I \exp[ik_I(x \sin \phi_I + y \cos \phi_I - \beta_1 t)]. \quad (4.13)$$

The stress and displacement equations for the reflected and transmitted waves are:

The reflected SH-wave (R_s):

$$(u_z)_R = R_s \exp[ik_{rs}(x \sin \phi_{rs} - y \cos \phi_{rs} - \beta_1 t)], \quad (4.14)$$

$$(\tau_{yz})_R = -ik_{rs} \mu_1 R_s \cos \phi_{rs} \exp[ik_{rs}(x \sin \phi_{rs} - y \cos \phi_{rs} - \beta_1 t)]. \quad (4.15)$$

The transmitted SH-wave (T_s):

$$(u_z)_T = T_s \exp[ik_{ts}(x \sin \phi_{ts} + y \cos \phi_{ts} - \beta_1 t)], \quad (4.16)$$

$$(\tau_{yz})_T = ik_{ts} \mu_2 T_s \cos \phi_{ts} \exp[ik_{ts}(x \sin \phi_{ts} + y \cos \phi_{ts} - \beta_2 t)]. \quad (4.17)$$

Since the equations must be satisfied for all values of x and t , the exponentials must be equal, so [53]

$$k_I \sin \phi_I = k_{rs} \sin \phi_{rs} = k_{ts} \sin \phi_{ts}, \quad (4.18)$$

$$k_I \beta_1 = k_{rs} \beta_1 = k_{ts} \beta_2, \quad (4.19)$$

$$k_{rs} = k_I, \quad \phi_I = \phi_{rs}, \quad (4.20)$$

$$k_{ts} = (\beta_1/\beta_2)k_I, \quad (4.21)$$

$$\sin \phi_{ts} = (\beta_2/\beta_1) \sin \phi_I. \quad (4.22)$$

The displacement u_z and the shear stress τ_{yz} at the plane $y = 0$ are continuous, which leads to two equations for R_s and T_s in terms of I_{SH} :

$$(u_z)_I + (u_z)_R = (u_z)_T, \quad (4.23)$$

$$(\tau_{yz})_I + (\tau_{yz})_R = (\tau_{yz})_T. \quad (4.24)$$

By substituting the equations of the displacement and the stress, Eqs. (4.11) and (4.13 - 4.17), into the equations (4.23) and (4.24) we obtain

$$I_{SH} + R_s = T_s, \quad (4.25)$$

$$I_{SH} \mu_1 \cos \phi_I - R_s \mu_1 \cos \phi_I = T_s \mu_2 \left(\frac{\beta_1}{\beta_2}\right) \cos \phi_{ts}. \quad (4.26)$$

These two equations, Eqs. (4.25) and (4.26), can be written in matrix form as

$$I_{SH} \begin{bmatrix} 1 \\ \mu_1 \cos \phi_I \end{bmatrix} = \begin{bmatrix} -1 & 1 \\ \mu_1 \cos \phi_I & \mu_2(\beta_1/\beta_2) \cos \phi_{ts} \end{bmatrix} \begin{bmatrix} R_s \\ T_s \end{bmatrix}$$

The amplitude ratios are then

$$\frac{1}{I_{SH}} \begin{bmatrix} R_s \\ T_s \end{bmatrix} = \frac{-1}{\mu_1 \cos \phi_I + \mu_2(\beta_1/\beta_2) \cos \phi_{ts}} \begin{bmatrix} \mu_2(\beta_1/\beta_2) \cos \phi_{ts} & -1 \\ -\mu_1 \cos \phi_I & -1 \end{bmatrix} \begin{bmatrix} 1 \\ \mu_1 \cos \phi_I \end{bmatrix}.$$

or,

$$\frac{R_s}{I_{SH}} = \frac{\mu_1 \cos \phi_I - \mu_2(\beta_1/\beta_2) \cos \phi_{ts}}{\mu_1 \cos \phi_I + \mu_2(\beta_1/\beta_2) \cos \phi_{ts}}, \quad (4.27)$$

$$\frac{T_s}{I_{SH}} = \frac{2\mu_1 \cos \phi_I}{\mu_1 \cos \phi_I + \mu_2(\beta_1/\beta_2) \cos \phi_{ts}}. \quad (4.28)$$

where (R_s/I_{SH}) and (T_s/I_{SH}) are the amplitude ratios for reflected and transmitted SH-wave, respectively, in two half-spaces.

4.1.2 Results and Discussion

We consider two half-spaces. The lower half-plane contains a material that has a Poisson's ratio of $\nu = 0.3$. We aim to investigate the change in the amplitude of transmitted and reflected waves with respect to the amplitude of an incident wave, depending on the change in Poisson's ratio of the material in the upper half-space. We have selected certain values for the material properties, such as Young's modulus and density, to avoid the complex values of the amplitude results. As seen in Figures 4.3 and 4.4, there are always combinations of material properties and incident angle for values of Poisson's ratio between -0.85 and 0.4 where the wave is totally transmitted and there is no reflected wave. The amplitude of the transmitted wave is less than 55% of the amplitude of the incident wave. This is just for incident angle less than 70° . At the incident angle $\phi_I = 90^\circ$ for all values of Poisson's ratio, the amplitude ratio of the reflected SH-wave $R_s/I_{SH} = -1$ and the amplitude ratio of the transmitted SH-wave $T_s/I_{SH} = 0$. That means there is no transmitted wave which is logical because the wave travels parallel to the interface in one material.

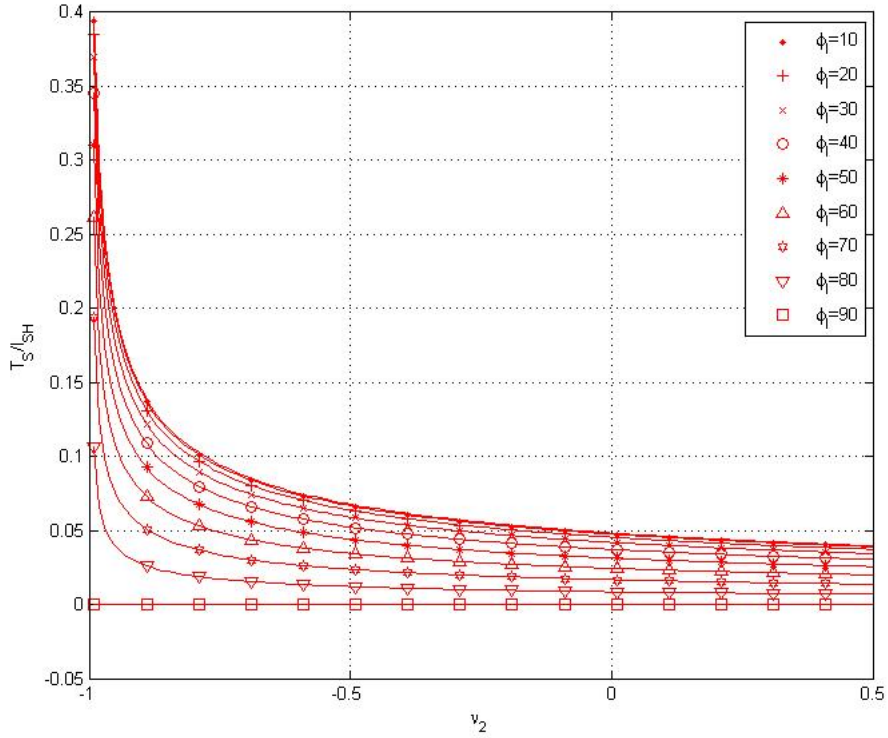


Figure 4.3: Transmitted SH-wave in two half-spaces (T_S/I_{SH}), amplitude ratios vs. Poisson's ratio.

Figures 4.6 and 4.7 show curves of amplitude ratio vs. the incident angle, from 0° (normal on the interface) to 90° (parallel to the interface). In materials with a positive Poisson's ratio, there is no reflected wave, and the wave totally transmits only in the range of incident angle $74^\circ - 77^\circ$ for all the combinations of material properties. In materials with a negative Poisson's ratio, there is no reflected wave, and the wave totally transmits only in the range of incident angle $15^\circ - 74^\circ$ for $-0.92 < \nu_2 < 0$, and $0 < \nu_1 < 0.5$ for all the combinations of material properties. At these points, the amplitude ratio of the transmitted wave is equal to $+1$, which means total transmission case. In the range $-1 < \nu_2 < -0.92$ there will always be reflected and transmitted waves. These limits change slightly up and down depending on material properties used in calculations.

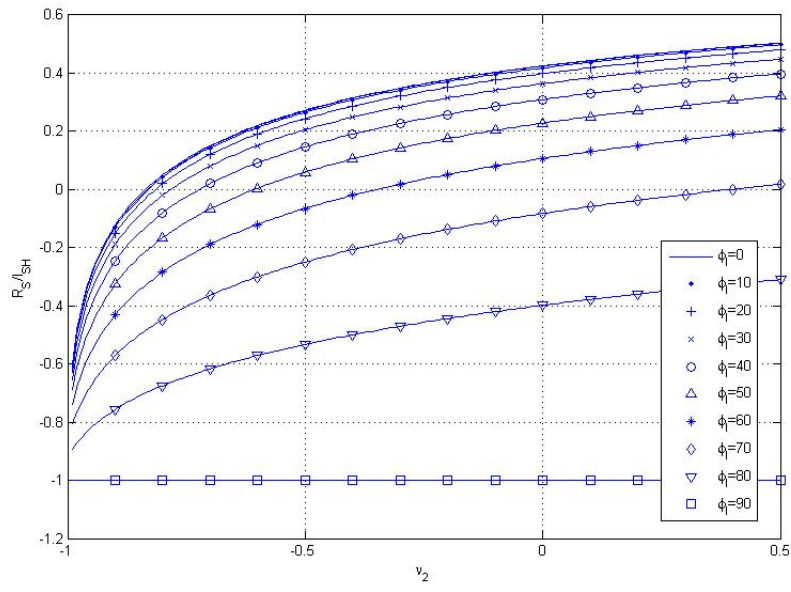


Figure 4.4: Reflected SH-wave in two half-spaces (R_S/I_{SH}), amplitude ratio vs. Poisson's ratio.

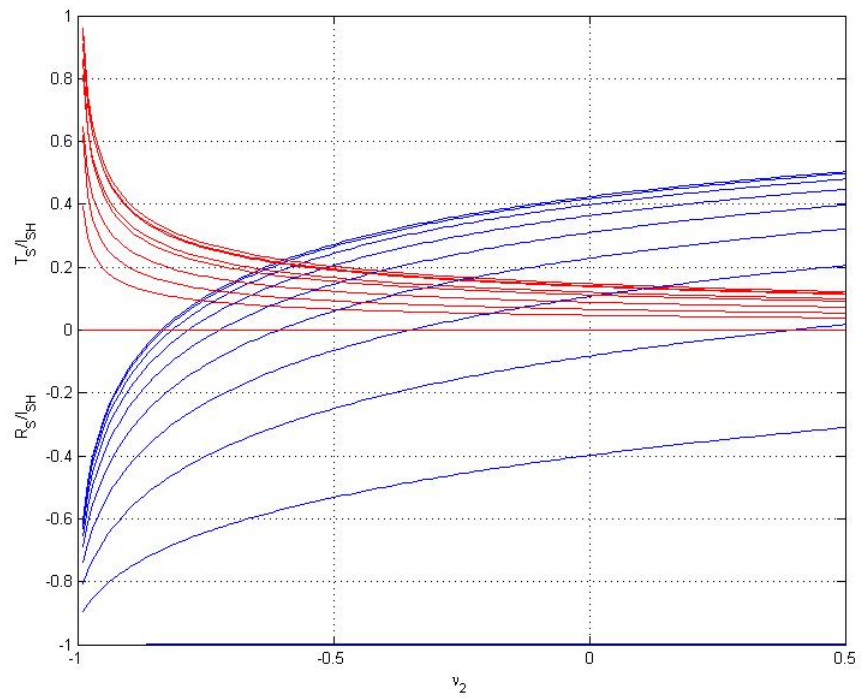


Figure 4.5: The transmitted and reflected SH-waves in one plot compared to each other.

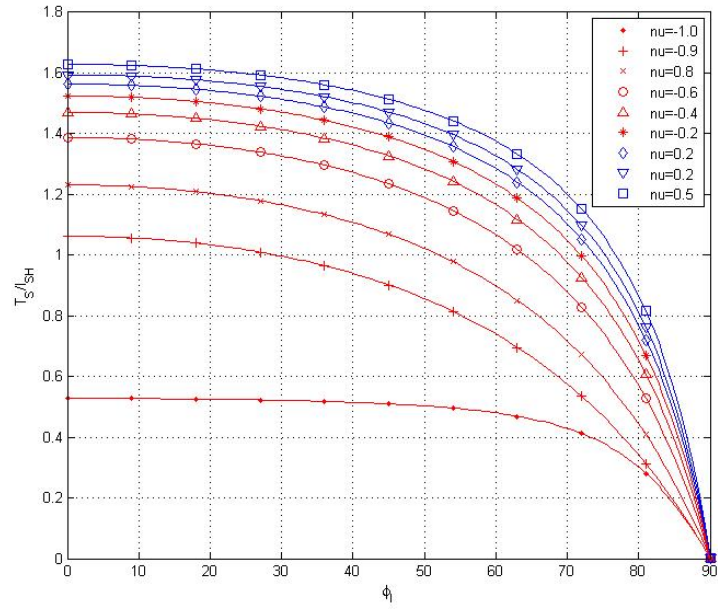


Figure 4.6: Transmitted SH-wave, the amplitude ratio as a function in the incident angle for various values of Poisson's ratio.

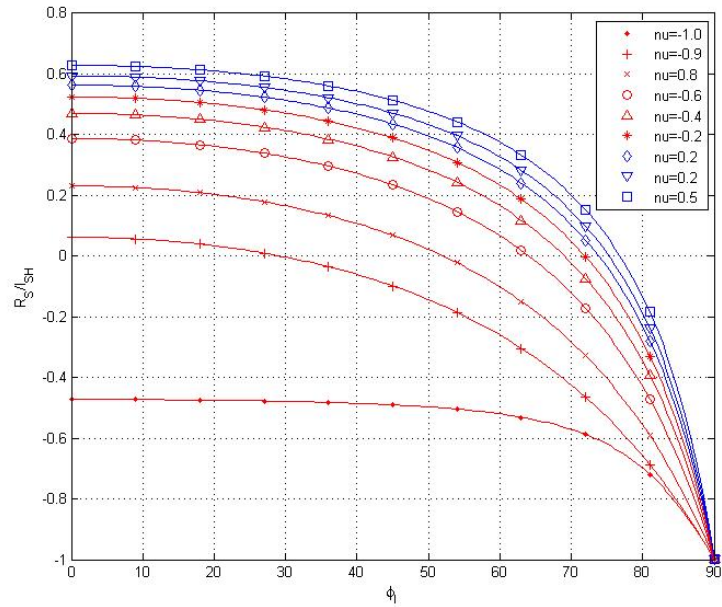


Figure 4.7: Reflected SH-wave, the amplitude ratio as a function in the incident angle for various values of Poisson's ratio.

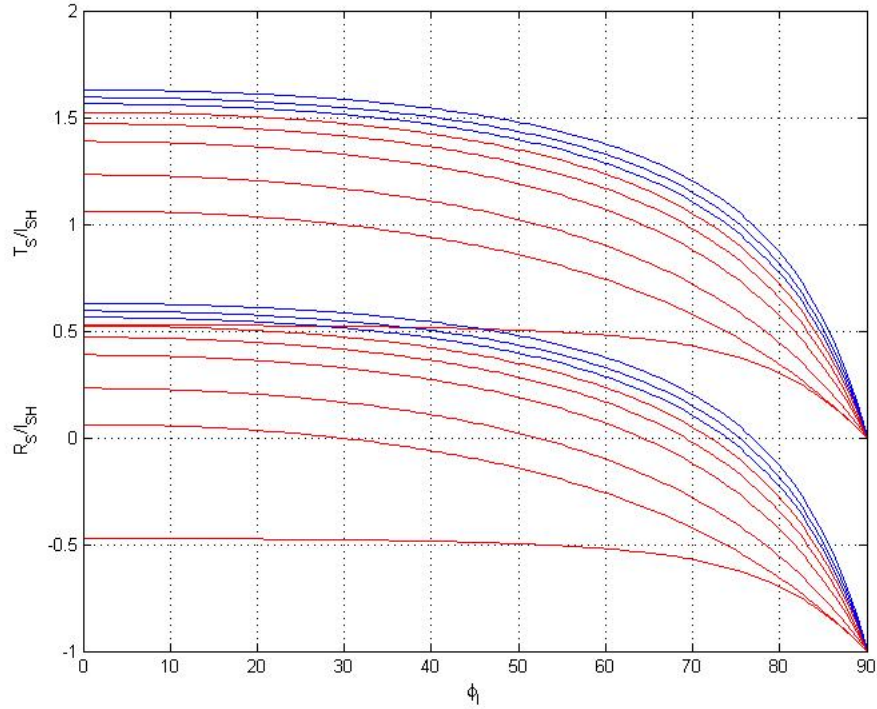


Figure 4.8: The transmitted and reflected waves as a function in the incident angle in one plot compared to each other.

4.2 Reflection and transmission of P-waves in two half-spaces

Here, we will study the P-wave propagation in two half-spaces and investigate the effect of auxetic material on the amplitude of reflected and transmitted wave. Also, we consider the material of the upper half-space is auxetic.

4.2.1 Mathematical formulation

In this section, we will review the derivation of Achenbach [53] for the amplitude ratios of an incident P-wave in two half-spaces. The problem considered is shown in Figure 4.9. The incident P-waves produces both a reflected and transmitted P-waves and SV-waves when impinging on an interface between two media. In general, the incident, reflected and transmitted waves are represented by their displacements and stresses [53] as

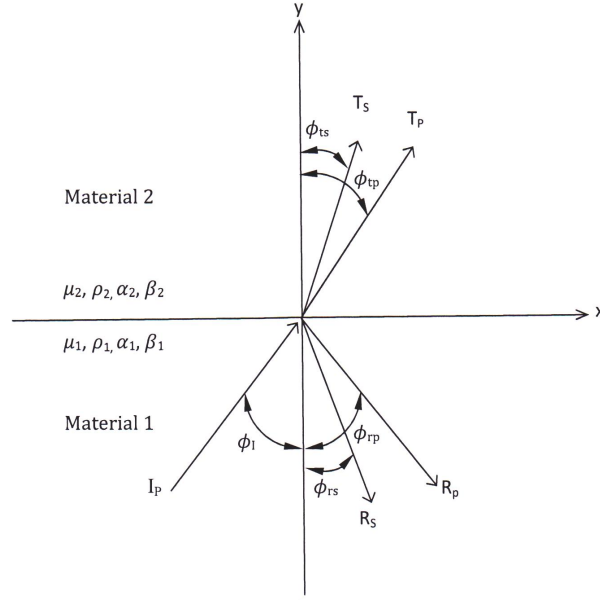


Figure 4.9: Propagation of P-waves in two half-spaces.

$$u_x = A \mathbf{d}_x \exp(i\zeta), \quad (4.29)$$

$$u_y = A \mathbf{d}_y \exp(i\zeta), \quad (4.30)$$

$$\tau_{yy} = ikA[(\lambda + 2\mu)d_y p_y + \lambda d_x p_x] \exp(i\zeta), \quad (4.31)$$

$$\tau_{yx} = ikA[(\lambda + 2\mu)d_y p_x + \lambda d_x p_y] \exp(i\zeta), \quad (4.32)$$

$$\text{and } \zeta = k(x \sin \phi + y \cos \phi - ct). \quad (4.33)$$

where \mathbf{d}_x and \mathbf{d}_y are the unit vectors for the direction of wave motion in x and y-directions, respectively. On $y = 0$, the stresses and the displacements are continuous, the term $y \cos \phi$ will disappear so ζ will become

$$\zeta = k(x \sin \phi - ct). \quad (4.34)$$

Now, equations (4.29)-(4.32) and (4.34) will be repeated for five waves, the incident P-wave, reflected P and S waves and transmitted P and S waves as follows:

The incident wave (I_P):

$$d_x = \sin \phi_I, \quad d_y = \cos \phi_I, \quad p_x = \sin \phi_I, \quad p_y = \cos \phi_I, \quad (4.35)$$

$$(u_x)_I = I_P \sin \phi_I \exp[ik_I(x \sin \phi_I - \alpha_1 t)], \quad (4.36)$$

$$(u_y)_I = I_P \cos \phi_I \exp[ik_I(x \sin \phi_I - \alpha_1 t)], \quad (4.37)$$

$$(\tau_{yy})_I = ik_I I_P (\lambda_1 + 2\mu_1 \cos^2 \phi_I) \exp[ik_I(x \sin \phi_I - \alpha_1 t)], \quad (4.38)$$

$$(\tau_{yx})_I = 2ik_I \mu_1 I_P \sin \phi_I \cos \phi_I \exp[ik_I(x \sin \phi_I - \alpha_1 t)]. \quad (4.39)$$

The reflected P-wave (R_P):

$$d_x = \sin \phi_{rp}, \quad d_y = -\cos \phi_{rp}, \quad p_x = \sin \phi_{rp}, \quad p_y = -\cos \phi_{rp}, \quad (4.40)$$

$$(u_x)_{rp} = R_P \sin \phi_{rp} \exp[ik_{rp}(x \sin \phi_{rp} - \alpha_1 t)], \quad (4.41)$$

$$(u_y)_{rp} = -R_P \cos \phi_{rp} \exp[ik_{rp}(x \sin \phi_{rp} - \alpha_1 t)], \quad (4.42)$$

$$(\tau_{yy})_{rp} = ik_{rp} R_P (\lambda_1 + 2\mu_1 \cos^2 \phi_{rp}) \exp[ik_{rp}(x \sin \phi_{rp} - \alpha_1 t)], \quad (4.43)$$

$$(\tau_{yx})_{rp} = -2ik_{rp} \mu_1 R_P \sin \phi_{rp} \cos \phi_{rp} \exp[ik_{rp}(x \sin \phi_{rp} - \alpha_1 t)]. \quad (4.44)$$

The reflected S-wave (R_S):

$$d_x = \cos \phi_{rs}, \quad d_y = \sin \phi_{rs}, \quad p_x = \sin \phi_{rs}, \quad p_y = -\cos \phi_{rs}, \quad (4.45)$$

$$(u_x)_{rs} = R_S \cos \phi_{rs} \exp[ik_{rs}(x \sin \phi_{rs} - \beta_1 t)], \quad (4.46)$$

$$(u_y)_{rs} = R_S \sin \phi_{rs} \exp[ik_{rs}(x \sin \phi_{rs} - \beta_1 t)], \quad (4.47)$$

$$(\tau_{yy})_{rs} = -2ik_{rs}R_S\mu_1 \sin \phi_{rs} \cos \phi_{rs} \exp[ik_{rs}(x \sin \phi_{rs} - \beta_1 t)], \quad (4.48)$$

$$(\tau_{yx})_{rs} = ik_{rs}\mu_1 R_S(\sin^2 \phi_{rs} - \cos^2 \phi_{rs}) \exp[ik_{rs}(x \sin \phi_{rs} - \beta_1 t)]. \quad (4.49)$$

The transmitted P-wave (T_P):

$$d_x = \sin \phi_{tp}, \quad d_y = \cos \phi_{tp}, \quad p_x = \sin \phi_{tp}, \quad p_y = \cos \phi_{tp}, \quad (4.50)$$

$$(u_x)_{tp} = T_P \sin \phi_{tp} \exp[ik_{tp}(x \sin \phi_{tp} - \alpha_2 t)], \quad (4.51)$$

$$(u_y)_{tp} = T_P \cos \phi_{tp} \exp[ik_{tp}(x \sin \phi_{tp} - \alpha_2 t)], \quad (4.52)$$

$$(\tau_{yy})_{tp} = ik_{tp}T_P(\lambda_2 + 2\mu_2 \cos^2 \phi_{tp}) \exp[ik_{tp}(x \sin \phi_{tp} - \alpha_2 t)], \quad (4.53)$$

$$(\tau_{yx})_{tp} = 2ik_{tp}\mu_2 T_P \sin \phi_{tp} \cos \phi_{tp} \exp[ik_{tp}(x \sin \phi_{tp} - \alpha_2 t)]. \quad (4.54)$$

The transmitted S-wave (T_S):

$$d_x = -\cos \phi_{ts}, \quad d_y = \sin \phi_{ts}, \quad p_x = \sin \phi_{ts}, \quad p_y = \cos \phi_{ts}, \quad (4.55)$$

$$(u_x)_{ts} = -T_S \cos \phi_{ts} \exp[ik_{ts}(x \sin \phi_{ts} - \beta_2 t)], \quad (4.56)$$

$$(u_y)_{ts} = T_S \sin \phi_{ts} \exp[ik_{ts}(x \sin \phi_{ts} - \beta_2 t)], \quad (4.57)$$

$$(\tau_{yy})_{ts} = 2ik_{ts}T_S\mu_2 \sin \phi_{ts} \cos \phi_{ts} \exp[ik_{ts}(x \sin \phi_{ts} - \beta_2 t)], \quad (4.58)$$

$$(\tau_{yx})_{ts} = ik_{ts}\mu_2 T_S(\sin^2 \phi_{ts} - \cos^2 \phi_{ts}) \exp[ik_{ts}(x \sin \phi_{ts} - \beta_2 t)]. \quad (4.59)$$

From continuity condition at the interface between the two media, we have 4 equations, 2 for the displacements in the x and y -direction and 2 for the normal stress τ_{yy} and the shear stress τ_{yx} :

$$(u_x)_I + (u_x)_{rp} + (u_x)_{rs} = (u_x)_{tp} + (u_x)_{ts}, \quad (4.60)$$

$$(u_y)_I + (u_y)_{rp} + (u_y)_{rs} = (u_y)_{tp} + (u_y)_{ts}, \quad (4.61)$$

$$(\tau_{yy})_I + (\tau_{yy})_{rp} + (\tau_{yy})_{rs} = (\tau_{yy})_{tp} + (\tau_{yy})_{ts}, \quad (4.62)$$

$$(\tau_{yx})_I + (\tau_{yx})_{rp} + (\tau_{yx})_{rs} = (\tau_{yx})_{tp} + (\tau_{yx})_{ts}. \quad (4.63)$$

These equations must be satisfied for all values of x and t [53] which means that the exponential terms in all the previous equations are equal, so

$$k_I \sin \phi_I = k_{rp} \sin \phi_{rp} = k_{rs} \sin \phi_{rs} = k_{tp} \sin \phi_{tp} = k_{ts} \sin \phi_{ts}, \quad (4.64)$$

and

$$k_I \alpha_1 = k_{rp} \alpha_1 = k_{rs} \beta_1 = k_{tp} \alpha_2 = k_{ts} \beta_2. \quad (4.65)$$

$$\frac{k_I}{k_{rp}} = 1, \quad \frac{k_{rs}}{k_I} = \frac{\alpha_1}{\beta_1} = \kappa, \quad \frac{k_{tp}}{k_I} = \frac{\alpha_1}{\alpha_2}, \quad \frac{k_{ts}}{k_I} = \frac{\alpha_1}{\beta_2}. \quad (4.66)$$

Also, by using the following trigonometric relations

$$2 \sin \phi \cos \phi = \sin(2\phi), \quad (4.67)$$

$$\cos^2 \phi - \sin^2 \phi = \cos(2\phi), \quad (4.68)$$

and using relations of the form [53]

$$\frac{\lambda_1 + 2\mu_1 \cos^2 \phi_I}{\mu_1} = \kappa_1^2 \cos(2\phi_{rs}), \quad (4.69)$$

and

$$\frac{\lambda_2 + 2\mu_2 \cos^2 \phi_{tp}}{\mu_1} = \frac{\mu_2}{\mu} (\kappa_2)^2 \cos(2\phi_{ts}), \quad (4.70)$$

we obtain four equations:

$$I_P \sin \phi_I = -R_P \sin \phi_{rp} - R_S \cos \phi_{rs} + T_P \sin \phi_{tp} - T_S \cos \phi_{ts}, \quad (4.71)$$

$$I_P \cos \phi_I = R_P \cos \phi_{rp} - R_S \sin \phi_{rs} + T_P \sin \phi_{tp} + T_S \sin \phi_{ts}, \quad (4.72)$$

$$I_P \sin 2\phi_I = R_P \sin 2\phi_{rp} + R_S \kappa_1 \cos 2\phi_{rs} + T_P \frac{\mu_2 \alpha_1}{\mu_1 \alpha_2} \sin 2\phi_{tp} - T_S \frac{\mu_2 \alpha_1}{\mu_1 \alpha_2} \cos 2\phi_{ts}, \quad (4.73)$$

$$I_P \kappa_1^2 \cos 2\phi_I = -R_P \kappa_1^2 \cos 2\phi_{rs} + R_S \kappa_1 \sin 2\phi_{rs} + T_P \frac{\mu_2 \alpha_1}{\mu_1 \alpha_2} (\kappa_2)^2 \cos 2\phi_{ts} + T_S \frac{\mu_2 \alpha_1}{\mu_1 \alpha_2} \sin 2\phi_{ts}. \quad (4.74)$$

These equations can be solved numerically to give solutions for the amplitude ratios for certain materials employed in the two half-spaces media.

The matrix form of equations (4.71)-(4.74) is

$$I_P \begin{bmatrix} \sin \phi_I \\ \cos \phi_I \\ \sin 2\phi_I \\ \kappa_1^2 \cos 2\phi_{rs} \end{bmatrix} = \begin{bmatrix} -\sin \phi_{rp} & -\cos \phi_{rs} & \sin \phi_{tp} & -\cos \phi_{ts} \\ \cos \phi_{rp} & -\sin \phi_{rs} & \cos \phi_{tp} & \sin \phi_{ts} \\ \sin 2\phi_{rp} & \kappa_1 \cos 2\phi_{rs} & \frac{\mu_2 \alpha_1}{\mu_1 \alpha_2} \sin 2\phi_{tp} & -\frac{\mu_2 \alpha_1}{\mu_1 \alpha_2} \cos 2\phi_{ts} \\ -\kappa_1^2 \cos 2\phi_{rs} & \kappa_1 \sin 2\phi_{rs} & \frac{\mu_2 \alpha_1}{\mu_1 \alpha_2} (\kappa_2)^2 \cos 2\phi_{ts} & \frac{\mu_2 \alpha_1}{\mu_1 \alpha_2} \sin 2\phi_{ts} \end{bmatrix} \begin{bmatrix} R_P \\ R_S \\ T_P \\ T_S \end{bmatrix}.$$

These will be used for our numerical calculations.

4.2.2 Results and discussion

Results for reflection and transmission of P-waves in two half-spaces, where one half-space is a material with a negative Poisson's ratio (auxetic material) are reported here. We used five different values of Poisson's ratio ($\nu_2 = -0.6, -0.4, -0.1, +0.1$ and $+0.4$) for the

material in the upper half-space while the material of lower half-space was considered to be typical material with a positive Poisson's ratio ($\nu_1 = +0.25$).

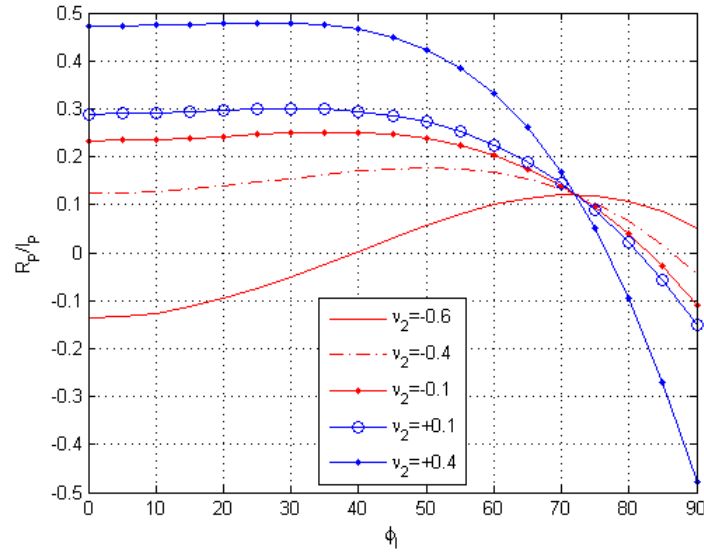


Figure 4.10: The amplitude ratio of reflected longitudinal P-wave, R_P/I_P vs. incident angle, ϕ_I in two half-spaces.

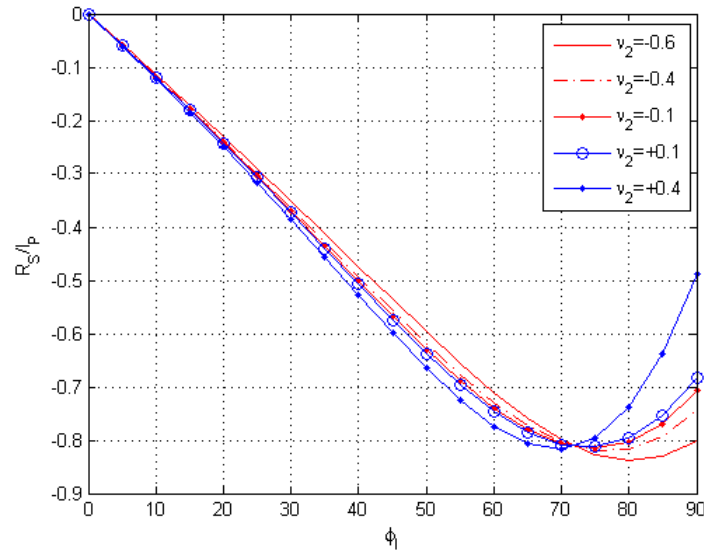


Figure 4.11: The amplitude ratio of reflected transverse P-wave, R_S/I_P vs. incident angle, ϕ_I in two half-spaces.

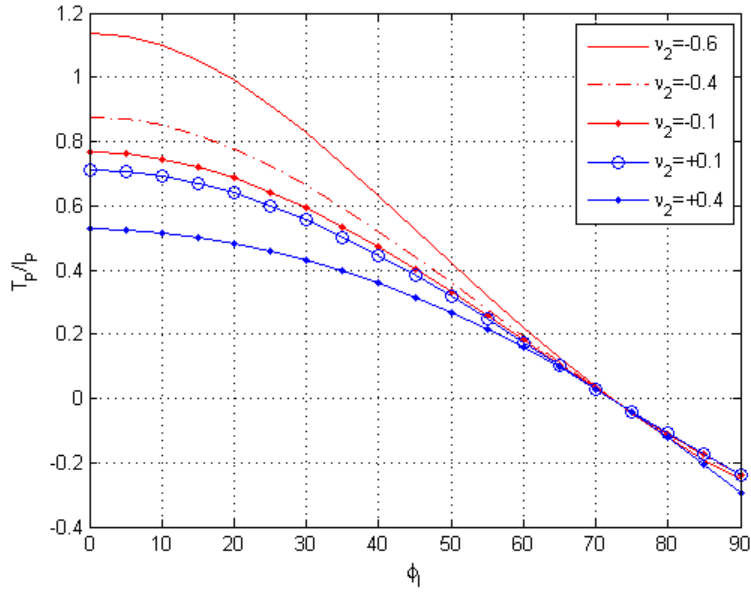


Figure 4.12: The amplitude ratio of transmitted longitudinal P-wave, T_P/I_P vs. incident angle, ϕ_I in two half-spaces.

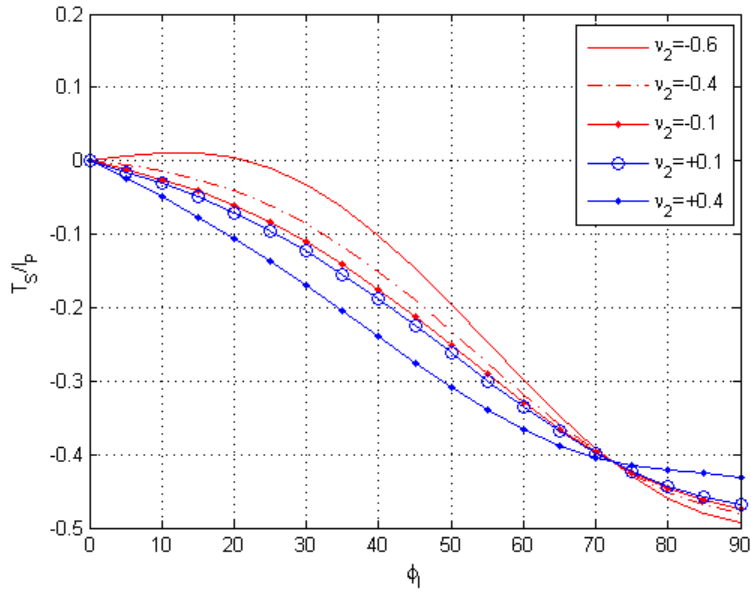


Figure 4.13: The amplitude ratio of transmitted transverse P-wave, T_S/I_P vs. incident angle, ϕ_I in two half-spaces.

The auxetic material has a significant effect on wave propagation as is shown in Figures 4.10 to 4.13. In P-wave propagation, the change in the amplitude ratio value is very clear in reflected and transmitted longitudinal waves, R_P/I_P and T_P/I_P , respectively. The amplitude ratio, at an incident angle of 72° , is constant and does not change for any value of Poisson's ratio for both reflected and transmitted waves. This angle is called a critical angle of incidence. At this angle, there are reflected longitudinal and transverse waves and transmitted transverse waves, while the transmitted longitudinal wave is zero. The interface does not allow T_P -wave to pass at the critical angle.

The amplitude ratio of the longitudinal waves (R_P and T_P), in Figures 4.10 and 4.12, is more affected by the negative Poisson's ratio than that of transverse waves (R_S and T_S), in Figures 4.11 and 4.13.

4.3 Wave propagation in layered half-space

This section contains wave propagation in single layered half-space. First we introduce derivation for the problem, then we investigate the effect of auxetic layer covered the half-space on the reflected SH-wave amplitude.

4.3.1 Mathematical formulation

The problem considered is shown in Figure 4.14. It contains a half-space (L_2) covered by a layer (L_1). Its thickness is H . An incident SH-wave is propagating in the half-space and impinging at the interface to produce reflected and transmitted waves. We will follow Ben-Menahem and Singh's [96] derivation method of multi-layers. They used the n -layer problem ($n > 2$) to obtain the solution, and then reduced the solution to one layered half-space. Here, we derive directly the solution for one layer overlying the half-space starting with single layer overlying an infinite halfspace problem ($n=2$)

The displacement in layered media which is caused by SH-wave takes the z -direction, which is perpendicular to the plane x - y and expressed [53, 54] as

$$u_z = f(y)e^{i(kx - \omega t)}, \quad \text{and} \quad k = \frac{\omega}{c} \quad (4.75)$$

Ben-Menahem et al. [96] have deleted the common factor $\exp[i(\omega t - kx)]$ from the displacement and stress equations from the beginning of the derivation. Also, they used the normalized velocity ($\dot{u} = \frac{\partial u}{\partial t}$) instead of the displacement term u_z in their derivation. We will not use the normalized velocity ($\dot{u} = \frac{\partial u}{\partial t}$) instead of the displacement or omit the common exponential term ($\exp[i(\omega t - kx)]$) from the equations.

This solution in Eq. (4.75) must satisfy the wave equation

$$\nabla^2 u = \frac{1}{\beta^2} \frac{\partial^2 u}{\partial t^2}. \quad (4.76)$$

where

$$\nabla^2 u = \frac{\partial^2 u}{\partial x^2} + \frac{\partial^2 u}{\partial y^2} + \frac{\partial^2 u}{\partial z^2}, \quad (4.77)$$

By deriving the solution, Eq. (4.75) into the two sides of wave equation, Eq. (4.76) we get

$$\nabla^2 u = -k^2 f(y) e^{i(kx - \omega t)} + f''(y) e^{i(kx - \omega t)}, \quad (4.78)$$

and

$$\frac{\partial^2 u}{\partial t^2} = -\omega^2 f(y) e^{i(kx - \omega t)}, \quad (4.79)$$

and putting them together we obtain

$$f''(y) e^{i(kx - \omega t)} - k^2 f(y) e^{i(kx - \omega t)} + \frac{\omega^2}{\beta^2} f(y) e^{i(kx - \omega t)} = 0, \quad (4.80)$$

or,

$$f''(y) e^{i(kx - \omega t)} + \left(\frac{\omega^2}{\beta^2} - k^2 \right) f(y) e^{i(kx - \omega t)} = 0, \quad (4.81)$$

by canceling the common term ($e^{i(kx - \omega t)}$) yields

$$f''(y) + \left(\frac{\omega^2}{\beta^2} - k^2 \right) f(y) = 0, \quad (4.82)$$

or,

$$f''(y) + k^2 \left(\frac{c^2}{\beta^2} - 1 \right) f(y) = 0. \quad (4.83)$$

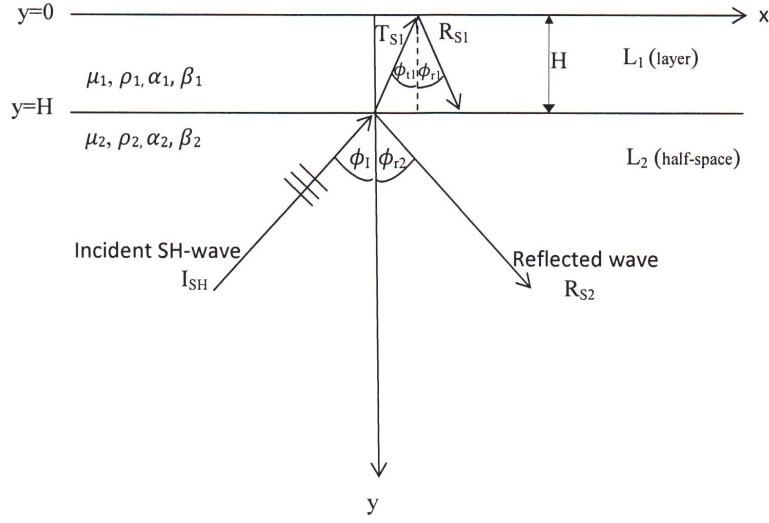


Figure 4.14: Propagation of SH-wave in layered half-spaces

For solving equation (4.83) assume an exponential form

$$f(y) = e^{Sy}, \quad (4.84)$$

and consider

$$\left(\frac{c^2}{\beta^2} - 1\right) = \zeta^2, \quad (4.85)$$

so

$$S^2 e^{Sy} + k^2 \zeta^2 e^{Sy} = 0, \quad \Rightarrow S^2 = -k^2 \zeta^2, \quad \Rightarrow S = \pm \sqrt{-k^2 \zeta^2}, \quad (4.86)$$

then

$$S_1 = ik\zeta, \quad S_2 = -ik\zeta, \quad (4.87)$$

The general solution of the function $f(y)$ for the differential equation (4.83) will be in the form

$$f(y) = C_u e^{S_1 y} + C_d e^{S_2 y}, \quad (4.88)$$

or

$$f(y) = C_u e^{ik\zeta y} + C_d e^{-ik\zeta y}, \quad (4.89)$$

where $\zeta = \sqrt{(\frac{c^2}{\beta^2} - 1)}$. Substituting in the displacement equation (4.75) we obtain

$$u_z = [C_u e^{ik\zeta y} + C_d e^{-ik\zeta y}]e^{i(kx - \omega t)}. \quad (4.90)$$

The last equation (4.90) is as Ben-Menahem and Singh [96] stated in chapter 3 (section 3.7), where $C_u = I_{SH}$ or T_{S1} , is the amplitude of the upgoing wave and $C_d = R_{S2}$ or R_{S1} is the amplitude of the downgoing wave.

There will be two equations for the displacement, one for the layer (L_1) and the other for the half-space (L_2):

$$(u_z)_1 = [T_{S1} e^{ik\zeta_1 y} + R_{S1} e^{-ik\zeta_1 y}]e^{i(kx - \omega t)}, \quad (4.91)$$

$$(u_z)_2 = [I_{SH} e^{ik\zeta_2 y} + R_{S2} e^{-ik\zeta_2 y}]e^{i(kx - \omega t)}. \quad (4.92)$$

Also, there will be two equations for the stress, one for the layer (L_1) and the other for the half-space (L_2):

$$(\tau_{yz})_1 = [ik\mu_1\zeta_1 T_{S1} e^{ik\zeta_1 y} - ik\mu_1\zeta_1 R_{S1} e^{-ik\zeta_1 y}]e^{i(kx - \omega t)}, \quad (4.93)$$

$$(\tau_{yz})_2 = [ik\mu_2\zeta_2 I_{SH} e^{ik\zeta_2 y} - ik\mu_2\zeta_2 R_{S2} e^{-ik\zeta_2 y}]e^{i(kx - \omega t)}. \quad (4.94)$$

There is another form for the function $f(y)$ which may be obtained by using the Euler relation

$$e^{ix} = \cos(x) + i \sin(x), \quad (4.95)$$

This yields

$$f(y) = A \cos(k\zeta y) + iB \sin(k\zeta y), \quad (4.96)$$

where $A = C_u + C_d$ and $B = C_u - C_d$. The displacement and stress are then

$$u_z = [A \cos(k\zeta y) + iB \sin(k\zeta y)]e^{i(kx-\omega t)}, \quad (4.97)$$

$$\tau_{yz} = [-A\mu k\zeta \sin(k\zeta y) + iB\mu k\zeta \cos(k\zeta y)]e^{i(kx-\omega t)}. \quad (4.98)$$

Now, we will investigate the displacement and the stress in the layer (L_1) at the boundaries.

1- At the free surface where $y=0$:

Here, we substitute $y=0$ in Eqs. (4.97) and (4.98) we obtain

$$(u_z)_1 = A_1 e^{i(kx-\omega t)} = (u_z)_0, \quad (4.99)$$

$$(\tau_{yz})_1 = iB_1 \mu_1 k\zeta_1 e^{i(kx-\omega t)} = (\tau_{yz})_0. \quad (4.100)$$

If we apply the condition that the free surface at $y=0$ is traction free that means $(\tau_{yz})_0 = 0$ which lead to $B_1 = 0$.

2- At the interface where $y=H$:

Also, by substituting $H=y$ and $B_1 = 0$ in Eqs. (4.97) and (4.98) we obtain

$$(u_z)_1 = A_1 \cos(k\zeta_1 H)e^{i(kx-\omega t)}, \quad (4.101)$$

$$(\tau_{yz})_1 = -A_1 \mu_1 k\zeta_1 \sin(k\zeta_1 H)e^{i(kx-\omega t)}, \quad (4.102)$$

substituting the constants $A_1 = (u_z)_0 e^{-i(kx-\omega t)}$ into the previous two equations (4.101) and (4.102)

$$(u_z)_1 = (u_z)_0 \cos(k\zeta_1 H), \quad (4.103)$$

$$(\tau_{yz})_1 = -(u_z)_0 \mu_1 k\zeta_1 \sin(k\zeta_1 H). \quad (4.104)$$

Also, we have at the interface

$$(u_z)_1 = (u_z)_2, \text{ for } y = H, \text{ and } (\tau_{yz})_1 = (\tau_{yz})_2, \text{ for } y = H.$$

From equations (4.92) and (4.94), substitute into equations (4.103) and (4.104) we obtain

$$[I_{SH} e^{ik\zeta_2 H} + R_{S2} e^{-ik\zeta_2 H}]e^{i(kx-\omega t)} = (u_z)_0 \cos \Omega_1, \quad (4.105)$$

and

$$[ik\mu_2\zeta_2 I_{SH} e^{ik\zeta_2 H} - ik\mu_2\zeta_2 R_{S2} e^{-ik\zeta_2 H}]e^{i(kx-\omega t)} = -(u_z)_0 \mu_1 k \zeta_1 \sin \Omega_1, \quad (4.106)$$

where $\Omega_1 = k\zeta_1 H$, also substitute $(u_z)_0 = u_0 e^{i(kx-\omega t)}$ we get

$$I_{SH} e^{ik\zeta_2 H} + R_{S2} e^{-ik\zeta_2 H} = u_0 \cos \Omega_1, \quad (4.107)$$

and

$$ik\mu_2\zeta_2 I_{SH} e^{ik\zeta_2 H} - ik\mu_2\zeta_2 R_{S2} e^{-ik\zeta_2 H} = -u_0 \mu_1 k \zeta_1 \sin \Omega_1, \quad (4.108)$$

where $u_0 = T_{S1} + R_{S1}$.

The matrix form of equations (4.107) and (4.108), in the formula of $\mathbf{b}=\mathbf{A}\mathbf{x}$ is

$$\begin{bmatrix} I_{SH} e^{ik\zeta_2 H} \\ ik\mu_2\zeta_2 I_{SH} e^{ik\zeta_2 H} \end{bmatrix} = \begin{bmatrix} \cos \Omega_1 & -e^{-ik\zeta_2 H} \\ -k\mu_1\zeta_1 \sin \Omega_1 & ik\mu_2\zeta_2 e^{-ik\zeta_2 H} \end{bmatrix} \begin{bmatrix} u_0 \\ R_{S2} \end{bmatrix}.$$

Dividing by $I_{SH} e^{-ik\zeta_2 H}$ we obtain

$$\begin{bmatrix} e^{2ik\zeta_2 H} \\ ik\mu_2\zeta_2 e^{2ik\zeta_2 H} \end{bmatrix} = \begin{bmatrix} \cos \Omega_1 e^{ik\zeta_2 H} & -1 \\ -k\mu_1\zeta_1 \sin \Omega_1 e^{ik\zeta_2 H} & ik\mu_2\zeta_2 \end{bmatrix} \begin{bmatrix} u_0/I_{SH} \\ R_{S2}/I_{SH} \end{bmatrix},$$

To get the vector of the amplitude ratios we calculate the inverse of coefficients matrix (A)

$$\begin{bmatrix} \frac{u_0}{I_{SH}} \\ \frac{R_{S2}}{I_{SH}} \end{bmatrix} = \frac{1}{\cos \Omega_1 (ik\mu_2\zeta_2) e^{ik\zeta_2 H} - k\mu_1\zeta_1 \sin \Omega_1 e^{ik\zeta_2 H}} \begin{bmatrix} ik\mu_2\zeta_2 & 1 \\ +k\mu_1\zeta_1 \sin \Omega_1 e^{ik\zeta_2 H} & \cos \Omega_1 e^{ik\zeta_2 H} \end{bmatrix} \begin{bmatrix} e^{2ik\zeta_2 H} \\ ik\mu_2\zeta_2 e^{2ik\zeta_2 H} \end{bmatrix}$$

The amplitude ratio at the free surface is

$$\frac{u_0}{I_{SH}} = \frac{ik\mu_2\zeta_2 e^{2ik\zeta_2 H} + ik\mu_2\zeta_2 e^{2ik\zeta_2 H}}{\cos \Omega_1 (ik\mu_2\zeta_2) e^{ik\zeta_2 H} - k\mu_1\zeta_1 \sin \Omega_1 e^{ik\zeta_2 H}} \quad (4.109)$$

or

$$\frac{u_0}{I_{SH}} = \frac{2ik\mu_2\zeta_2 e^{2ik\zeta_2 H}}{\cos \Omega_1 (ik\mu_2\zeta_2) e^{ik\zeta_2 H} - k\mu_1\zeta_1 \sin \Omega_1 e^{ik\zeta_2 H}} \quad (4.110)$$

Divide by $ik\mu_2\zeta_2 e^{ik\zeta_2 H}$ where $1/i = -i$, we obtain the final equation as mentioned in [96]

$$\frac{u_0}{I_{SH}} = \frac{2e^{ik\zeta_2 H}}{\cos \Omega_1 + i \frac{\mu_1\zeta_1}{\mu_2\zeta_2} \sin \Omega_1} \quad (4.111)$$

Also, The aptitude ratio of reflected SH-wave is given by

$$\frac{R_{S2}}{I_{SH}} = \frac{k\mu_1\zeta_1 \sin \Omega_1 e^{ik\zeta_2 H} e^{2ik\zeta_2 H} + \cos \Omega_1 (ik\mu_2\zeta_2) e^{ik\zeta_2 H} e^{2ik\zeta_2 H}}{\cos \Omega_1 (ik\mu_2\zeta_2) e^{ik\zeta_2 H} + k\mu_1\zeta_1 \sin \Omega_1 e^{ik\zeta_2 H}} \quad (4.112)$$

Similarly, divide by $ik\mu_2\zeta_2 e^{ik\zeta_2 H}$ we obtain

$$\frac{R_{S2}}{I_{SH}} = \frac{\cos \Omega_1 e^{2ik\zeta_2 H} + \frac{k\mu_1\zeta_1}{ik\mu_2\zeta_2} \sin \Omega_1 e^{2ik\zeta_2 H}}{\cos \Omega_1 - \frac{k\mu_1\zeta_1}{ik\mu_2\zeta_2} \sin \Omega_1} \quad (4.113)$$

or

$$\frac{R_{S2}}{I_{SH}} = \frac{\cos \Omega_1 - i \frac{\mu_1\zeta_1}{\mu_2\zeta_2} \sin \Omega_1}{\cos \Omega_1 + i \frac{\mu_1\zeta_1}{\mu_2\zeta_2} \sin \Omega_1} e^{2ik\zeta_2 H} \quad (4.114)$$

Equations (4.111) and (4.114) are the same equations that Ben-Menahem and Singh [96] have obtained in their book.

4.3.2 Results and Discussion

In the layered half-space, we can conclude the following points:

a) When the layer and the half-space materials both have the same density (ρ), Young's modulus (E), wave number, and the incident angle (ϕ) is equal to $\pi/3$, and the Poisson's ratio of the layer changes from -1 to 0.5, the amplitude has a complex value. When the Poisson's ratio of the layer is positive ($0 < \nu < 0.5$), the imaginary part of the amplitude

changes from +1 to 0. But when the Poisson's ratio of the layer is negative ($-1 < \nu < 0$), the imaginary part of the amplitude changes from 0 to -1 then changes from -1 to 0 as shown in Figure 4.15, i.e., the imaginary part of the amplitude has positive value if Poisson's ratio is positive and has negative value if Poisson's ratio is negative. Also, the real part of the amplitude ratio has a positive value from zero to +1 in the positive interval of Poisson's ratio of the layer ($0 < \nu < 0.5$) then it comes down from +1 to -1 in the negative interval of Poisson's ratio of the layer ($-1 < \nu < 0$). Both the real and imaginary part are positive when the Poisson's ratio is positive but they take negative value when $\nu < -0.3$. The imaginary part vanishes and the real part tends to +1 at $\nu = 0$.

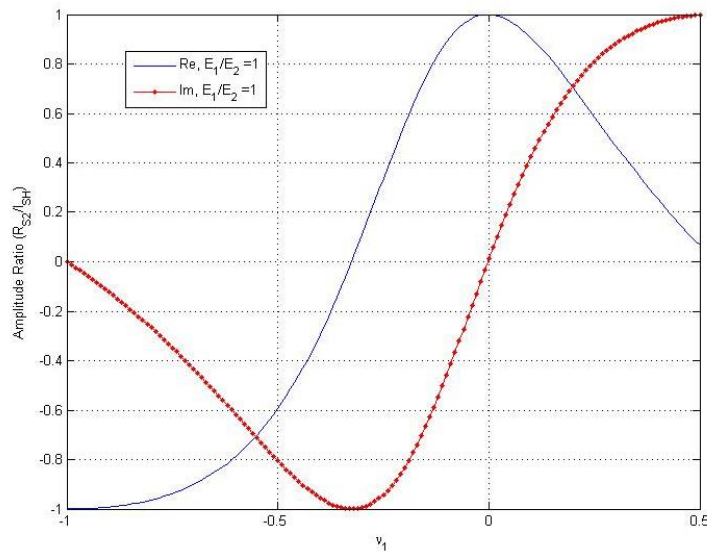


Figure 4.15: The amplitude ratio vs. Poisson's ratio of the layer real (Re) and imaginary (Im) part, $E_1/E_2 = 1$.

Table 4.1: Case when the amplitude ratio is equal to 1 for $\phi = \pi/3$ and $E_1/E_2 < 2$

| E_1/E_2 | 1.2 | 1.1 | 1.0 | 2/3 | 0.5 | 0.1 |
|-----------|-------|-------|---------|--------|------|-------|
| ν | 0.197 | 0.097 | -0.0025 | -0.335 | -0.5 | -0.65 |

b) When E_1/E_2 is small, there is always a complex value for the amplitude ratio until the Young's modulus ratio becomes very large ($E_1/E_2 > 100$). For the large values of E_1/E_2

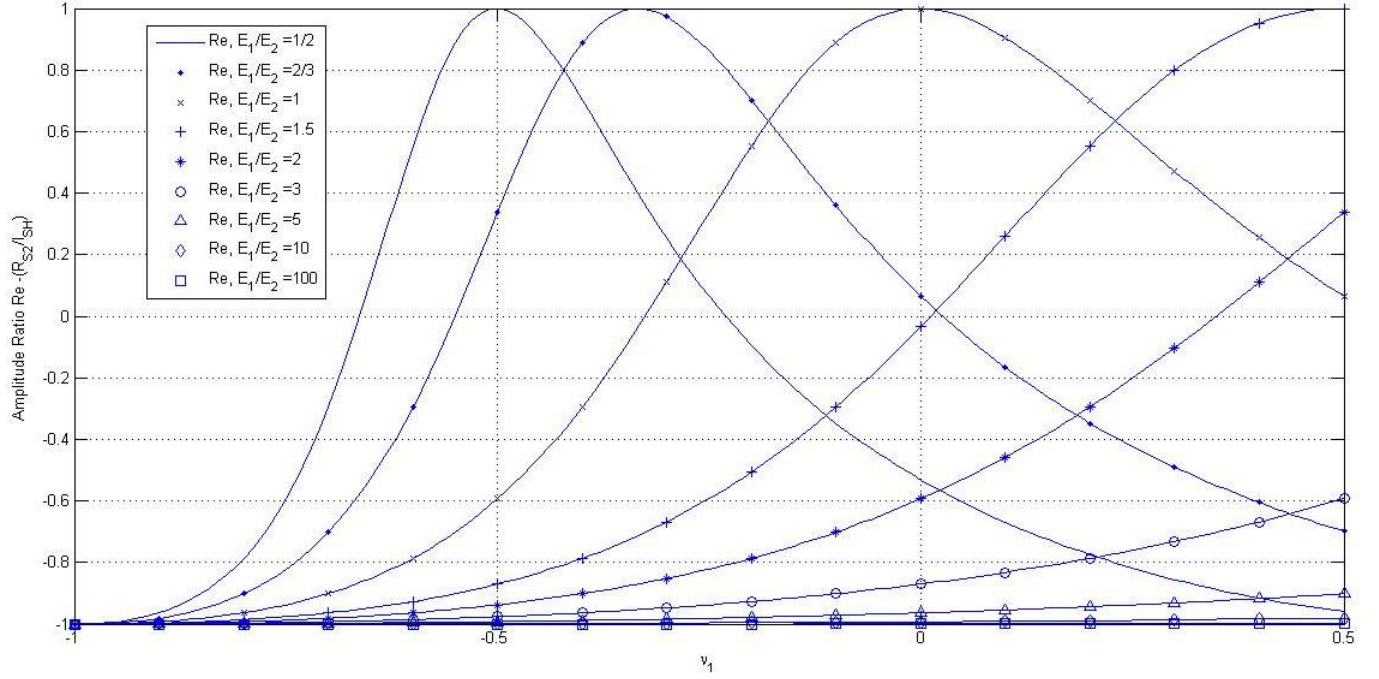


Figure 4.16: The real part of amplitude ratio vs. Poisson's ratio of the layer for various values of E_1/E_2 .

the imaginary part disappears and the real part tends to -1 for all values of Poisson's ratio. When $E_1/E_2 < 2$ there will be at least one real value for the amplitude ratio (the imaginary part is equal zero). For different real values of the amplitude ratio, we found a different Poisson's ratio for the layer for every value of E_1/E_2 as shown Table 4.1. From Table 4.1 when $R_{S2}/I_{SH}=1$, the amplitudes are both equal in the incident wave and reflected wave.

c) For $E_1/E_2 \leq 1$ the amplitude gives maximum real value for reflected wave when $\nu_2 < 0$ and the imaginary part tends to zero at these points, see Figures 4.16 and 4.17.

d) When we change the layer thickness (H) as shown in Figures 4.18 and 4.19 the complex value of the amplitude ratio becomes real (its value is equal to +1) at $\nu_1 = 0$, for all the value of the layer's thickness. Also, it becomes real (its value is equal to -1) again at $\nu_1 = -1$ where the imaginary part at these two values ($\nu_1 = 0$ and -1) tends to zero.

e) When the incident angle is very close to $\pi/2$, the value of the amplitude ratio depends on the Poisson's ratio of the layer. From Figure 4.20, we note that the amplitude ratio has various complex values in the positive range of Poisson's ratio. In the negative range $-0.5 < \nu < 0$ the imaginary part approaches to zero and the real part tends to -1 as the value of ν approaches to -0.5. In the high auxetic range $-1 < \nu < -0.5$ the imaginary part tends to zero, and the real part equal to -1 as long as ν is close to -1 and the complex value becomes pure real value in the range $-1 < \nu < -0.9$.

f) Figures 4.22 and 4.23 show the amplitude ratio (real and imaginary parts) as a function of Poisson's ratio of the layer for five different incidence angles. In general, the amplitude ratio has a complex value. Every case has at least one value of Poisson's ratio at which the imaginary part disappears.

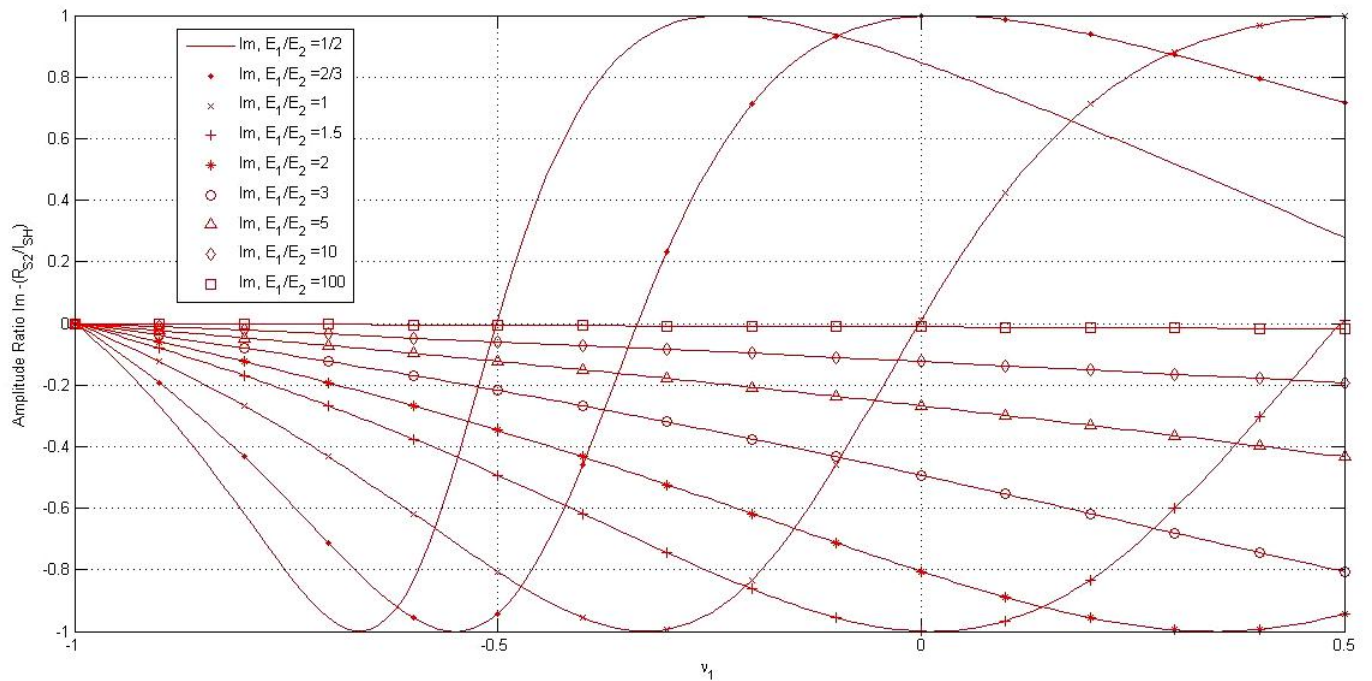


Figure 4.17: The imaginary part of amplitude ratio vs. Poisson's ratio of the layer for various values of E_1/E_2 .

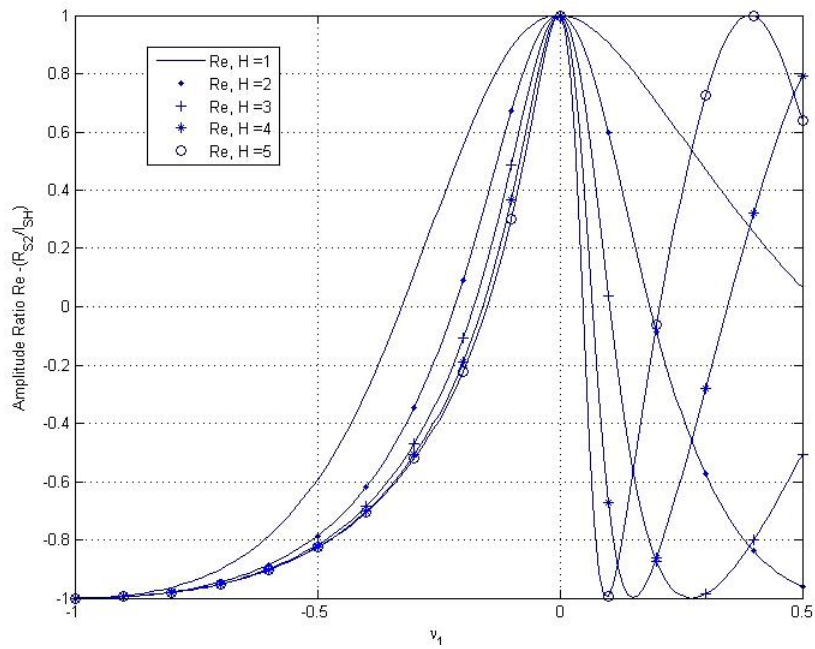


Figure 4.18: The real part of amplitude ratio vs. Poisson's ratio of the layer for various values of layer thickness (H).

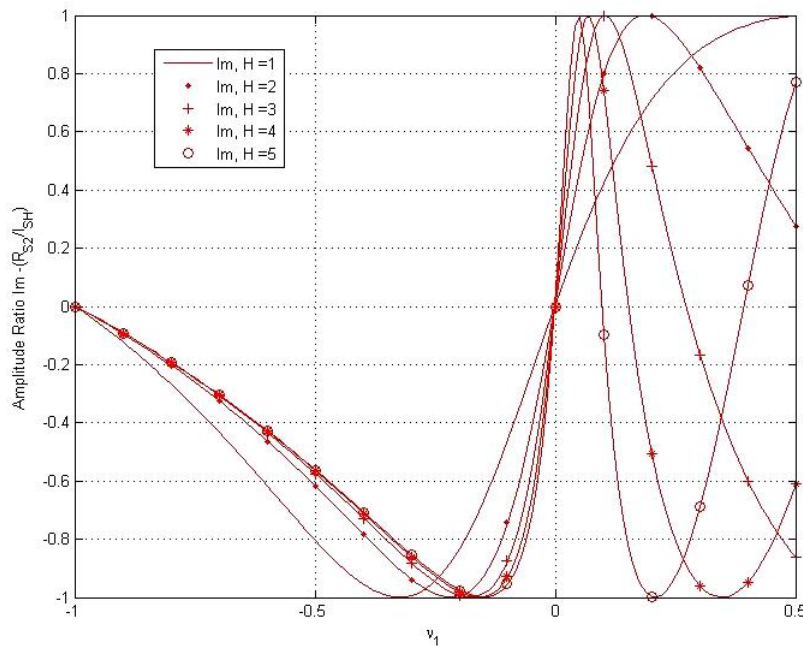


Figure 4.19: The imaginary part of amplitude ratio vs. Poisson's ratio of the layer for various values of layer thickness (H).

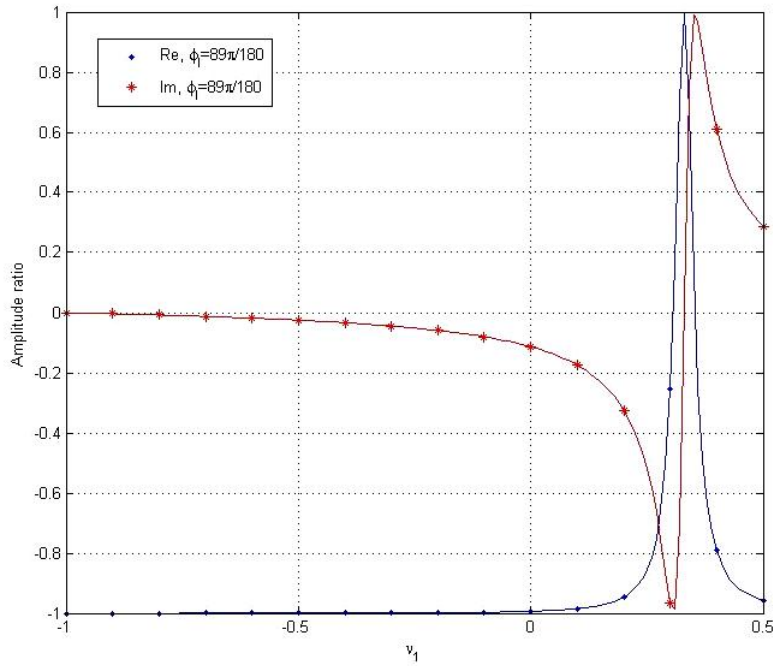


Figure 4.20: The real and imaginary part of amplitude ratio vs. Poisson's ratio for incident angle $\phi_I = 89\pi/180$ (grazing angle).

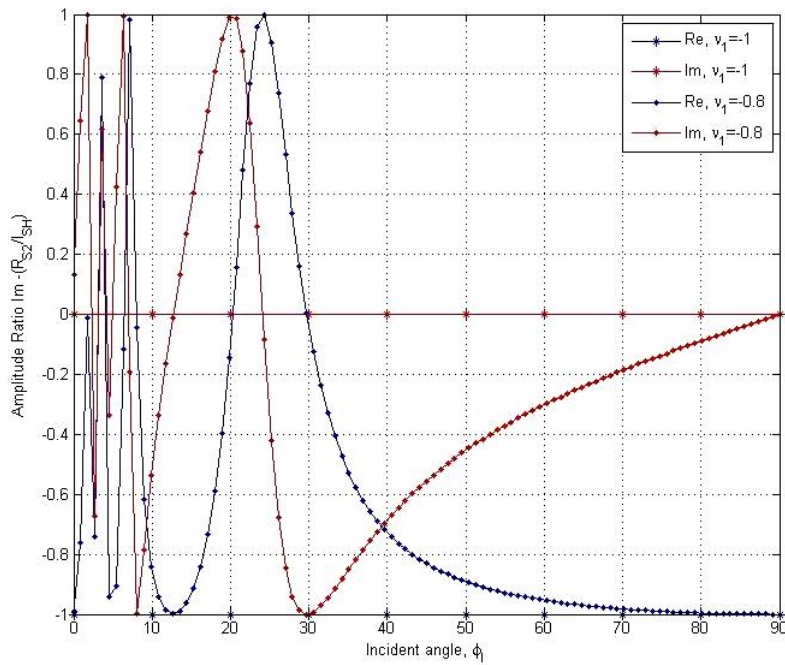


Figure 4.21: The amplitude ratio vs. the incident angle (ϕ_I) for two values of Poisson's ratio ($\nu_1 = -1$ and -0.8).

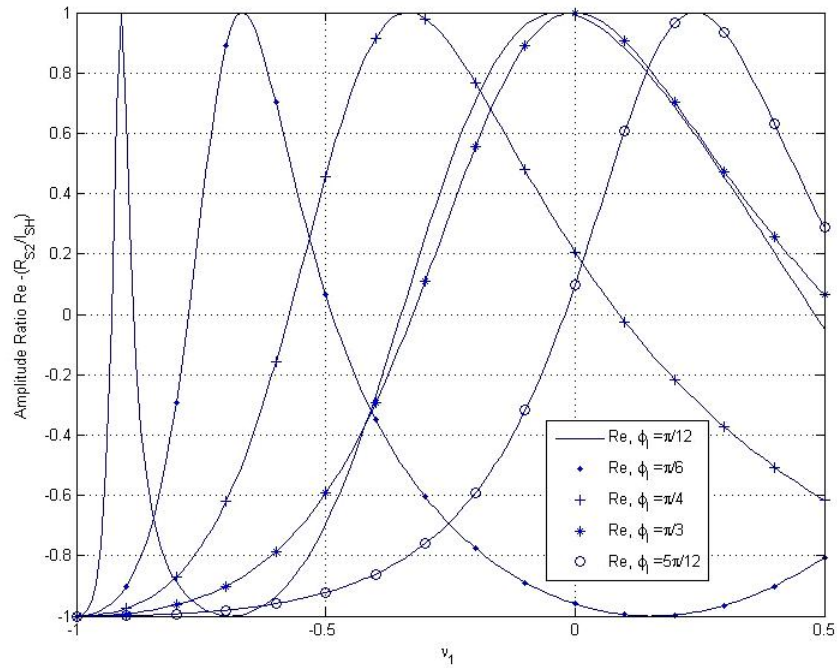


Figure 4.22: The real part of amplitude ratio as a function in Poisson's ratio for various values of incident angle (ϕ_I).

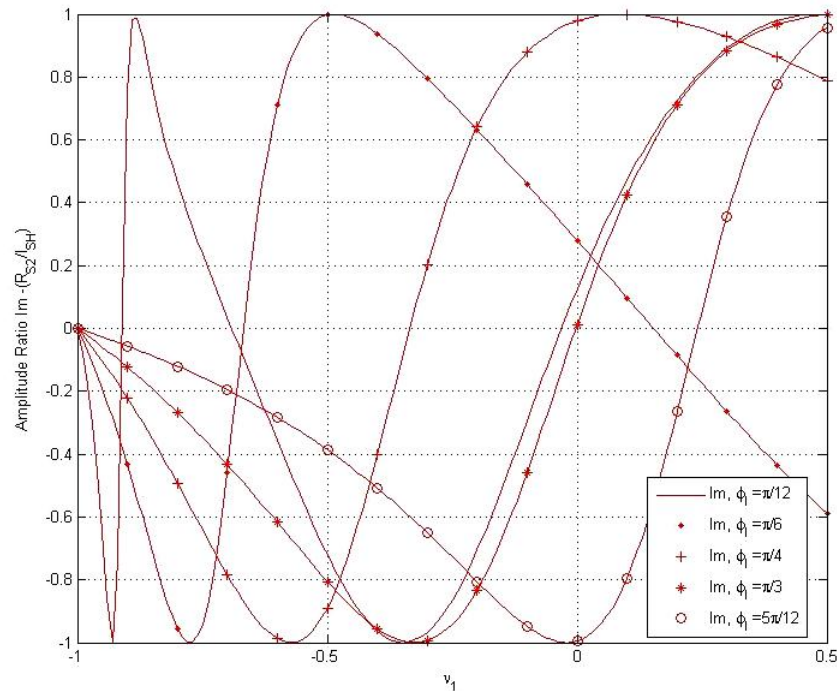


Figure 4.23: The imaginary part of the amplitude ratio as a function in Poisson's ratio for various values of incident angle (ϕ_I).

4.4 Summary

This research has investigated the effect of a negative Poisson's ratio on wave propagation for three problems: a) SH-waves in two half-spaces, b) P-waves in two half-spaces, and c) SH-waves in a layered half-space. The results of this study show that a negative Poisson's ratio has an effect on the amplitude of SH-waves and P-waves in two half-spaces media, and on the amplitude of SH-waves in layered half space problem. When Poisson's ratio is close to -1, there is a significant effect on wave propagation behavior.

In the first problem of SH-waves in two half-spaces, the amplitude may have a complex value or a real value, depending on the combination of the two materials. The amplitude of the transmitted wave changes slightly in the positive interval of Poisson's ratio and the amplitude ratio does not exceed 5%. While the change is bigger in the auxetic interval, $-0.5 < \nu_2 < 0$, in the interval of high auxeticity ($-1 < \nu_2 < -0.5$), we see significant amplification in the amplitude ratio of the transmitted wave to reach 40%.

On the other side of the interface, there is a big difference between the values of amplitude ratio of the reflected wave for the incident angle between 0° and 90° . Also, the amplitude ratio has small change in the positive interval of Poisson's ratio. This change increases in the auxetic range $-1 < \nu_2 < 0$. Some values of the amplitude ratio go from positive to negative between 0.4 and -0.8.

In the second problem of P-waves in two half-spaces, the influence of Poisson's ratio appears more in the reflected and transmitted P-waves. However, there is a slight change in the amplitude ratio of the reflected and transmitted SV-waves for various values of Poisson's ratio.

In the third problem of SH-waves in layered half space, the amplitude of SH-waves has a complex value, as was already mentioned in the discussion. The values of the amplitude for an auxetic material are different than those of a typical material. There are combinations of material properties and incident angles at which we obtained real values for the amplitude ratio.

CHAPTER 5

CONCLUSIONS AND SUGGESTIONS FOR FUTURE WORK

This chapter contains two sections. In the first part, we give conclusions for the three chapters, 2, 3, and 4. We make concluding remarks on the effects of an auxetic material on stress singularities, crack growth direction, and wave propagation. In the last part, we introduce some suggestions for future work.

5.1 Conclusions

This research studied three topics in elasticity: singularities in auxetic bimetals, crack propagation near auxetic particles, and wave propagation in auxetic layered media. The common point between the three topics was the effect of an auxetic material on the solution of these problems. In general, we find through this investigation that there are significant effects on the mechanical behavior due to the negative Poisson's ratio.

5.1.1 Stress singularity

In this chapter, we investigated the change in the singularity in a bi-material with an auxetic material for two problems: the free-edge problem and the interface crack problem. According to the results that we obtained, the auxetic material has a strong effect on the stress singularity order. For the free-edge case, it was found that the singularity order (δ) became increasingly more negative as the the elastic moduli ratio (E_1/E_2) was increased for fixed Poisson's ratio. Once the upper half material became auxetic, the singularity order was affected by the Poisson's ratio. Moreover, it was observed for the cases of $E_1/E_2 < 2$ the singularity order disappears when Poisson's ratio is less than -0.4. However, the singularity order can not be eliminated if the elastic moduli ratio is larger than 3 for all values of Poisson's ratio.

In the interface crack case, the singularity at the tip of the interface crack consists of two parts, the real value and the imaginary oscillatory part. The negative Poisson's ratio only affects the oscillatory part. The auxetic material causes the imaginary part to decrease or vanish for certain values of elastic moduli ratio. We have presented a table for the values of Poisson's ratio at which the imaginary part of the singularity order disappears for various elastic constant ratios.

5.1.2 Crack propagation

This chapter focused on the effect of an auxetic particle on different crack parameters for a crack approaching the particle, such as the crack path direction, the driving force, and the stress intensity near the crack tip. To carry out this investigation, a numerical boundary element method was used. A symmetric Galerkin boundary element method (SGBEM) was employed with a modified quarter-point crack tip element, which produced very accurate results for crack problems.

The effects of the mismatch in Young's modulus (E_p/E_m for an auxetic particle embedded in matrix material) on crack extension was studied. The Young's modulus ratios were 2, 4, 8 and 16. For small ratios of $E_p/E_m = 2, 4$ the crack was attracted to the auxetic particle, while the crack deflects away from the particle when $E_p/E_m > 4$. However, it was noted that the deflection of the crack in the auxetic particle case is less than that for the crack in the non-auxetic particle case.

The stress intensity factors were also studied for $E_p/E_m = 2$. The results showed the deep effect of auxeticity on the stress intensity at the crack tip. In the case of a non-auxetic particle, K_I decreased when the crack approached the particle. But, it increased when the crack approached an auxetic particle. Not only was the stress intensity in mode-I (K_I) affected, but also mode-II (K_{II}). However, the stress intensity in mode-II increased dramatically when the crack approached a non-auxetic particle and decreased when the crack approached an auxetic particle. The shielding of the stress intensity as the crack approached a particle, and the amplification of the stress intensity as the crack passed the particle were

investigated for the case of $E_p/E_m = 8$. The amount of shielding and amplification were almost equal for a typical and an auxetic particle.

Crack deflection or attraction from or to the particle was also studied. It was found that the soft particle, which has elastic moduli ratio ($E_p/E_m < 1$), attracts the crack whether the particle is auxetic or non-auxetic. But a hard particle, $E_p/E_m > 1$, causes the crack to deflect away from the particle except when the particle is auxetic and $1 \leq E_p/E_m \leq 4$. Finally, in the case of double particles, $E_p/E_m > 4$ the crack deflected away from the first particle, and when it approached the upper particle it deflected again towards the inner particle. After that the crack was attracted by the second particle, which meant there was attraction zone around the auxetic particle and if the crack entered this zone it will be attracted by the particle.

5.1.3 Wave propagation

Three elastic wave problems were studied: SH-wave propagation in two half-spaces, P-wave propagation in also two half-spaces and SH-wave propagation in layered half-space. Again, the effect of an auxetic material was the focus of these studies.

In the first problem (SH-wave propagation in two half-spaces), a negative Poisson's ratio suppressed the reflection of SH incident waves and the incident wave totally transmits through the interface. Also, it reduced the transmitted wave amplitude nearly to one half of the incident wave amplitude. In general, the value of the amplitude ratio had a slight change when $0 < \nu < 0.5$, and this change increased in the low interval of auxetic material, $-0.5 < \nu < 0$. It was noted that there is a large change when $-1 < \nu < -0.5$. The change here increased the transmitted amplitude and decreased the reflected amplitude as the auxeticity increased. This effect was more clear for small incidence angles where this change tended to zero as long as the incidence angle tended to 90° .

In the second problem (P-wave propagation in two half-spaces), there was a clear effect on the reflected wave amplitude by negative Poissons ratio for incident angles less than 60° and more than 80° . At small angles the reflected amplitude ratio increased dramatically

from around zero to 0.5. However, the auxeticity affected the longitudinal P-waves, whether transmitted or reflected, much more than the transverse P-waves. The amplitude ratio of the reflected longitudinal P-wave decreased as Poisson's ratio decreased from 0.5 to -0.5. On the other hand, the amplitude ratio of the transmitted longitudinal P-wave increased as Poisson's ratio decreased from -0.5 to -1.

In the third problem (SH-wave propagation in single layered half-space), the amplitude of a reflected SH-wave in a layered half-space generally was complex. When Poisson's ratio of the layer was equal to zero ($\nu = 0$) the reflected amplitude value became real valued (amplitude ratio = 1). For Young's modulus ratio, $E_1/E_2 = 1$, and the Poisson's ratio of the layer $\nu = -0.335$, the amplitude ratio was real valued (-1) which meant that the incident wave totally was reflected by the layer with a phase shift of 180° . For small ratios of Young's modulus, $E_1/E_2 < 2$ there was always a negative Poisson's ratio value at which the amplitude converts from complex to real valued. For all thickness values of the layer, the complex values of the amplitude ratio become real when the layer Poisson's ratio $\nu = 0$. Also, the behavior of curves of the real and imaginary parts of the amplitude showed different behavior for a typical material ($0 < \nu < 0.5$) and an auxetic material ($-1 < \nu < 0$). For example, the real part became smooth in one direction from 1 to -1 (the amplitude ratio) for auxetic material while they take more than directions for typical material.

The research accomplished in this thesis presents and confirms the significant effects of an auxetic material on the mechanical behavior of several parameters in the elastic problems. Hereby, the field is wide open now for scientific researchers and engineers to consider more investigations related to the auxetic materials in solid mechanics.

5.2 Suggestions for Future Work

In general, many studies have been done in the past for typical materials ($0 < \nu < 0.5$) might be repeated using an auxetic material in which the Poisson's ratio changes from -1 to zero ($-1 < \nu < 0$). However, there are limited studies on auxetic behavior. As further studies related to our recent research, we suggest to carry out similar investigations for the

interaction between a crack and auxetic inclusion or group of auxetic inclusions embedded in anisotropic elastic material instead of isotropic material. The second suggestion is carrying out these studies in three-dimensions.

Further investigation is also recommended for the use of auxetic particles for toughening of surfaces. This investigation should focus on how the auxetic particles might be used to control the crack growth direction, or to suppress crack extension.

Finally, we also suggest to study other parameters, such as the T-stress, which is the non singular term in the Williams crack tip stress field expansion, in the light of auxetic material.

REFERENCES CITED

- [1] R. S. Lakes, T. Lee, A. Bersie, and Y. C. Wang. Extreme damping in composite materials with negative-stiffness inclusions. *Nature*, **410**:565–567, 2001.
- [2] J. R. Barber. *Elasticity*. Kluwer Academic Publishers., Waterloo, Ontario, Canada., 2002.
- [3] R. Lakes. Advances in negative Poisson’s ratio materials. *Advanced Materials*, **5**:293–296, 1993.
- [4] K. Bertoldi, P. M. Reis, S. Willshaw, and T. Mullin. Negative Poisson’s ratio behavior induced by an elastic instability. *Advanced Materials*, **22**:261–266, 2010.
- [5] G. N. Greaves, A. L. Greer, R. S. Lakes, and T. Rouxel. Poisson’s ratio and modern materials. *Nature Materials*, **10**:823–837, 2011.
- [6] G. W. Milton. Composite materials with Poisson’s ratios close to -1. *Journal of the Mechanics and Physics of Solids*, **40**(5):1104–1137, 1992.
- [7] R. S. Lakes. Foam structures with a negative Poisson’s ratio. *Science*, **235**:1038–1040, 1987.
- [8] A. Yeganeh-Haeri, D. J. Weidner, and J. B. Parise. Elasticity of α -cristobalite: a silicon dioxide with a negative Poisson’s ratio. *Science*, **257**:650–652, 1992.
- [9] G. E. Stavroulakis. Auxetic behavior: appearance and engineering applications. *Phys. Stat. Sol. (b)*, **242**:710–720, 2005.
- [10] A. Alderson and K. E. Evans. Deformation mechanisms leading to auxetic behavior in the α -cristobalite and α -quartz structures of both silica and germania. *Journal of Physics: Condensed Matter*, **21**:025401–025412, 2009.
- [11] J. N. Grima and K. E. Evans. Auxetic behavior from rotating squares. *Journal of Materials Science Letters*, **19**:1563–1565, 2000.
- [12] J. N. Grima, R. Jackson, A. Alderson, and K. E. Evans. Do zeolites have a negative Poisson’s ratios? *Adv. Mater.*, **12**:1912–1918, 2000.
- [13] A. Alderson and K. E. Evans. Molecular origin of auxetic behavior in tetrahedral framework silicates. *Physical Review Letters*, **89**:225503–225507, 2002.

- [14] J. N. Grima, R. Gatt, A. Alderson, and K. E. Evans. On the origin of auxetic behavior in the silicate α -cristobalite. *Journal of Material Chemistry*, **15**:4003–4005, 2005.
- [15] J. N. Grima and K. E. Evans. Auxetic behavior from rotating triangles. *Journal of Materials Science*, **41**:3193–3196, 2006.
- [16] J. N. Grima, R. Gatt, A. Alderson, and K. E. Evans. alternative explanation for the negative poisson’s ratios in α -cristobalite. *Materials Science and Engineering A*, **423**:219–224, 2006.
- [17] N. Gaspar, C. W. Smith, and K. E. Evans. Auxetic behavior and anisotropic heterogeneity. *Acta Materialia*, **57**:875–880, 2009.
- [18] M. Franke and R. Magerle. Locally auxetic behavior of elastometric polypropylene on the 100 nm length scale. *ACS Nano*, **5**:4886–4891, 2011.
- [19] J. B. Choi and R. S. Lakes. Fracture toughness of re-entrant foam materials with a negative Poisson’s ratio: experiment and analysis. *International Journal of Fracture*, **80**:73–83, 1996.
- [20] K. L. Alderson, A. Fitzgerald, and K. E. Evans. The strain dependent indentation resilience of auxetic microporous polyethylene. *Journal of Materials Science*, **35**:4039–4047, 2000.
- [21] N. R. Keskar and J. R. Chelikowsky. Structural properties of nine silica polymorphs. *Physical Review B*, **46**:1–13, 1992.
- [22] C. W. Smith, J. N. Grima, and K. E. Evans. A novel mechanism for generating auxetic behavior in reticulated foams: missing rib foam model. *Acta Mater.*, **48**:4349–4356, 2000.
- [23] W. Yang, Z.-M. Li, W. Shi, B.-H. Xie, and M.-B. Yang. Review on auxetic materials. *Journal of Materials Science*, **39**:3269–3279, 2004.
- [24] H. Kimizuka, H. Kaburaki, and Y. Kogure. Mechanism for negative Poisson ratios over the α - β transition of cristobalite, SiO₂: A molecular dynamics study. *Physical review letters*, **84**:5548–5551, 2000.
- [25] A. Alderson, K. L. Alderson, K. E. Evans, J. N. Grima, M. R. Williams, and P. J. Davies. Modeling the deformation mechanisms, structure-property relationships and applications of auxetic nanomaterials. *Phys. Stat. Sol. (b)*, **242**:499–508, 2005.

- [26] J. N. Grima, E. Chetcuti, E. Manicaro, D. Attard, M. Camilleri, R. Gatt, and K. E. Evans. On the auxetic properties of generic rotating rigid triangles. *Proceeding of The Royal Society A*, **468**:810–830, 2012.
- [27] D. B. Bogy. Edge-bonded dissimilar orthogonal elastic wedges under normal and shear loading. *Journal of Applied Mechanics*, **35**:460–466, 1968.
- [28] D. B. Bogy. On the problem of edge-bonded elastic quarter-planes loaded at the boundary. *International Journal of Solids and Structures*, **6**:1287–1313, 1970.
- [29] J. Dundurs. Discussion of Bogy. *Journal of Applied Mechanics*, **36**:650–651, 1968.
- [30] V. L. Hein and F. Erdogan. Stress singularities in a two-material wedge. *International Journal of Fracture Mechanics*, **7**:317–330, 1971.
- [31] V. K. Tewary. Elastic Green’s function for a bi-material composite solid containing a free surface normal to the interface. *Journal of Materials Research*, **6**:2592–2608, 1991.
- [32] P. A. Martin. On the green’s function for a bimaterial elastic half-plane. *International Journal of Solids and Structures*, **40**:2101–2119, 2003.
- [33] J. R. Berger, P. A. Martin, and J. P. Lien. Reduction of free-edge stress intensities in anisotropic bi-materials. *International Journal of Fracture*, **91**:165–177, 1998.
- [34] B. Hopkinson. Brittleness and ductility. *Cambridge University Press, London*, :64–76, 1910.
- [35] C. E. Inglis. Stresses in plate due to the presence of cracks and sharp corners. *Transactions of the Institute of Naval Architects*, **55**:219–241, 1913.
- [36] A. A. Griffith. The phenomena of rupture and flow in solids. *Philosophical Transactions of the Royal Society of London. Series A*, **221** :163–198, 1921.
- [37] H. M. Westergaard. Bearing pressures and cracks. *Journal of Applied Mechanics*, **6** : A49–A53, 1939.
- [38] M. L. Williams. On the stress distribution at the base of a stationary crack. *Journal of Applied Mechanics*, **24** :109–114, 1957.
- [39] G. R. Irwin. Analysis of stresses and strains near the end of a crack traversing a plate. *Journal of Applied Mechanics*, **24** :361–364, 1957.
- [40] F. Erdogan and G. C. Sih. On the crack extension in plates under plane loading and transverse shear. *Journal of Fluids Engineering*, **85** (4):519–525, 1963.

- [41] G. C. Sih. Strain-energy-density factor applied to mixed mode crack problems. *International Journal of Fracture*, **10**(3):305–321, 1974.
- [42] B. Cotterell and J. R. Rice. Slightly curved or kinked cracks. *International Journal of Fracture*, **16**(2):155–169, 1979.
- [43] C. Hwu and T. C. T. Ting. Two-dimensional problems of the anisotropic elastic solid with an elliptic inclusion. *The Quarterly Journal of Mechanics and Applied Mathematics*, **42** (4):553–572, 1989.
- [44] A. N. Stroh. Dislocations and cracks in anisotropic elasticity. *Philosophical Magazine*, **3**(30):625–646, 1958.
- [45] C. Hwu and W. J. Yen. On the anisotropic elastic inclusions in plane elastostatics. *Journal of Applied Mechanics*, **60** (3):626–632, 1993.
- [46] W. J. Yen, C. Hwu, and Y. K. Liang. Dislocation inside, outside, or on the interface of an anisotropic elliptical inclusion. *Journal of Applied Mechanics*, **62** (2):306–311, 1995.
- [47] C. Hwu, Y. K. Liang, and W. J. Yen. Interactions between inclusions and various types of cracks. *International journal of fracture*, **73**(4):301–323, 1995.
- [48] D.-H. Chen. The effect of an elliptical inclusion on a crack. *International Journal of Fracture*, **85** (4):351–364, 1997.
- [49] M. B. Bush. The interaction between a crack and a particle cluster. *International Journal of Fracture*, **88**(3):215–232, 1997.
- [50] R. Kitey, A.-V. Phan, H. V. Tippur, and T. Kaplan. Modeling of crack growth through particulate clusters in brittle matrix by symmetric-Galerkin boundary element method. *International Journal of Fracture*, **141**(1-2):11–25, 2006.
- [51] L. J. Gray, A.-V. Phan, G. H. Paulino, and T. Kaplan. Improved quarter-point crack tip element. *Engineering Fracture Mechanics*, **70**(2):269–283, 2003.
- [52] R. C Williams, A.-V. Phan, H. V. Tipplur, T. Kaplan, and L. J. Gray. SGBEM analysis of crack-particle(s) interactions due to elastic constants mismatch. *Engineering Fracture Mechanics*, **74**:314–331, 2007.
- [53] J. Achenbach. *Wave Propagation in Elastic Solids*. Elsevier, 1984.
- [54] W. M. Ewing, W. S. Jardetzky, and F. Press. *Elastic Wave in Layered Media*. McGraw-Hill Company New York, 1957.

- [55] T. J. Bromwich. On the influence of gravity on elastic waves, and, in particular on the vibrations of an elastic globe. *Proceedings of the London Mathematical Society*, **1**(1): 98–120, 1898.
- [56] A. E. H. Love. *A treatise on the mathematical theory of elasticity*. Cambridge University Press, 2013.
- [57] M. A Biot. The influence of initial stress on elastic waves. *Journal of Applied Physics*, **11**(8):522–530, 1940.
- [58] W. T. Thomson. Transmission of elastic waves through a stratified solid medium. *Journal of Applied Physics*, **21**(2):89–93, 1950.
- [59] A. J. Philippacopoulos. Waves in a partially saturated layered half-space: analytic formulation. *Bulletin of the Seismological Society of America*, **77**(5):1838–1853, 1987.
- [60] M. Muskat and M. W. Meres. Reflection and transmission coefficients for plane waves in elastic media. *Geophysics*, **5**(2):115–148, 1940.
- [61] Y.-S. Wang, G.-L. Yu, and B.-Z. Gai. Propagation of sh waves in a layered half-space with a frictional contact interface. *Bulletin of the Seismological Society of America*, **88**(5):1300–1310, 1998.
- [62] J. Liu, Y. Wang, and B. Wang. Propagation of shear horizontal surface waves in a layered piezoelectric half-space with an imperfect interface. *Ultrasonics, Ferroelectrics and Frequency Control, IEEE Transactions on*, **57**(8):1875–1879, 2010.
- [63] M. Destrade and G. Saccomandi. Finite amplitude elastic waves propagating in compressible solids. *Physical Review E*, **72**(1):016620, 2005.
- [64] M. M. Carroll. Some results on finite amplitude elastic waves. *Acta Mechanica*, **3**(2): 167–181, 1967.
- [65] A. W. Lipsett and A. I. Beltzer. Reexamination of dynamic problems of elasticity for negative poisson’s ratio. *Journal of Acoustical Society of America*, **84**:2179–2186, 1988.
- [66] T.-C. Lim, P. Cheang, and F. Scarpa. Wave motion in auxetic solids. *physica Status Solidi (b)*, **251**(2):388–396, 2014.
- [67] R. V. Goldstein, V. A. Gorodtsov, and D. S. Lisovenko. Rayleigh and Love surface waves in isotropic media with negative Poisson’s ratio. *Acta Mechanica*, **49**:422–434, 2014.

- [68] T. C. Lim. Vibration of thick auxetic plates. *Mechanics Research Communications*, **61**: 60–66, 2014.
- [69] C .A. Brebbia and J. Dominguez. *Boundary elements: An introductory course*. Computational Mechanics Publications, McGraw - Hill Book Company, Southampton - Boston, 1992.
- [70] A. Sutradhar, G. H. Paulino, and L. J. Gray. *Symmetric Galerkin Boundary Element Method*. Springer-Verlag Berlin Heidelberg, 2008.
- [71] M. H. Aliabadi. *The Boundary Element Method, Volume 2, Applications in Solids and Structures*. Wiley, 2002.
- [72] T. A. Cruse. *Boundary Element Analysis in Computational Fracture Mechanics*, volume **1**. Springer, 1988.
- [73] T. A. Cruse. Mathematical foundations of the boundary-integral equation method in solid mechanics. Technical report, DTIC Document, 1977.
- [74] M. Bonnet, G. Maier, and C. Polizzotto. Symmetric Galerkin boundary element methods. *Applied Mechanics Reviews*, **51**(11):669–704, 1998.
- [75] C. V. Camp and G. S. Gipson. Overhauser elements in boundary element analysis. *Mathematical and Computer Modelling*, **15**(3):59–69, 1991.
- [76] L. J. Gray, J. M. Glaeser, and T. Kaplan. Direct evaluation of hypersingular Galerkin surface integrals. *SIAM Journal on Scientific Computing*, **25**(5):1534–1556, 2004.
- [77] L. J. Gray et al. Evaluation of singular and hypersingular Galerkin integrals: direct limits and symbolic computation. *Singular Integrals in Boundary Element Methods, Comp. Mech. Publ., Southampton*, pages 45–84, 1998.
- [78] L. J. Gray. Presentation about SGBEM by Dr. Leonard J. Gray, Colorado School of Mines, Spring 2010.
- [79] M. M. Adam, J. R. Berger, and P. A. Martin. Singularities in auxetic elastic bimetals. *Mechanics Research Communications*, 47:102–105, 2013.
- [80] S. Ding and M. Kumosa. Singular stress behavior at an adhesive interface corner. *Engineering Fracture Mechanics*, **47**:503–519, 1994.
- [81] M. L. Williams. The stress around a fault or crack in dissimilar media. *Bulletin of the Seismological Society of America*, **49**:199–204, 1952.

- [82] J. W. Hutchinson and Z. Suo. Mixed mode cracking in layered materials. *Advances in Applied Mechanics*, **29**:63–192, 1992.
- [83] C. Atkinson. Stress singularities and fracture mechanics. *Applied Mechanics Reviews*, **32**:123–135, 1979.
- [84] L. Gu and T. Belytschko. A numerical study of stress singularities in a two-material wedge. *International Journal of Solids and Structures*, **31**:865–889, 1994.
- [85] O. Tamate. The effect of a circular inclusion on the stresses around a line crack in a sheet under tension. *International Journal of Fracture Mechanics*, **4**:257–266, 1968.
- [86] C. Atkinson. The interaction between a crack and an inclusion. *International Journal of Engineering Science*, **10**:127–136, 1972.
- [87] F. Erdogan, G. Gupta, and M. Ratwani. Interaction between a circular inclusion and an arbitrarily oriented crack. *Journal of Applied Mechanics*, **41**:1007–1013, 1974.
- [88] C. Hwu, Y. K. Liang, and W. J. Yen. Interactions between inclusions and various types of cracks. *International Journal of Fracture*, **73**:301–323, 1995.
- [89] M. G. Knight, L. C. Wrobel, J. L. Henshall, and L. A. De Lacerda. A study of the interaction between a propagating crack and an uncoated/coated elastic inclusion using the be technique. *International Journal of Fracture*, **114**:47–61, 2002.
- [90] S. Sirtori, G. Maier, G. Novati, and S. Miccoli. A Galerkin symmetric boundary element method in elasticity: formulation and implementation. *International Journal for Numerical Methods in Engineering*, **35**:255–282, 1992.
- [91] R. D. Henshell and K. G. Shaw. Crack tip finite elements are unnecessary. *International Journal for Numerical Methods in Engineering*, **9**:495–507, 1975.
- [92] R. S. Barsoum. On the use of isoparametric finite elements in fracture mechanics. *International Journal for Numerical Methods in Engineering*, **10**:25–37, 1974.
- [93] L. J. Gray and G. H. Paulino. Crack tip interpolation, revisited. *SIAM Journal on Applied Mathematics*, **58**:428–455, 1998.
- [94] F. Erdogan and G. C. Sih. On the crack extension in plates under plane loading and transverse shear. *Journal of Basic Engineering*, **86**:519–527, 1963.
- [95] H. Tada, P. C. Paris, and G. R. Irwin. *The Analysis of Cracks Handbook*. New York: ASME Press, 2000.

- [96] A. Ben-Menahem and S. J. Singh. *Seismic Waves and Sources*. Courier Dover Publications, 2012.

APPENDIX - PROGRAMS, CODES USED AND METHODS

Here, MatLab code and some examples of input and output files are included. The package is shown in the next Figure, Figure A.1.

| Name | Date modified | Type | Size |
|----------------|----------------------|---------------|----------|
| A | 1/29/2011 10:58 AM | File | 53 KB |
| A | 1/29/2011 10:56 AM | Text Document | 59 KB |
| AOriginal | 1/19/2011 1:53 PM | File | 45 KB |
| AOriginal | 1/4/2011 9:27 AM | Text Document | 43 KB |
| CrackGrowth | 1/25/2011 1:28 PM | M File | 7 KB |
| crackgrowth6 | 1/29/2011 12:29 PM | M File | 5 KB |
| fortran | 1/25/2011 1:24 PM | M File | 1 KB |
| KPlot | 1/29/2011 10:56 AM | DAT File | 2 KB |
| KPlotOriginal | 12/18/2010 9:28 PM | DAT File | 0 KB |
| resetall | 1/25/2011 12:58 PM | M File | 1 KB |
| script | 1/25/2011 1:22 PM | M File | 1 KB |
| SGBEM | 12/16/2010 10:33 ... | Application | 1,587 KB |
| XY | 1/29/2011 10:56 AM | DAT File | 1 KB |
| XYOriginal | 1/25/2011 12:44 PM | DAT File | 1 KB |
| XYPlot | 1/29/2011 10:56 AM | DAT File | 2 KB |
| XYPlotOriginal | 1/25/2011 12:45 PM | DAT File | 1 KB |

Figure A.1: Code Package For Crack Growth Direction calculations

A.1 MATLAB program

MATLAB program (CrackGrowth) is used to plot the crack path, by reading K_I and K_{II} from the output FORTRAN file, then calculate the crack path angle, calculate the (x, y) coordinates, modified FORTRAN input file, record (x, y) and redo this multi-times.

```
classdef CrackGrowth
    % CrackGrowth Class

    methods(Static)
        function Calculate(FortranOutputFile, XY_DataFile, DeltaA,
            FortranInputFile, XY_PlotFile, K_PlotFile)
            disp 'Growing crack...'
```

```

XY = load(XY_DataFile);
OldTip = XY(4,1:2);
OldThetaC = XY(5,1);
if (all(OldTip == [0 0.01]))
    HP = [0 0.0095];
else
    HP = OldTip - (0.50 * DeltaA) .* [cos(OldThetaC) sin(
        OldThetaC)];
end

% find the beginning of the last line
fid = fopen(FortranOutputFile, 'r');
if (fseek(fid, -2, 'eof') == 0)
    while (fscanf(fid, '%c', 1) ~= char(10)) && (fseek(fid
        , -2, 'cof') == 0)
    end
    last_line = fgetl(fid);
end
fclose(fid);

K = sscanf(last_line, '%f');
K(1) = [];

ThetaC = OldThetaC + 2*atan((-2*K(2)/K(1))/(1+sqrt(1+8*(K
    (2)/K(1))^2)));

QP = OldTip + (0.75 * DeltaA) .* [cos(ThetaC) sin(ThetaC)];
Tip = OldTip + DeltaA .* [cos(ThetaC) sin(ThetaC)];

XY = [[HP 0 0 3 3]; [OldTip 0 0 3 3]; [QP 0 0 3 3]; [Tip 0
    0 3 3]; [ThetaC 0 0 0 0]];
fid = fopen(XY_DataFile, 'wt');
fprintf(fid, '% 1.10E % 1.10E % 1.10E % 1.10E %d %d\n', XY)
;
fclose(fid);

XYOutputMatrix = [load(XY_PlotFile); Tip];
fid = fopen(XY_PlotFile, 'wt');
fprintf(fid, '% 1.10E % 1.10E\n', XYOutputMatrix);
fclose(fid);

KOutputMatrix = [load(K_PlotFile); K];
fid = fopen(K_PlotFile, 'wt');
fprintf(fid, '% 1.10E % 1.10E\n', KOutputMatrix);
fclose(fid);

% Modify Fortran input file

```

```

InputStringSet = cell.empty();
fid = fopen(FortranInputFile, 'r');
while true
    dataline = fgetl(fid);
    if (dataline == -1)
        break;
    end
    InputStringSet{end+1} = dataline;
end
fclose(fid);

OutputStringSet = cell.empty();

OutputStringSet{end+1} = InputStringSet{1};
OutputStringSet{end+1} = InputStringSet{2};

OutputStringSet{end+1} = InputStringSet{3};
OriginalNumberOfNodes = sscanf(InputStringSet{3}, '%f');
TempString = sprintf('%6d', OriginalNumberOfNodes+2);
OutputStringSet{end}(1:length(TempString)) = TempString;

for i = 1:OriginalNumberOfNodes
    TempString = InputStringSet{3+i};
    TempString(TempString == 'D') = 'E';
    NodeArray(i,:) = sscanf(TempString, '%f')';
end

i = 4 + i;
OutputStringSet{i+0+2} = InputStringSet{i+0};
OutputStringSet{i+1+2} = InputStringSet{i+1};
OutputStringSet{i+2+2} = InputStringSet{i+2};
OutputStringSet{i+3+2} = InputStringSet{i+3};
OutputStringSet{i+4+2} = InputStringSet{i+4};
OutputStringSet{i+5+2} = InputStringSet{i+5};
OutputStringSet{i+6+2} = InputStringSet{i+6};
OutputStringSet{i+7+2} = InputStringSet{i+7};
OutputStringSet{i+8+2} = InputStringSet{i+8};

Corner = sscanf(InputStringSet{i+3}, '%f');
Corner = Corner(1);
TempString = sprintf('%6d', Corner+2);
OutputStringSet{i+3+2}(1:length(TempString)) = TempString;

Base = sscanf(InputStringSet{i+5}, '%f');
TempString = sprintf('%6d%5d%5d', Base(1), Base(2), Base(3)
+2);
OutputStringSet{i+5+2} = TempString;

```

```

Base = Base(3);

ElementsInZone1 = sscanf(InputStringSet{i+6}, '%f ');
TempString = sprintf('%5d', ElementsInZone1+1);
OutputStringSet{i+6+2}(1:length(TempString)) = TempString;

XY(5,:) = [];
NodeArray = [NodeArray(1:(Base-3),:); [XY [0;0;0;0]];
             NodeArray(Base:end,:)];
NodeArray(:,7) = (1:length(NodeArray))';

i = 9 + i;

for j = 1:OriginalNumberOfNodes+2
    OutputStringSet{3+j} = sprintf('% 1.10E % 1.10E % 1.10E
    % 1.10E %d %d %d', NodeArray(j,:));
    OutputStringSet{3+j}(OutputStringSet{3+j} == 'E') = 'D
    ';
end

for j = 1:ElementsInZone1
    TempString = InputStringSet{i+j-1};
    IndexArray(j,:) = sscanf(TempString, '%f ')';
end

OldBaseIndex = find(IndexArray(:,1) == Base);
IndexArray(OldBaseIndex,:) = IndexArray(OldBaseIndex,:) -
    1;
OldCornerIndex = find(IndexArray(:,1) == Corner+1);
IndexArray(OldCornerIndex,:) = IndexArray(OldCornerIndex,:) -
    1;
OldEndIndex = find(IndexArray(:,1) == OriginalNumberOfNodes
    ) - 1;
IndexArray = [IndexArray(1:OldEndIndex,:); IndexArray(
    OldEndIndex,:)+2; IndexArray(OldEndIndex+1,:)+2;
    IndexArray(OldEndIndex+1:(end-1),:)]';

for j = 1:ElementsInZone1+1
    OutputStringSet{i+j+1} = sprintf('%d\t%d\t%d',
    IndexArray(j,:));
end

i = i + ElementsInZone1;
OutputStringSet{i+0+3} = InputStringSet{i+0};
OutputStringSet{i+1+3} = InputStringSet{i+1};
OutputStringSet{i+2+3} = InputStringSet{i+2};
OutputStringSet{i+3+3} = InputStringSet{i+3};

```

```

OutputStringSet{i+4+3} = InputStringSet{i+4};
OutputStringSet{i+5+3} = InputStringSet{i+5};
OutputStringSet{i+6+3} = InputStringSet{i+6};

OldTip = sscanf(InputStringSet{i+2}, '%f');
OldTip = OldTip(1);
TempString = sprintf('%4d', OldTip+2);
OutputStringSet{i+2+3}(1:length(TempString)) = TempString;

ElementsInZone2 = sscanf(InputStringSet{i+3}, '%f');

i = i + 7;

for j = 1:ElementsInZone2
    TempString = InputStringSet{i+j-1};
    IndexArray2(j,:) = sscanf(TempString, '%f')';
end
IndexArray2 = [IndexArray2(2:end,:); IndexArray2(end,:)+2];

for j = 1:ElementsInZone2
    OutputStringSet{i+j+2} = sprintf('%d\t%d\t%d',
        IndexArray2(j,:));
end

i = i + ElementsInZone2;

OutputStringSet{i+0+3} = InputStringSet{i+0};
OutputStringSet{i+1+3} = InputStringSet{i+1};

fid = fopen(FortranInputFile, 'wt');
for j = 1:length(OutputStringSet)
    fprintf(fid, '%s', OutputStringSet{j});
    if (j ~= length(OutputStringSet))
        fprintf(fid, '\n');
    end
end
fclose(fid);
end
end
end

```